A miniaturized optical gas sensor for natural gas analysis

Ayerden, Pelin

DOI
10.4233/uuid:2d31aed1-bec6-4d58-a790-e0be6e90b5db

Publication date
2016

Document Version
Final published version

Citation (APA)
Ayerden, P. (2016). *A miniaturized optical gas sensor for natural gas analysis*. [Dissertation (TU Delft), Delft University of Technology]. https://doi.org/10.4233/uuid:2d31aed1-bec6-4d58-a790-e0be6e90b5db

A MINIATURIZED OPTICAL GAS SENSOR FOR NATURAL GAS ANALYSIS

A MINIATURIZED OPTICAL GAS SENSOR FOR NATURAL GAS ANALYSIS

Proefschrift

ter verkrijging van de graad van doctor
aan de Technische Universiteit Delft,
op gezag van de Rector Magnificus prof. ir. K. C. A. M. Luyben,
voorzitter van het College voor Promoties,
in het openbaar te verdedigen op dinsdag 5 juli 2016 om 10:00 uur

door

Nadire Pelin AYERDEN

Master of Science in Engineering, Koç University, Turkey
geboren te Karabük, Turkije.

This dissertation has been approved by the

promoter: Prof. dr. ir. A. J. P. Theuwissen
copromoter: Dr. ir. R. F. Wolffenbuttel

Composition of the doctoral committee:

Rector Magnificus	chairman
Prof. dr. ir. A. J. P. Theuwissen	Delft University of Technology, promoter
Dr. ir. R. F. Wolffenbuttel	Delft University of Technology, copromoter

Independent members:

Prof. dr. B. Dam	Delft University of Technology
Prof. dr. P. French	Delft University of Technology
Prof. dr. P. Enoksson	Chalmers University of Technology
Prof. dr. G. Minas	University of Minho
Dr. F. J. M. Harren	Radboud University

This work has been supported by the Dutch technology foundation STW under grant DEL.11476.

Keywords: Gas sensor, natural gas, hydrocarbons, Fabry-Perot, Fizeau interferometer, LVOF, mid-IR, optical absorption spectroscopy

Printed by: IPSKAMP Printing

ISBN 978-94-6186-681-3

Cover design by Adrián Fulcar

An electronic version of this dissertation is available at
http://repository.tudelft.nl/.

CONTENTS

1

INTRODUCTION

1

1.1. NATURAL GAS IN THE NETHERLANDS

NATURAL gas has been commonly used as a source of energy for more than a century in both households and industry [1]. However, several complications have appeared in the last decade. The depletion of domestic resources has forced many countries to import natural gas or liquefied natural gas (LNG). Moreover, due to the negative environmental effects of fossil fuels, more sustainable energy sources such as biogas are provided to the users. Furthermore, with rapidly growing cities; hence, denser and more complex gas grids, it has become harder for the energy provider to ensure the quality and the constant composition of the supplied gas. These issues call for the development of instruments to monitor the distributed gas quality.

Natural gas is also a major source of energy in the Netherlands. Due to the availability of the local resources in Groningen and the North Sea as shown in Fig. 1.1, the Netherlands has so far been self-sufficient in natural gas production.

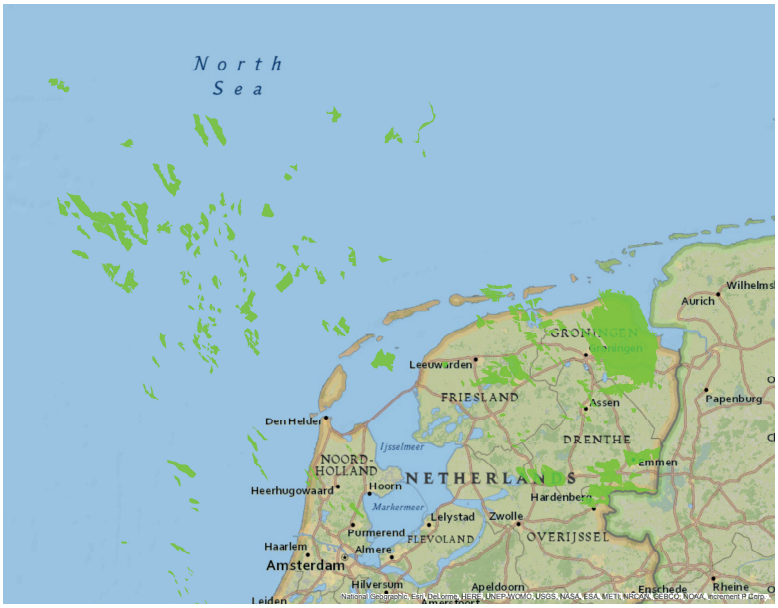

Figure 1.1: The natural gas fields in the Netherlands, indicated in green [2].

However, the natural gas production in the Netherlands is expected to decrease by almost 80% in the coming 20 years as shown in Fig. 1.2 [2]. The depletion of natural gas resources forces a transition from the locally produced gas (G-gas) with a well-known composition toward the 'new' gas with a more flexible composition. The 'new' gas is a mixture of high-calorific-value gas (H-gas) imported from other countries such as Russia and Norway, and LNG imported from Middle East and Africa. Also, biogas is introduced

in the Dutch gas grid as a sustainable source of energy [3]. In all these scenarios, the composition of the gas that is supplied to the user changes from the very stable G-gas composition to mixtures with other sources of energy [4].

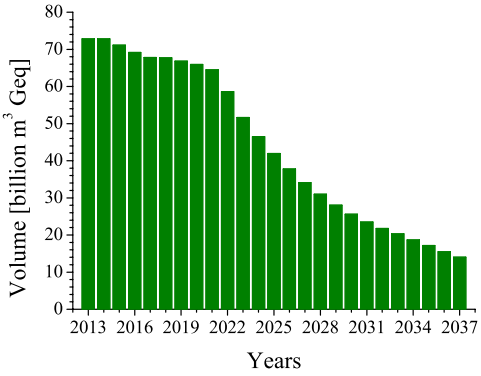

Figure 1.2: The expected natural gas production in the Netherlands. (Geq stands for Groningen gas equivalent with a heating value of 35.17 MJ/m^3.)

The main components of natural gas are hydrocarbons. Typical compositions of G-gas, H-gas and LNG are listed in Table 1.1 [5]. Methane (CH_4) has the highest concentration in all types of natural gas, while ethane (C_2H_6) is the second most abundant component in the natural gas mixture. Although propane (C_3H_8) and butane (C_4H_{10}) constitute a very small part of natural gas, these cannot be neglected due to their relatively high heating values [6]. Therefore, gas producers are usually interested in the sum of their concentration instead of the individual values. In addition to hydrocarbons, natural gas includes carbon dioxide (CO_2) and nitrogen (N_2).

Table 1.1: Typical compositions of G-gas, H-gas, and LNG.

	CH_4 (mol %)	C_2H_6 (mol %)	C_3H_8 (mol %)	C_4H_{10} (mol %)	CO_2 (mol %)	N_2 (mol %)
G-gas	82.3	3.07	0.47	0.09	1.1	12.7
H-gas	89	5.3	1.3	0.3	1.2	2.3
LNG	90	6.25	1	2.1	1	1.1

The transportation of natural gas from the well to the gas grid is schematically illustrated in Fig. 1.3. Imported H-gas and LNG as well as biogas are added to the Dutch gas at the processing plants. Then, the new mixture is distributed to the industrial customers and the local distribution companies through high pressure transmission pipelines. Lastly, the households receive natural gas through the low pressure distribution grid.

The change in the gas concentration has substantial effect on the performance of the burners and other household appliances [7, 8]. For safe and clean combustion and

1

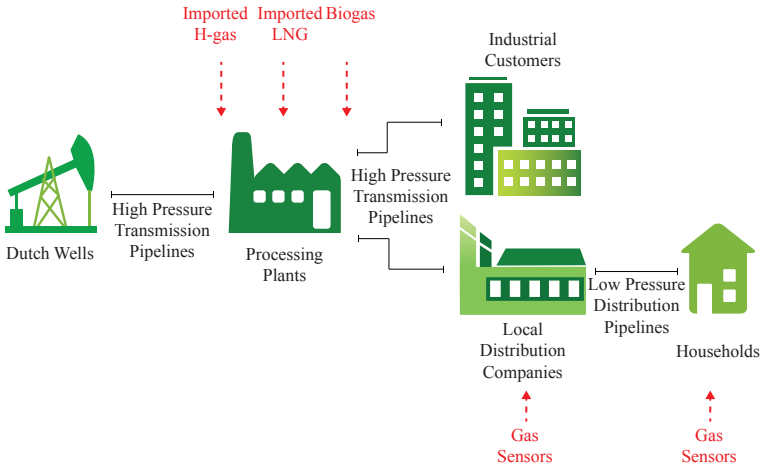

Figure 1.3: Transportation of natural gas.

proper billing, the composition of natural gas must be monitored at both distribution points and households. This calls for a robust and low-cost gas sensor that does not require sample preparation or a lab technician to analyze the results.

1.2. GAS SENSING METHODS

Gas sensors are categorized based on the type of response that they exhibit in the presence of the sample. Ideally, gas sensors must be selective to every specimen as shown in Fig. 1.4. However, in many applications, the components of the sample mixture are previously known and have sufficiently dissimilar characteristics to measure.

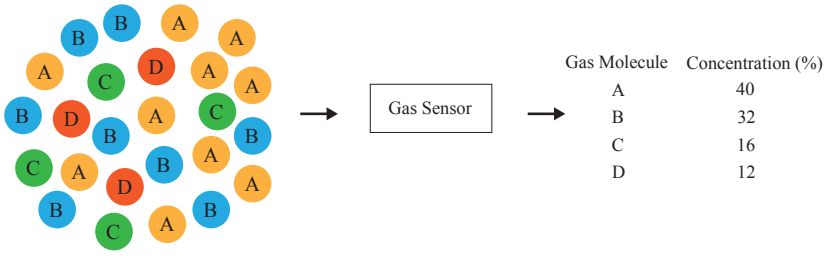

Figure 1.4: An ideal gas sensor distinguishing components of a gas mixture.

Metal-oxide gas sensors are widely used for the detection of carbon monoxide (CO) and nitrogen dioxide (NO_2) in air quality measurements [9]. The operation principle relies on the fact that the adsorption and desorption of gases changes the electrical conductivity of semiconductors [10]. Despite their high sensitivity and low cost, the depen-

dency of the optimum operation temperature of the sensor on the sample, which can vary from 25 °C to 500 °C for an SnO_2-based sensor, is a limiting factor [11]. Moreover, these sensors suffer from long recovery periods, which makes them undesirable for applications where fast detection is required.

The poor sensitivity of metal-oxide gas sensors at room temperature pushed carbon nanotube (CNT)-based sensors forward in spite of the complexity of their fabrication. Thanks to their large surface-area-to-volume ratio, CNT-based gas sensors exhibit enhanced adsorptivity; hence, high sensitivity [12]. Moreover, by applying different coatings, the selectivity and the sensitivity of a CNT-based gas sensor can be improved, while tailoring the porosity of the structure [13, 14]. These sensors are mainly used in the detection of alcohol, ammonia (NH_3), carbon dioxide (CO_2) and nitrogen oxide (NO_x).

Pellistors are widely used low-cost calorimetric sensors for gas detection. There are two main types of pellistor, catalytic sensors to measure flammable gases and thermal conductivity based sensors to measure gases that have a significant difference in thermal conductivity to that of air [15]. A catalytic sensor is composed of two beads on wire coils, one for gas detection and one for compensation as shown in Fig. 1.5(a), [16]. The detector bead contains a catalyst to stimulate the combustion of the gas to be measured, while the compensator bead remains nonreactive. The beads are heated by flowing electrical current through the wires and the resulting change in temperature due to the gas is measured resistively, typically in a Wheatstone bridge configuration. However, these sensors suffer from poisoning from certain types of compounds such as sulfur (H_2S), which inhibits the response of the sensor to combustible gases [17]. Therefore, despite their simple operating principle and low cost, catalytic pellistors put a prior condition on the sample set and are not capable of distinguishing highly similar molecules such as hydrocarbons. In a similar fashion, thermal conductivity based sensors correlate the loss in heated resistance wires due to the gas mixture flowing through the sensor to the thermal conductivity of the individual components of the gas sample [18]. However, these devices can measure only binary mixtures, where the sample is composed of merely two gases [19]. Therefore, in spite of its simplicity, reliability and low cost, thermal conductivity detectors are not suitable for measuring natural gas because of the complex composition of the sample and the limited selectivity of the method.

Electrochemical gas sensors are usually employed in the detection of toxic gases. They consist of a sensing and a counter electrode with a thin layer of electrolyte in-between as shown in Fig. 1.5(b), [20]. The gas diffusing through the sensor goes into a reaction with the sensing electrode. By measuring the change in the current or the voltage between the sensing and the counter electrode, the change in the concentration of the sample gas is quantified. Since the electrode materials are selected specifically to catalyze the gas of interest, these sensors must be tailored for different types of samples,

rendering them highly selective. Compared to nondestructive methods, electrochemical sensors have a shorter lifespan [21].

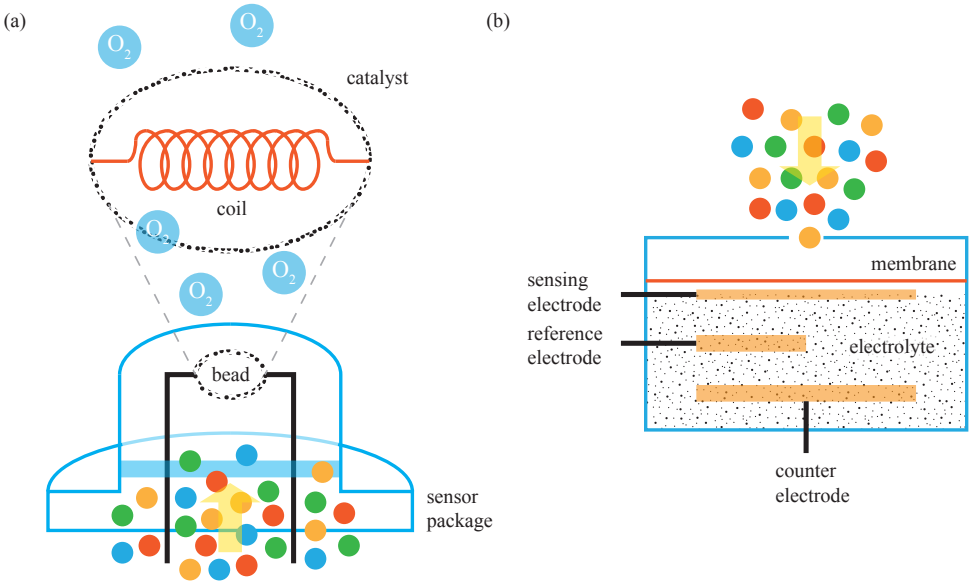

Figure 1.5: Schematic illustration of (a) a catalytic and (b) an electrochemical sensor.

The gold standard of natural gas composition measurement is gas chromatography [22]. In this method, the sample mixture is introduced into the injection port, carried through the column by an inert gas, where it is separated into its components based on the affinity of each component for the stationary phase and finally reaches the detector, conventionally a mass spectrometer, where the individual components are quantitatively analyzed as shown in Fig. 1.6. Despite their high sensitivity and selectivity, gas chromatographs are bulky and expensive lab equipment. Much effort has been put on miniaturizing the injector [23], the column [24] and the detector element [25, 26] using microelectromechanical systems (MEMS) technology. Both scientific [27, 28] and commercial [29] MEMS based gas chromatography systems are available; however, the method has practical limitations at wafer-level miniaturization for fully portable applications due to the requirement of sample handling and carrier gas supply.

Optical absorption spectroscopy is a commonly used method for material identification due to its nondestructive and self-referencing properties. For gas sensing it offers a promising compromise between high-resolution and high-cost methods such as gas chromatography, and nonselective and low-cost methods involving calorimetric sensing [30]. In optical absorption spectroscopy, light is passed through a sample and the ratio of absorbed to incident radiation is recorded as shown in Fig. 1.7, [31]. The sample

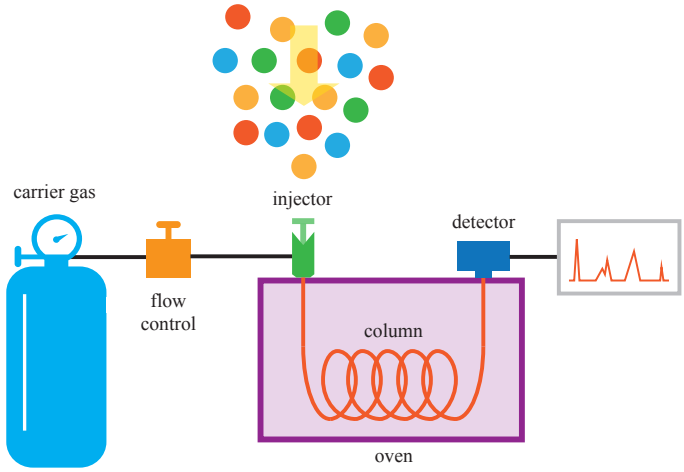

Figure 1.6: Schematic illustration of a gas chromatograph.

is identified by comparing the acquired spectrum with a database. The actual spectral position of the series of absorption peaks is unique for each chemical substance, while the amount of optical absorption at each of these peaks is correlated to the concentration of the chemical species. Therefore, the composition of a gas mixture, where each individual gas is characterized by a specific absorption spectrum, can be measured using a spectrometer and multivariate analysis techniques [32]. This method is particularly suitable for the measurement of combustible gases that contain hydrocarbons in the mid-IR, because of their unique absorption spectra in this wavelength range.

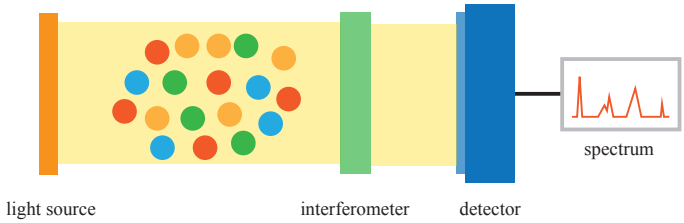

Figure 1.7: Schematic illustration of an optical absorption spectrometer.

Distinguishing the components of natural gas using a single sensing method is challenging. Therefore, a microsystem that combines multiple sensors on a chip is more effective and gives more accurate results. This work focuses on the measurement of hydrocarbons using optical absorption spectroscopy in the mid-IR wavelength range.

1

1.3. OUTLINE OF THIS THESIS

This thesis describes the functional integration of a gas cell and a linear variable optical filter (LVOF) for the analysis of hydrocarbons in natural gas. The objective is to build a robust and low-cost microspectrometer that does not require sample preparation or a carrier gas supply as in gas chromatography. To achieve robustness, optical absorption spectroscopy is selected as the measurement technique due to its self-referencing property, which renders periodic calibration unnecessary. Moreover, the wavelength-selective component that is usually composed of moving parts to achieve wideband operation, is designed such that the spectral response in a wide wavelength range is measured without any moving parts to aid the robustness of the whole system. The key to attain low unit cost is high-volume production using microfabrication techniques. A CMOS-compatible MEMS device that is batch-fabricated at the wafer-level has major advantages on reproducible high-volume production with low unit cost. The sample cell occupies a significant volume in a spectrometer due to the fact that the absorption is proportional to the path that the light beam travels through the sample and a significant absorption is required to measure the small spectral variation therein. Integrating such a large component with a microspectrometer at the wafer-level, while maintaining the dimensions of a typical external gas cell is a big challenge. Using the resonator cavity of an LVOF as a gas cell by exploiting the multiple reflections from highly reflective mirrors allows for a mm-level effective absorption path, while the dimensions of the cavity remain at the µm-level. Therefore, the gas-filled LVOF is a significant improvement in the miniaturization of spectrometers.

The thesis is composed of seven chapters. The motivation and the aim of the project in addition to the gas composition measurement methods are described in chapter 1. In chapter 2, the conventional techniques for optical absorption spectroscopy are explained. Moreover, the optical filter based approach is selected as the most suitable technique and the miniaturization of individual components of such a system is investigated. Furthermore, the evolution of the wafer-level miniaturization is presented step-by-step and finally the gas-filled LVOF is opted for due to its high suitability for the application.

Chapter 3 describes the theoretical background of the optical design of an LVOF and the optical constraints (or optimization parameters, depending on the perspective) on the filter performance. Conventionally, LVOFs are approximated as fixed Fabry-Perot (FP) filters and designed using thin-film design tools. However, an FP filter assumes two parallel mirrors, while the operation principle of an LVOF relies on the small angle between them. Therefore, a new design approach, where the LVOF is treated as a Fizeau wedge with the tilt angle taken into consideration is introduced. The performance of the LVOF is simulated using both approaches and it is shown that the Fizeau approach

is more appropriate at demanding operating conditions. In addition, the effect of the operating order, mirror reflectivity, incidence angle, filter-detector separation and the cone angle of light source on the spectral performance of the filter are investigated.

The optical design of the gas-filled LVOF using the Fizeau approach is explained in chapter 4. Firstly, available mid-IR spectral databases for hydrocarbons are investigated. After selecting the 3.2 µm to 3.4 µm wavelength range, the operating order of the filter and the reflectivity of the mirrors that are required for the application are studied. A device with 3-pair Si-SiO_2 Bragg mirrors operating at the 15^{th} order is designed. The effect of the gas is incorporated into the design using the absorption coefficient of methane that is modified using the resolution of the device. Also, the incidence angle is included as an optimization parameter for improving the elongation of the optical path length.

The details of the CMOS-compatible fabrication and the initial characterization of the tapered structures are provided in chapter 5. After explaining the fabrication flows of the flat and the tapered Bragg mirrors, the masks that are used in the process are described. These two mirrors are integrated by wafer bonding, resulting in the gas-filled LVOF with a tapered cavity that also serves as a gas cell. Moreover, the mirror profiles are measured using a stylus profilometer prior to wafer bonding.

Chapter 6 explains the characterization of the gas-filled LVOF. Firstly, the Bragg mirrors and a fixed FP filter are characterized using a Fourier transform infrared (FTIR) spectrometer. Based on these measurements, the limitations of the measurement setup as well as the susceptibility of the device to the collimation of the light source are demonstrated. A custom-built setup with a HeNe laser at 3392 nm is used to measure the spectral response of the filters. The same setup is also employed in the gas measurements, where methane is flown through the filter cavity. For wideband characterization, the HeNe laser is replaced with an optical parametric oscillator (OPO) laser. Measurements with methane, ethane and propane prove the selectivity, while dilutions with nitrogen demonstrate the sensitivity to the concentration of the sample constituents.

Finally, chapter 7 concludes the thesis with a summary of the achievements and remarks for future work.

1

REFERENCES

[1] D. G. Victor, A. M. Jaffe, and M. H. Hayes, *Natural Gas and Geopolitics: From 1970 to 2040* (Cambridge University Press, 2006).

[2] *NL Oil and Gas Platform*, Report (TNO-Geological Survey of the Netherlands).

[3] *Report on Gas Composition*, Report (Directoraat-generaal voor Energie, Telecom en Markten, 2011).

[4] J.-F. Auger, C. Jepma, and B. Wiersema, *A research program on the gas infrastructure in the Netherlands,* Network Industries Quarterly **12**, 3 (2010).

[5] G. de Graaf, F. Bakker, and R. F. Wolffenbuttel, *Sensor platform for gas composition measurement,* Procedia Engineering **25**, 1157 (2011).

[6] F. G. Shinskey, *Chapter 2 - Combustion control systems,* in *Energy Conservation Through Control* (Academic Press, 1978) pp. 39–67.

[7] S. Gersen, M. van Essen, G. van Dijk, and H. Levinsky, *Physicochemical effects of varying fuel composition on knock characteristics of natural gas mixtures,* Combustion and Flame **161**, 2729 (2014).

[8] V. Van Essen, H. De Vries, and H. Levinsky, *Possibilities for admixing gasification gases: Combustion aspects in domestic natural gas appliances in the Netherlands,* in *International Gas Union Research Conference.*

[9] G. F. Fine, L. M. Cavanagh, A. Afonja, and R. Binions, *Metal oxide semi-conductor gas sensors in environmental monitoring,* Sensors **10**, 5469 (2010).

[10] T. Seiyama, A. Kato, K. Fujiishi, and M. Nagatani, *A new detector for gaseous components using semiconductive thin films,* Analytical Chemistry **34**, 1502 (1962).

[11] X. Liu, S. Cheng, H. Liu, S. Hu, D. Zhang, and H. Ning, *A survey on gas sensing technology,* Sensors **12**, 9635 (2012).

[12] Z. Ting, M. Syed, V. M. Nosang, and A. D. Marc, *Recent progress in carbon nanotube-based gas sensors,* Nanotechnology **19**, 332001 (2008).

[13] R. H. Poelma, B. Morana, S. Vollebregt, E. Schlangen, H. W. van Zeijl, X. Fan, and G. Q. Zhang, *Tailoring the mechanical properties of high-aspect-ratio carbon nanotube arrays using amorphous silicon carbide coatings,* Advanced Functional Materials **24**, 5737 (2014).

[14] B. Esser, J. M. Schnorr, and T. M. Swager, *Selective detection of ethylene gas using carbon nanotube-based devices: Utility in determination of fruit ripeness,* Angewandte Chemie International Edition **51**, 5752 (2012).

[15] D. O. de Sa, *Instrumentation Fundamentals for Process Control* (CRC Press, 2001).

[16] J. G. Firth, A. Jones, and T. A. Jones, *The principles of the detection of flammable atmospheres by catalytic devices,* Combustion and Flame **20**, 303 (1973).

[17] Y. Deng, T. G. Nevell, R. J. Ewen, and C. L. Honeybourne, *Sulfur poisoning, recovery and related phenomena over supported palladium, rhodium and iridium catalysts for methane oxidation,* Applied Catalysis A: General **101**, 51 (1993).

[18] B. Sharma, *Instrumental Methods of Chemical Analysis* (Krishna Prakashan Media, 2000).

[19] B. G. Liptak, *Analytical Instrumentation* (CRC Press, 1994).

[20] P. Gründler, *Chemical Sensors: An Introduction for Scientists and Engineers* (Springer Science & Business Media, 2007).

[21] L. T. White, *Chapter 4 - Hazardous gas monitoring sensors,* in *Hazardous Gas Monitoring (Fifth Edition)* (William Andrew Publishing, 2001) pp. 81–116.

[22] A. Drews, *Manual on Hydrocarbon Analysis*, Vol. 3 (ASTM International, 1989).

[23] K. Nachef, F. Marty, E. Donzier, B. Bourlon, K. Danaie, and T. Bourouina, *Micro gas chromatography sample injector for the analysis of natural gas,* Journal of Microelectromechanical Systems **21**, 730 (2012).

[24] D. Gaddes, J. Westland, F. L. Dorman, and S. Tadigadapa, *Improved micromachined column design and fluidic interconnects for programmed high-temperature gas chromatography separations,* Journal of Chromatography A **1349**, 96 (2014).

[25] S. Narayanan, G. Rice, and M. Agah, *Characterization of a micro-helium discharge detector for gas chromatography,* Sensors and Actuators B: Chemical **206**, 190 (2015).

[26] M. Yang, T.-Y. Kim, H.-C. Hwang, S.-K. Yi, and D.-H. Kim, *Development of a palm portable mass spectrometer,* Journal of the American Society for Mass Spectrometry **19**, 1442 (2008).

[27] J. A. Dziuban, J. Mróz, M. Szczygielska, M. Małachowski, A. Górecka-Drzazga, R. Walczak, W. Buła, D. Zalewski, . Nieradko, J. Łysko, J. Koszur, and P. Kowalski, *Portable gas chromatograph with integrated components,* Sensors and Actuators A: Physical **115**, 318 (2004).

[28] M. Akbar, M. Restaino, and M. Agah, *Chip-scale gas chromatography: From injection through detection,* Microsystems and Nanoengineering **1**, 15039 (2015).

[29] Agilent Technologies, *4100 ExoScan Series FTIR,* Accessed: 27.05.2016.

[30] J. Hodgkinson and R. P. Tatam, *Optical gas sensing: a review,* Measurement Science and Technology **24**, 012004 (2013).

[31] N. Tkachenko, *Optical Spectroscopy: Methods and Instrumentations* (Elsevier Science, 2006).

[32] S. Thiele and R. Salzer, *Optical spectroscopy,* in *Handbook of Spectroscopy* (Wiley, 2003) pp. 441–468.

2

From Benchtop Spectrometers to Portable Microspectrometers

THE need for a low-cost and robust sensor for natural gas analysis at many nodes in the grid (potentially in every burner) necessitates miniaturization at the wafer-level for batch fabrication. Optical absorption spectroscopy is a self-referencing and nondestructive method that is highly suitable for hydrocarbon analysis in the mid-IR. However, it is a challenge to miniaturize an absorption spectrometer to the wafer-level, while maintaining the selectivity, sensitivity and robustness. In this chapter, several optical absorption spectroscopy methods are described and the miniaturization approaches that led to the development of the gas-filled linear variable optical filter (LVOF) are investigated.

2.1. OPTICAL ABSORPTION SPECTROMETERS

Optical absorption spectrometers are composed of a light source, a wavelength-selective element, a sample cell, a detector and optical components to steer the light beam. The key component that sets the resolution of the entire system is the wavelength-selective element. Wavelength selection can be implemented either in the light source or as a separate component. In this section, both methods with their suitability for miniaturization are analyzed.

2.1.1. WAVELENGTH SELECTIVITY IMPLEMENTED AT THE LIGHT SOURCE

Lasers are commonly preferred in spectral analysis due to their high power, narrow linewidth and long coherence length [1]. In laser absorption spectroscopy, the wavelength selection is implemented in the light source, where the laser either emits a single wavelength or is tunable. The laser based systems are very suitable for the analysis of low-concentration gases due to their high power, high resolution and long coherence length. The sensitivity can be further improved by applying modulation techniques in wavelength [2] or frequency [3], as well as increasing the absorption path length. In cavity enhanced absorption spectroscopy (CEAS), either an internal or an external cavity is included to increase the absorption path using multiple reflections. An external cavity can be a multipass cell with nonplanar mirrors to confine the light beam such as the White cell [4], the Herriott cell [5] and a circular multipass cell [6, 7] or a resonant etalon such as Fabry-Perot (FP). The FP type cavities are capable of achieving very long optical paths due to the high reflectivity of the mirrors. However, matching the resonating frequency of the laser to that of the FP cavity becomes a problem in these systems. Cavity ringdown spectroscopy bypasses this limitation by sending a pulsed signal to the cavity and subsequently measuring decay rate of the circulating light beam transmission in time [8]. The decay rate is then translated into sample concentration, given the physical dimensions of the cavity.

Mid-IR is an important wavelength range for gas monitoring due to the distinguishing spectral features of gases such as hydrocarbons (CH_4, C_2H_6, C_3H_8, C_4H_{10}), carbon monoxide (CO), carbon dioxide (CO_2), etc. Several examples of parametric oscillator [9, 10], semiconductor such as quantum cascade laser (QCL) [11], fiber [12, 13] and solid-state [14] lasers have been presented in the literature. In spite of its high sensitivity and resolution, laser spectroscopy is still far from wafer-level miniaturization.

2.1.2. SEPARATE WAVELENGTH-SELECTIVE ELEMENT

The second way to divide the spectrum into different wavelengths is to combine a wideband source with a wavelength-selective element. This component can be dispersive as in a grating based spectrometer, interferometric as in an FTIR spectrometer or an optical filter.

GRATING BASED SPECTROMETERS

Gratings are commonly used as both monochromators in research labs and wavelength-selective components in commercial spectrometers. They can be employed either as transmissive or reflective elements. The repetitive series of narrow grooves in a grating allow the incident light to be diffracted at different angles [15]. The operating principle is governed by the grating equation $a(\sin\theta_m + \sin\theta_i) = m\lambda$ for the reflective configuration, where a is the grating pitch, θ_i is the angle of incidence, θ_m is the angle of diffraction, m is the diffraction order and λ is the wavelength. For monochromatic incidence, different orders are diffracted at different angles at a given grating pitch. Similarly, a wideband incident illumination is separated into different wavelengths at different angles at a particular diffraction order. Therefore, a wideband light source can be divided into separate wavelengths either by combining a grating with a detector array to convert the angular separation into lateral position or by using a single detector element and rotating the grating to measure one wavelength at each step.

The biggest limitation in the performance of gratings is the optical throughput. In a conventional grating with flat surfaces, most of the incident light reflects off the grating without a wavelength-dependent pattern at the 0^{th} order. Blazed gratings overcome this limitation by creating a tapered grating structure to achieve maximum grating efficiency at the desired diffraction order. Particularly, in the Littrow configuration for blazed gratings, maximum efficiency is achieved at the 1^{st} order, while the light is diffracted from the grating back to the source [16]. Moreover, a special type of blazed grating, the sinusoidal shaped holographic grating, reduces ghosting and scattering; however, suffers from degraded efficiency.

Miniaturization of grating based spectrometers has been of great interest toward the use in portable applications [17, 18]. Compact microspectrometers in the visible extend-

ing to the near-IR [19–23] and mid-IR [24] ranges have been reported in the literature. Despite their compactness, grating based spectrometers are not suitable for wafer-level miniaturization and power efficiency becomes an issue in the infrared, where low-cost light sources suffer from limited output power.

FTIR SPECTROMETERS

Fourier transform infrared (FTIR) spectroscopy relies on converting the raw interferometric data into a spectrum by Fourier transform. FTIR spectroscopy has several advantages compared to dispersive methods. The entire spectrum is measured simultaneously in an FTIR spectrometer, whereas the spectrum is constructed from individual narrowband measurements in dispersive spectrometers. The noise in spectral measurements usually arises from the detector in the infrared [25]. Therefore, the signal-to-noise (SNR) of the measurements of a single spectral feature is proportional to the measurement time. Since the entire spectrum is measured at once in an FTIR spectrometer, the ratio of the SNR of an FTIR spectrometer to that of a dispersive spectrometer is proportional to the square root of the number of spectral elements. This improvement in the noise performance is known as the multiplex or the Fellgett advantage [26]. Moreover, Jacquinot investigated the etendue in grating based and FTIR spectrometers. For dispersive instruments, the throughput is limited by the size of the entrance slit. Compared to the grating based spectrometers, FTIR spectrometers offer an improvement in terms of etendue, which is known as Jacquinot or throughput advantage [27]. The last advantage of FTIR spectroscopy over dispersive spectroscopy is about calibration. FTIR spectrometers use a HeNe laser at 632.8 nm wavelength to derive the wavenumber scale of the spectrum, which is regarded as internal calibration. The wavelength of an HeNe laser is very stable and accurate. Therefore, FTIR spectrometers do not require additional external calibration. Grating based spectrometers on the other hand need to be calibrated periodically. This is known as the Connes advantage and renders FTIR spectroscopy a very reliable method [28].

The key component in an FTIR spectrometer is the interferometer. Conventionally, Michelson interferometers are employed in FTIR systems. These interferometers are composed of one stationary and one moving mirror, where the light is divided into two parts in amplitude by a beam splitter [29]. The wideband interference of light is ensured by creating an optical path difference between these mirrors through mechanical movement. Much attention has been paid to the miniaturization of the interferometer. Microelectromechanical systems (MEMS) implementations of the moving mirror in the Michelson interferometer has been presented in the literature [30–32]. Moreover, on-chip Michelson interferometers with both etched [33] and pop-up mirrors [34] have been demonstrated. In addition, lamellar grating interferometers are introduced as a

relatively robust substitute for Michelson interferometers. In the lamellar grating structure, stationary and moving mirrors are combined in a single MEMS device, while the use of a beam splitter is eliminated. The 0^{th} order is collected by a detector for Fourier analysis. Miniaturized lamellar grating interferometers have also been demonstrated [35–37]. Despite the marginal improvement in the latter, wideband operation of both interferometers still rely on moving parts. Also, in an on-chip configuration, the vertical arrangement of the mirrors does not allow for bottom-up integration with the rest of the components, which hinders the wafer-level miniaturization of the whole system. Examples of MEMS implementations are shown in Fig. 2.1.

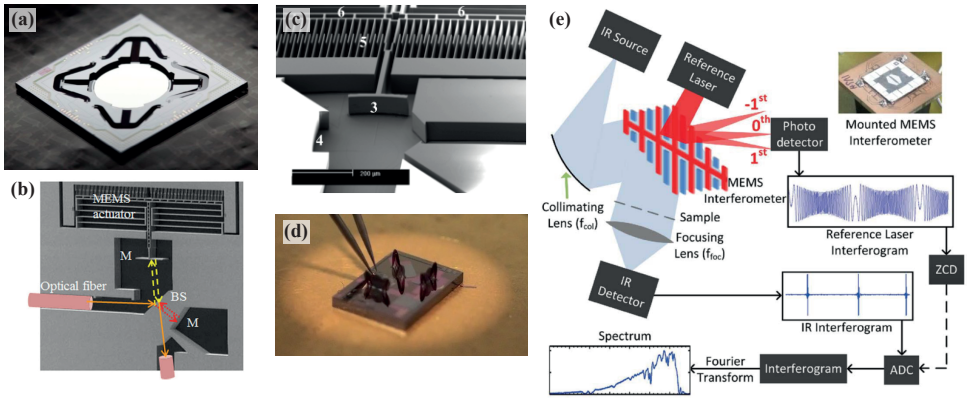

Figure 2.1: (a) MEMS piston device featuring a mirror plate of 5 mm diameter elevated by four pantograph suspensions that enable large strokes [32]. (b) Monolithically integrated micromachined Michelson interferometer. BS stands for beam splitter and M stands for mirror [33]. (c) Scanning electron microscopy (SEM) photograph of the electrostatic actuator, showing the movable (3) and the fixed mirror (4), the electrostatic comb actuator (5) and the suspension beams (6), [30]. (d) Monolithic MEMS Michelson interferometer with pop-up mirrors [34]. (e) Schematic of a lamellar grating based FTIR spectrometer. ZCD stands for zero-crossing detector and ADC stands for analog-to-digital converter. All figures are reprinted with permission.

OPTICAL FILTER BASED SPECTROMETERS

Optical filter based spectrometers use interference filters to separate the light into different wavelengths and are highly suitable for miniaturization [38]. Interference filters, i.e. FP resonators, are composed of two parallel mirrors with a resonator layer in-between. The thickness of the resonator determines the wavelength to be transmitted. The wideband operation of these filters is achieved either by an array of fixed filters with different resonator thicknesses or by mechanically moving one of the mirrors, i.e. tunable FP filter. In both configurations, the mirror parallelism is crucial for high resolution. In an array of fixed filters, high-parallelism can be achieved by a fine-tuned fabrication process, while the number of spectral channels; hence, the spectral resolving power of the spectrometer is limited by the number of filters. In tunable FP filters, continuous mechanical

movement of one of the mirrors allows for more spectral channels, thereby increasing the spectral resolving power, whereas mirror parallelism and robustness become issues. Miniaturized implementations of both arrays of fixed filters [39–41] and tunable filters [42–46] have been demonstrated for microspectrometer applications.

The linear variable optical filter combines the high spectral resolving power of a tunable filter with the robustness of an array of fixed filters. The LVOF is composed of one flat and one slightly tilted mirror with a tapered resonator in-between and is usually treated as a continuous array of fixed FP filters [47]. The thickness of the resonator, which can be air as well as an optical material, varies linearly as the filter is scanned along its length; hence, when combined with a detector array, a wideband spectral response can be obtained. Several MEMS implementations of LVOFs have been presented [48–50] in the literature.

Due to the wideband operation capability in a robust structure and eligibility for wafer-level miniaturization, LVOF is chosen as the wavelength-selective component of the microspectrometer developed in this thesis.

2.2. MINIATURIZATION OF SPECTROMETER COMPONENTS

The miniaturization of an optical filter based MEMS gas sensor requires the integration of a light source, a gas cell, a filter, a detector and optical elements. Several research groups have done substantial work related to miniaturization and integration of these components. At VTT, Finland, miniaturized tunable FP filter based portable spectrometers are developed [51]. In 2013, a compact spectrometer as shown in Fig. 2.2 for detecting hydrocarbons in the 3 µm to 3.5 µm wavelength range with a spectral resolution of 50 nm to 60 nm and an optical path length of 17 mm was reported. However, the filter, a lead-selenide (PbSe) detector and a pulsed broadband infrared emitter light source are combined at the component level, rather than monolithic integration [52].

Figure 2.2: The handheld hydrocarbon spectrometer in the gas measurement mode from VTT [52]. Reprinted with permission.

Another research group uses the flip chip method to integrate an array of fixed FP filters with a thermopile detector array in the mid-IR region [53, 54]. Mixtures of carbon

monoxide (CO), carbon dioxide (CO_2) and methane (CH_4) with a total concentration of 1000 ppm have been tested using a commercial IR emitter and an external absorption cell with 10 cm path length. Measurement errors in the range of tens of ppm were reported. Infratec demonstrated a tunable FP filter mounted on top of a pyroelectric detector that operates in the 3 µm to 4.3 µm and 3.7 µm to 5 µm wavelength ranges [55]. Lastly, a research group from the University of Western Australia published a tunable FP filter that is monolithically integrated to a Mercury Cadmium Telluride (MCT) detector in the 1.6 µm to 2.5 µm wavelength range [56]. More recent results were obtained in the 3 µm to 5 µm wavelength range, however monolithic integration of filter and detector was not pursued [57]. Wu *et al.* investigated the hybrid integration of a thermopile array that enhances the detection with a thin-film absorber and an LVOF that operates in the mid-IR; however, the actual integration was not realized [58].

Despite all the efforts on miniaturized gas sensors for natural gas analysis, there are still important gaps to fill. A very important one is the miniaturization and the integration of the light source, the gas cell, the filter, the detector, and the optics at the wafer-level for batch fabrication. Various MEMS implementations of these components have already been presented in the literature. However, the sample chamber which is used for storing the sample gas to be measured takes up most of the volume in a microspectrometer and is the only component that has not been miniaturized yet. In the rest of this chapter, the functional integration of the LVOF with an on-chip gas cell is discussed.

2.2.1. ON-CHIP OPTICAL ABSORPTION PATH USING PLANAR MIRRORS

Initial effort is devoted to the integration of the different functional components of a spectrometer in two wafers. One of the wafers hosts the light source as well as the combination of the optical filter and the detector. The other wafer is composed of two 45° inclined mirrors facing each other, while the space in-between is used as the optical absorption path.

Fabrication of 45° inclined mirrors using simple wet etching methods has been previously reported in the literature. The topic is of interest to the telecommunications community, due to the requirement of low-cost devices for efficient fiber coupling. By aligning the etch mask in the <100> direction in a (100) wafer, 45° inclined mirrors can be easily fabricated on the {110} planes by wet etching [59, 60]. Crystallographic alignment can be further improved compared to the angular alignment with respect to the primary flat of the wafer by observing pre-etched test structures [61–63]. Moreover, by adding a surfactant such as Triton X-100 to the KOH or the TMAH solution, the surface quality of the mirror can be improved immensely [64]. Several 45° inclined mirrors on the {110} plane were fabricated using a rotated SiN mask with 10 mm by 10 mm openings as shown in Fig. 2.3.

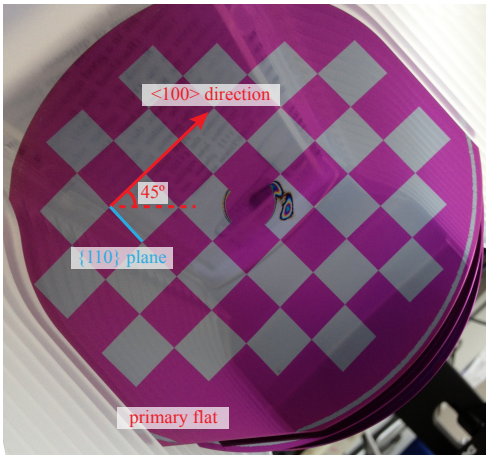

Figure 2.3: Wafer after lithography and development steps with a 10 mm by 10 mm checker pattern.

First wet etching experiments were performed with TMAH, where a solution of 25% TMAH + 200 ppm Triton X-100 at 75 °C was used. 45° inclined mirrors were achieved on the {110} plane at an etch rate of 0.21 µm/min. However, randomly located pyramids were formed on the {100} plane as shown in Fig. 2.4. Since these pyramids are in the light path, they could block the light and decrease the throughput.

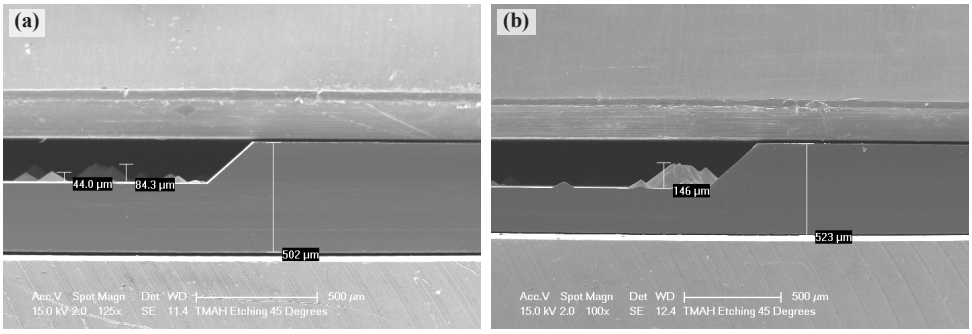

Figure 2.4: SEM images of 45° inclined mirrors etched (a) 198 µm and (b) 262 µm deep using 25% TMAH + 200 ppm Triton X-100 at 75 °C.

For KOH etching, a solution with 2 M KOH + 60 ppm Triton X-100 at 90 °C is prepared. KOH etching with the surfactant Triton X-100 resulted in smooth inclined surfaces as shown in Fig. 2.5. The etch rate is calculated as 0.10 µm/min. In contrast to the TMAH etching, the KOH etching resulted in roughness-free {100} planes, thereby allowing a light path without randomly formed structures.

The surface roughness of the etched mirrors are measured using atomic-force mi-

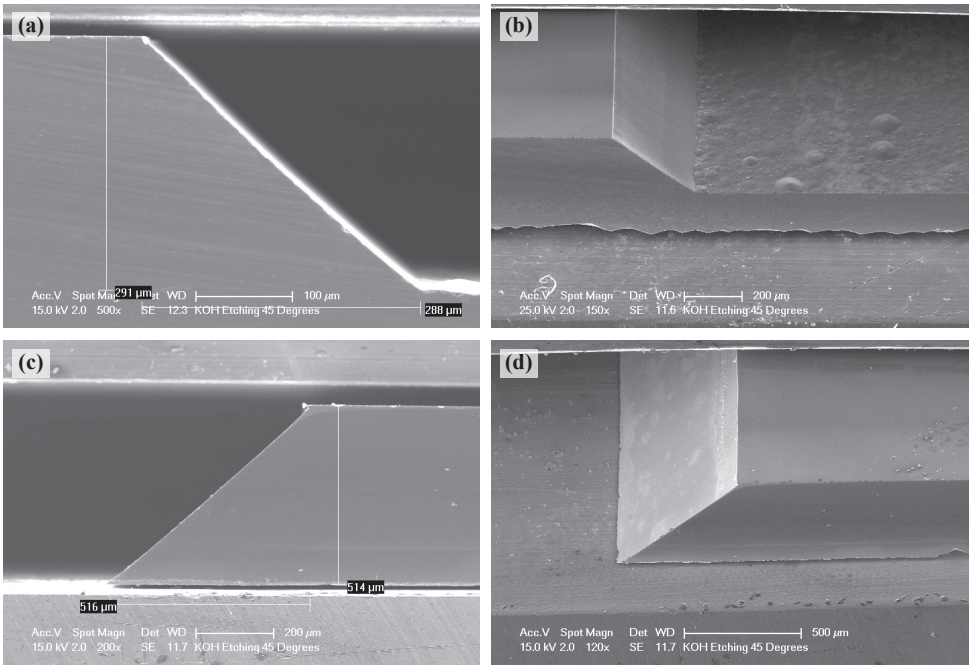

Figure 2.5: SEM images of 45° inclined mirrors etched (a, b) 290 µm deep and (c, d) through the Si wafer using 2 M KOH + 60 ppm Triton X-100 at 90 °C.

croscopy. The mirrors are diced along the edges and placed on a 45° inclined wedge to obtain a flat surface for roughness analysis as shown in Fig. 2.6. Double sided tape is used for attaching the mirror to the wedge. The measured root-mean-square (RMS) roughness values are below 15 nm, safely within the optical flatness limit of $\lambda/10$, considering the mid-IR wavelength range of 3 µm to 5 µm.

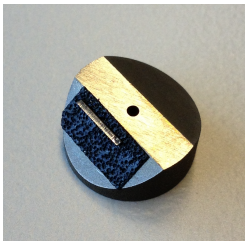

Figure 2.6: 45° inclined wedge used in AFM measurements.

The power efficiency of a system with 45° inclined mirrors is analyzed using the ray tracing software, Zemax. The simplified system is composed of a light source, two 45° inclined mirrors with a 10 mm long optical light path in-between and an image plane

as shown in Fig. 2.7. The light source is implemented as a cylindrical lens to realize a filament-like IR emitter. The cylindrical lens is designed as a toroidal surface with infinite radius of rotation. The diameter of the cylinder is 0.06 mm, while the length is 3 mm. The size of the entrance pupil diameter is selected as 3 mm so that the entire cylindrical lens surface is illuminated. The size of the 45° inclined mirrors is maximized to demonstrate the best-case efficiency. The largest mirror can be achieved by through-wafer etching, therefore the width of the mirror is selected as 0.74 mm assuming a standard 4" wafer thickness of 524 µm. The cylindrical lens and the image plane are placed 0.5 mm away from the mirrors.

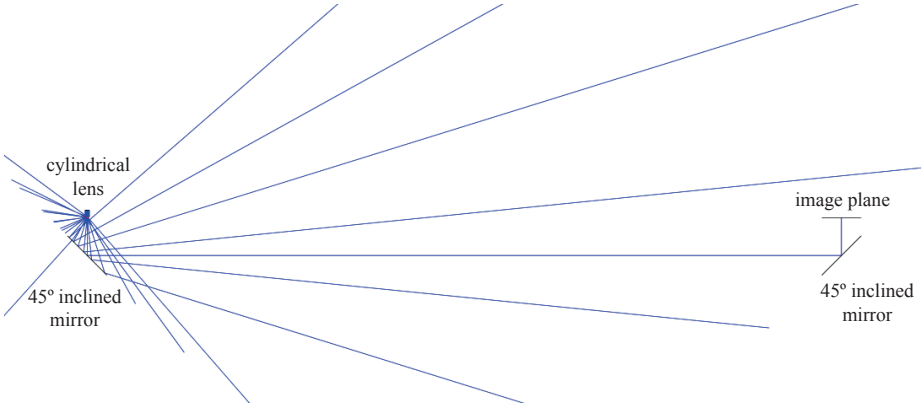

Figure 2.7: The Zemax layout of the on-chip optical absorption path with 45° inclined mirrors.

Geometric image analysis in the sequential mode of Zemax is used for power simulations. This type of analysis assumes a unit power of 1 W at the initial surface and calculates the power distribution at every surface based purely on geometrical optics. Power analysis results for the system with 45° inclined mirrors are given in Fig. 2.8. Since the cylindrical lens is going to be the light source in the actual implementation, the power at the image plane is normalized to the power at the cylindrical lens rather than the entrance pupil. This results in the best-case power efficiency of 1.1%. However, through-wafer etching, despite maximizing power efficiency, impairs the robustness of the entire system. Moreover, the stray light that does not follow the predefined optical path makes the quantitative material identification, which depends highly on the length of the optical absorption path, unreliable. In addition, the fabrication tolerances could easily decrease the efficiency below 1.1%, which is undesirable in systems with low-power wideband IR emitters. Therefore, despite their common use in coupling collimated light beam in telecommunications, the efficiency of a system with 45° inclined mirrors decreases sharply when combined with a wideband emitter without any collimating optics.

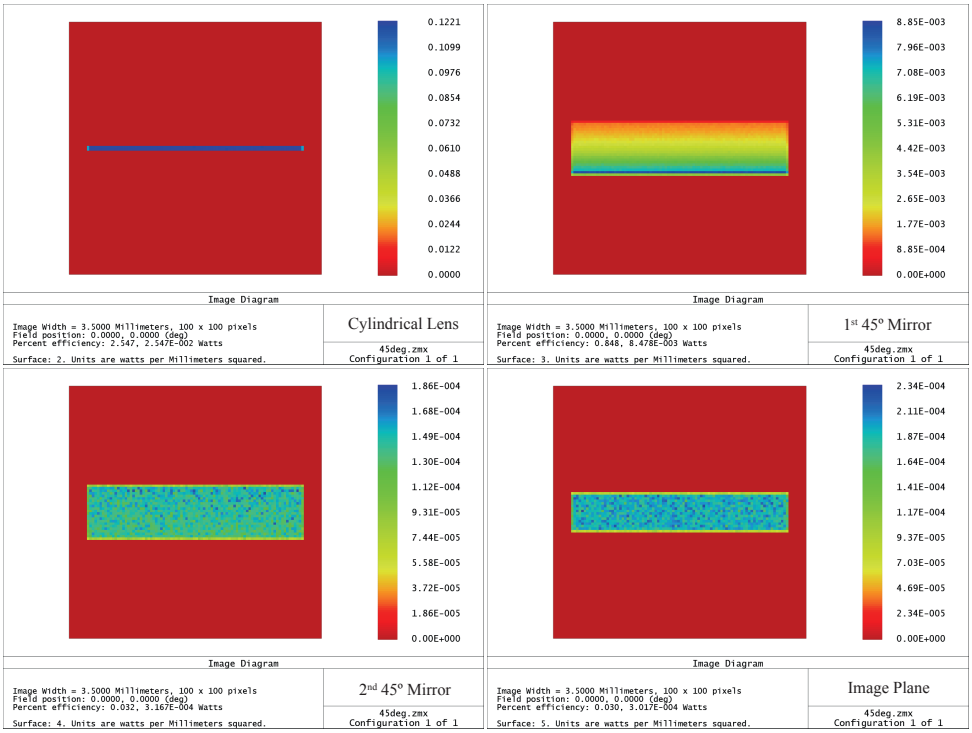

Figure 2.8: The results of the power analysis of the on-chip optical absorption path with 45° inclined mirrors.

2.2.2. ON-CHIP OPTICAL ABSORPTION PATH USING PARABOLIC MIRRORS

An optical system with an on-chip optical absorption path that lies on the surface of a wafer requires at least two mirrors; one for collimating the diverging light source and one for focusing the light onto the detector. A parabolic mirror is capable of focusing parallel incident rays perfectly, while spherical mirrors suffer from aberration. Therefore, in most optical systems where collimation of a broadband diverging source is required, parabolic mirrors are employed. It has been shown that such aspherical mirrors can be fabricated using simple techniques [65, 66].

In this section, an optical system that consists of a diverging light source, two off-axis parabolic mirrors, an on-chip optical absorption path and a detector is investigated. As shown in Fig. 2.9, bottom wafer (blue) includes two parabolic mirrors and the sample gas cell in-between. Top wafer (grey), which is bonded to the bottom one includes the light source and the combination of the LVOF and the detector array. The light beam is shown in semi-transparent orange.

The light source is identical to the implementation of the IR emitter as a cylindrical lens in the system with 45° inclined mirrors. The parabolic mirror is realized as a non-

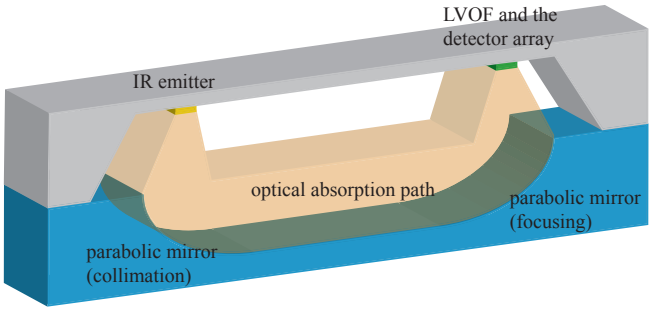

Figure 2.9: A schematic illustration of the envisaged optical system.

rotationally symmetric polynomial surface with the formula $y = x^2$. The focal length of a parabola defined with the formula $y = ax^2 + bx + c$ is $f = 1/4a$, therefore the focal length of the parabola designed in Zemax has a focal length of 0.25 mm. The size of the mirror (d), i.e. the height, is defined as the distance between the top and the bottom parts of the mirror and is limited by the wafer thickness. The maximum size that can be attained is 524 µm assuming through wafer etching. However, this deteriorates the robustness of the mirrors as well as the entire sensor system. Furthermore, the portion of the parabolic surface that is employed in the system plays an important role as well, especially in terms of fabrication limitations. Introducing decentering allows us to choose the part of the parabola that is defined by the aforementioned formula. Decenter ($dcntr$) is defined as the distance between the axis of symmetry and the centre of a rectangular frame around the selected parabola portion. Parabolic mirrors defined by the formula $y = x^2$ with d = 1.2 mm size and different decentering values are shown in Fig. 2.10 for clarification.

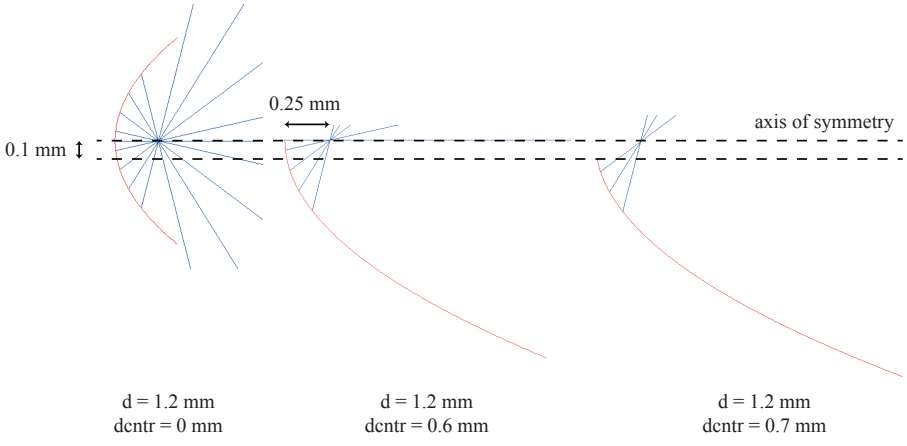

Figure 2.10: Polynomial surface $y = x^2$ with d = 1.2 mm size for various decentering values.

The cylindrical lens is placed at the focal point of the polynomial surface, which is also 3 mm long. After the light gets collimated at the first polynomial surface, it propagates through the sample gas for an optical path length of 10 mm. Later, it gets collected by the second polynomial surface, which is identical to the first one. Lastly, the light gets focused on the image plane that is located at the focal point of the second polynomial surface as shown in Fig. 2.11.

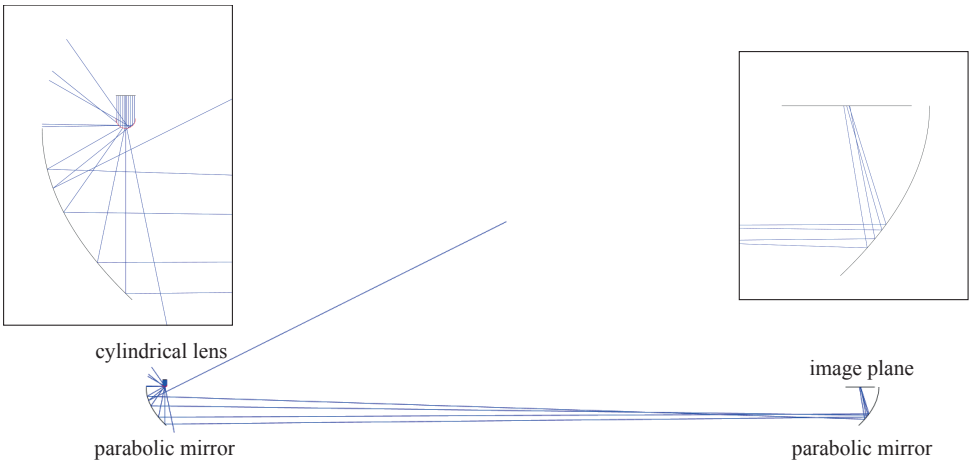

Figure 2.11: The Zemax layout of the on-chip optical absorption path with parabolic mirrors.

For the power simulations of the parabolic mirror based system, geometric image analysis in the sequential mode of Zemax is used as well. The results of the power analysis for a 400 µm mirror decentered for 400 µm are given in Fig. 2.12. A quick comparison between Fig. 2.8 and Fig. 2.12 in terms of the power of the light collected at the image plane already shows a factor of 10 improvement in the efficiency of the design with parabolic mirrors over the design with 45° inclined mirrors.

The effect of the mirror size and decentering on the optical efficiency of the system is further investigated by similar power analyses. The decentering value is swept from 0 µm to 800 µm with 8 µm steps for various mirror sizes, while the changes are applied to both of the parabolic mirrors simultaneously. The results are summarized in Fig. 2.13.

As the mirror size increases, the power at the image plane increases as well. However, for each mirror size, there is a decentering value at which maximum power is achieved at the image plane as listed in Table 2.1. These are the peaks of the plots in Fig. 2.13.

There is a huge power loss at the cylindrical lens due to the circular shape of the entrance pupil compared to the narrow rectangular aperture of the cylindrical lens. Since the filament will be the light source in the actual device, the power values at the image plane are normalized to the power at the cylindrical lens, as given in the last column of

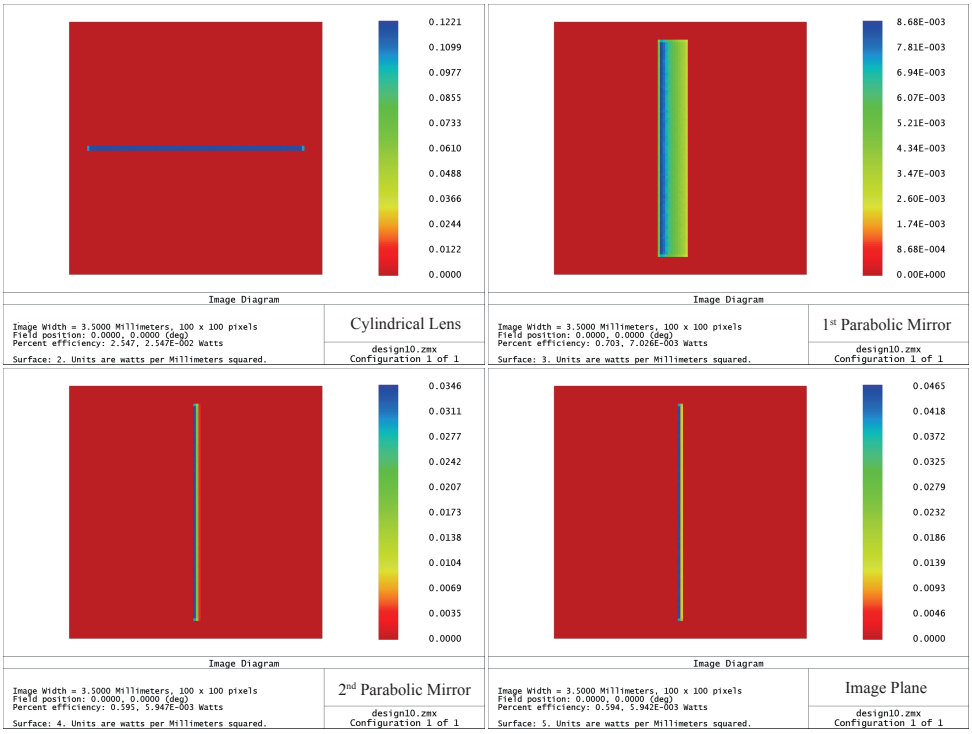

Figure 2.12: The results of the power analysis of the on-chip optical absorption path using off-axis parabolic mirrors with $d = 400\mu m$ and $dcntr = 400\mu m$.

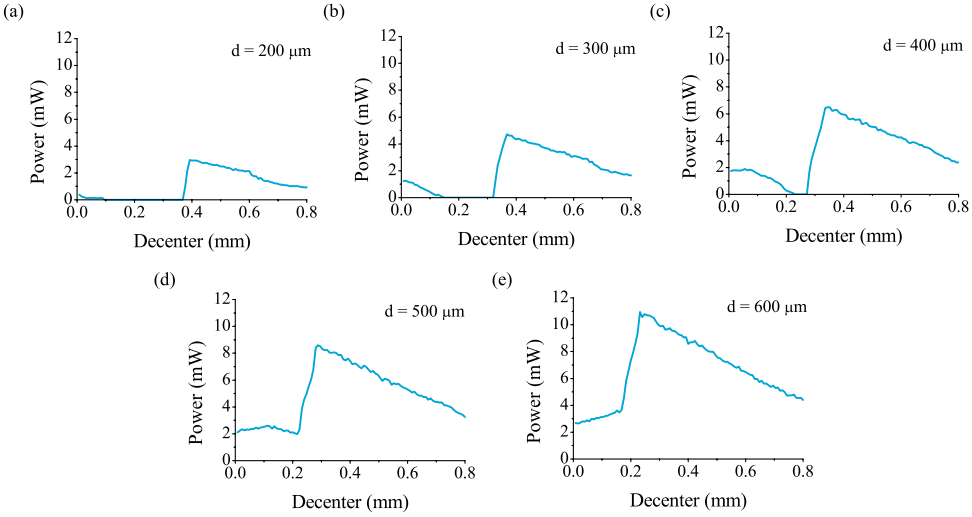

Figure 2.13: Simulation of the power at the image plane for a parabolic mirror with (a) $d = 200\mu m$, (b) $d = 300\mu m$, (c) $d = 400\mu m$, (d) $d = 500\mu m$, (e) $d = 600\mu m$.

Table 2.1. The simulation shows that approximately 42% of the incident light can reach the image plane in the best case with a $d = 600\,\mu m$ sized mirror that is decentered for $232\,\mu m$. However, this is an hypothetical mirror, which is larger than the thickness of a standard wafer. While a power efficiency of about 33% can be achieved by a $d = 500\,\mu m$ sized mirror, robustness of the whole system would be impaired. Therefore, a $d = 400\,\mu m$ sized mirror offers a good compromise between system robustness and power efficiency.

Table 2.1: Mirror size comparison in terms of power efficiency. Optimum decentering is the decentering value at which maximum power at the image plane is obtained. Power efficiency is calculated as $\frac{P_{imageplane}}{P_{cylindricallens}} \times 100$.

Mirror size, d (µm)	Optimum decentering (µm)	Maximum power (mW)	Power efficiency (%)
200	408	3.053	11.97
300	368	4.470	17.53
400	344	6.624	25.97
500	296	8.484	33.27
600	232	10.818	42.42

The detailed drawing of a $400\,\mu m$ sized mirror with $344\,\mu m$ decentering is given in Fig. 2.14. The x and y coordinates of the top, the bottom, and the focal point of the blue coloured mirror are provided in the figure. Note that the x and y axes are interchanged as compared to their conventional direction, since the plot is rotated 90° clockwise to be consistent with the Zemax design parameters.

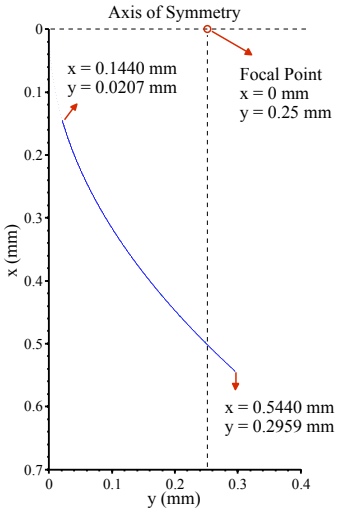

Figure 2.14: Detailed drawing of the mirror with $400\,\mu m$ size and $344\,\mu m$ decentering.

Although the solution shown above is the best case in simulation, the uncertainty

that the fabrication introduces might result in a sharp decrease in power efficiency, especially for lower decentering values, as shown in Fig. 2.13(c). Therefore, to account for such uncertainties, a tolerance simulation for 400 µm sized mirrors with decentering values of both 344 µm (best case) and 400 µm (safe case) is performed. A random error with maximum 10%, 20%, and 30% of the initial value is added to the polynomial surface defined with $y = x^2$. The new surface is described as y_{err} as given in Eq. 2.1.

$$y = x^2 \rightarrow y_{err} = x^2 + \underbrace{x^2 \frac{\%\ \text{error}}{100} \overbrace{(-1 + 2\ \text{rand})}^{\text{random number in } [-1:1]}}_{\text{total error}} \tag{2.1}$$

The definition of the new surface is limited to only the first four even terms of the polynomial in the sequential mode of Zemax. Therefore, the new dataset with error is fit to a polynomial with the terms x^2, x^4, x^6, and x^8 in Matlab. The polynomial plots including both cases (i.e. x varies from 144 µm to 600 µm) without error, with error and the polynomial fit of the latter are shown for 10%, 20%, and 30% error in Fig. 2.15. Note that the same random number set is used for all cases.

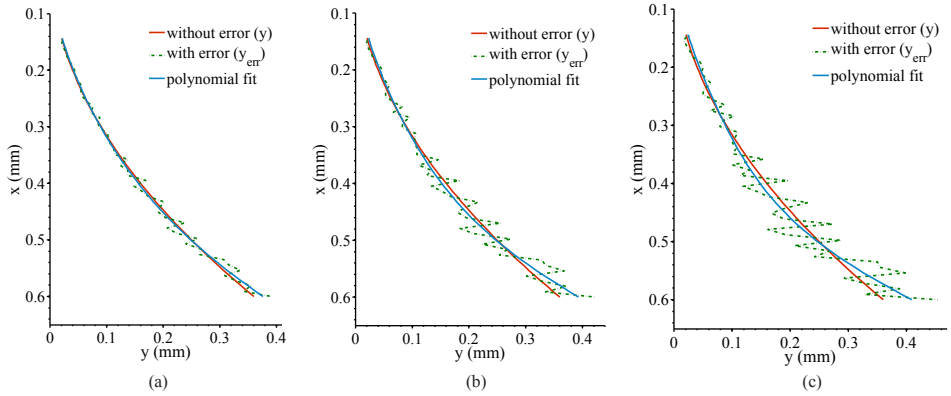

Figure 2.15: Polynomial plot covering a 400 µm sized mirror with both 344 µm (best case) and 400 µm (safe case) decentering with (a) 10%, (b) 20%, and (c) 30% error.

The coefficients acquired for these four terms with 10%, 20%, and 30% error are listed in Table 2.2, along with the respective power at the image plane and power efficiency values. The ideal values (i.e. without error) are also provided in the table. These results show that the mirrors are very sensitive to variations in the polynomial surface. Even with a maximum 10% error, the power efficiency of the best case decreased from 25.97% to 5.4%, which translates into almost 80% decline in performance. Since the error introduced in this study is random, it is not possible to conclude that this is the best or the worst case scenario. However, it is obvious that even small variations in the surface pro-

file have a tremendous effect on the collimating property of parabolic mirrors. Therefore, the on-chip optical absorption path with parabolic mirrors is not pursued in this study.

Table 2.2: Tolerance simulation details and results for a 400 µm sized mirror with 344 µm (best case) and 400 µm (safe case) decentering.

Error	No error	10%	20%	30%
Coefficient of x^2	1	1.0884	1.1768	1.2652
Coefficient of x^4	0	-1.5922	-3.1844	-4.7765
Coefficient of x^6	0	6.7163	13.4325	20.1488
Coefficient of x^8	0	-7.2831	-14.5663	-21.8494
Power at the image plane (best case)	6.624	1.378	1.086	0.985
Power at the image plane (safe case)	6.015	0.594	0.262	0.167
Power efficiency (best case)	25.97	5.40	4.25	3.86
Power efficiency (safe case)	23.58	2.33	1.03	0.65

2.2.3. GAS-FILLED LVOF

Collimation of the light and simultaneously steering it in the right direction with negligible power loss is a challenging objective. The efficiency of such a system would be significantly reduced when also considering the fabrication tolerances. Moreover, the stray light that is not collimated properly might reach the detector and deteriorate the performance of the microspectrometer. Therefore, a miniaturization approach that is not susceptible to the fabrication uncertainties is required.

The operating principle of the LVOF relies on the interference of the light that is reflected multiple times in the resonator layer between the mirrors. The wavelength to be transmitted through the filter is governed by the simplified interference equation $2nh = \lambda m$, where n is the refractive index of the resonator layer, h is the thickness of the resonator, λ is the wavelength to be transmitted and m is the operating order. Therefore, the wavelength to be transmitted is directly related to the thickness of the resonator. Since the wideband response of an LVOF is achieved by tapering the resonator layer and scanning the filter along its length, minor fabrication tolerances only shift the position of the transmission at a certain wavelength on the filter. Thus, the resonator thickness is usually doubled to account for the fabrication tolerances. The positional shift of the transmission at a particular wavelength can be later characterized with a single-wavelength calibration.

The low susceptibility to fabrication tolerances and the robustness that arises from achieving wideband operation without any moving parts makes the LVOF a highly suitable candidate for wafer-level miniaturization of spectrometers. Instead of combining the LVOF with an external sample chamber, as shown in Fig. 2.16(a), the resonator layer can be replaced with a cavity and used as a gas cell as shown in Fig. 2.16(b). In CEAS, the

multiple reflections in high-finesse optical cavities are exploited to elongate the effective optical absorption path [67]. However, this method requires almost perfectly reflecting mirrors ($R > 99.99$) and a light source with long coherence length to attain a very long absorption path. Such systems employ lasers as the light source and are not suitable for wafer-level miniaturization. By using highly reflective mirrors ($R \sim 98$) on the other hand, the requirements on the light source can be moderated, while still achieving a moderately long optical absorption path. Therefore, the combination of a low-cost IR emitter with a gas-filled LVOF, where the filter cavity is used as a gas cell is highly suitable for wafer-level microspectroscopy. In the remainder of this thesis, the functional integration of an LVOF and a gas cell is pursued.

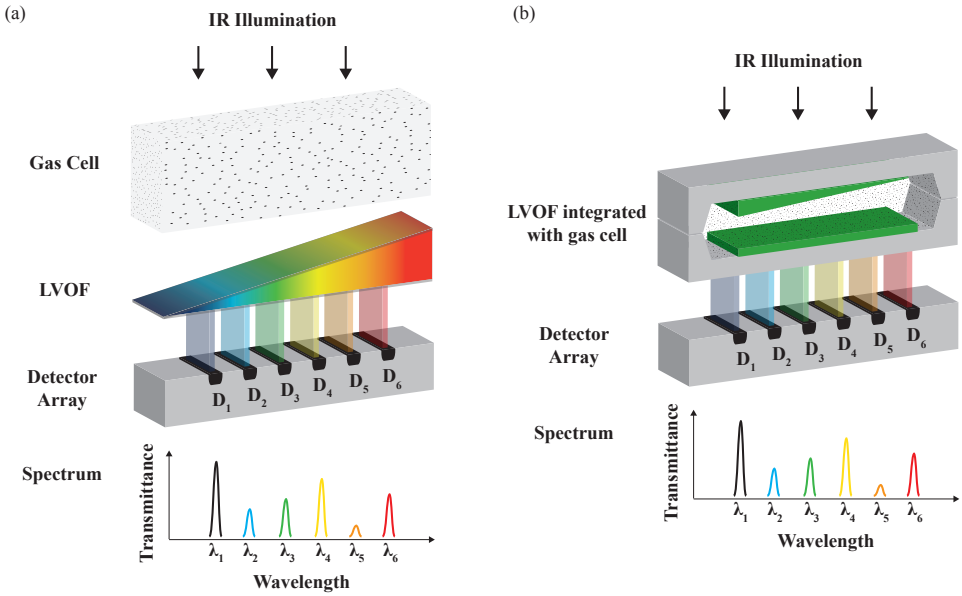

Figure 2.16: The components of an optical absorption based spectrometer with (a) a standard LVOF combined with a separate gas cell and (b) a miniaturized gas cell integrated with the resonator cavity of an LVOF.

REFERENCES

[1] L. J. Radziemski, R. W. Solarz, and J. A. Paisner, *Laser Spectroscopy and Its Applications* (Marcel Dekker, 1987).

[2] P. Kluczynski, J. Gustafsson, Å. M. Lindberg, and O. Axner, *Wavelength modulation absorption spectrometry - an extensive scrutiny of the generation of signals,* Spectrochimica Acta Part B: Atomic Spectroscopy **56**, 1277 (2001).

[3] G. C. Bjorklund, M. D. Levenson, W. Lenth, and C. Ortiz, *Frequency modulation (FM) spectroscopy,* Applied Physics B **32**, 145 (1983).

[4] J. U. White, *Long optical paths of large aperture,* Journal of the Optical Society of America **32**, 285 (1942).

[5] D. R. Herriott and H. J. Schulte, *Folded optical delay lines,* Applied Optics **4**, 883 (1965).

[6] M. L. Thoma, R. Kaschow, and F. J. Hindelang, *A multiple-reflection cell suited for absorption measurements in shock tubes,* Shock Waves **4**, 51 (1994).

[7] M. Mangold, B. Tuzson, M. Hundt, J. Jágerská, H. Looser, and L. Emmenegger, *Circular paraboloid reflection cell for laser spectroscopic trace gas analysis,* Journal of the Optical Society of America A **33**, 913 (2016).

[8] J. J. Scherer, J. B. Paul, A. O'Keefe, and R. J. Saykally, *Cavity ringdown laser absorption spectroscopy: History, development, and application to pulsed molecular beams,* Chemical Reviews **97**, 25 (1997).

[9] J. A. Giordmaine and R. C. Miller, *Tunable coherent parametric oscillation in $LiNbO_3$ at optical frequencies,* Physical Review Letters **14**, 973 (1965).

[10] D. D. Arslanov, M. Spunei, J. Mandon, S. M. Cristescu, S. T. Persijn, and F. J. M. Harren, *Continuous-wave optical parametric oscillator based infrared spectroscopy for sensitive molecular gas sensing,* Laser & Photonics Reviews **7**, 188 (2013).

[11] Y. Yao, A. J. Hoffman, and C. F. Gmachl, *Mid-infrared quantum cascade lasers,* Nature Photonics **6**, 432 (2012).

[12] S. D. Jackson, *Towards high-power mid-infrared emission from a fibre laser,* Nature Photonics **6**, 423 (2012).

[13] J.-C. Gauthier, V. Fortin, J.-Y. Carrée, S. Poulain, M. Poulain, R. Vallée, and M. Bernier, *Mid-IR supercontinuum from 2.4 to 5.4 µm in a low-loss fluoroindate fiber,* Optics Letters **41**, 1756 (2016).

[14] S. B. Mirov, V. V. Fedorov, D. Martyshkin, I. S. Moskalev, M. Mirov, and S. Vasilyev, *Progress in mid-IR lasers based on Cr and Fe-doped II-VI chalcogenides,* IEEE Journal of Selected Topics in Quantum Electronics **21**, 292 (2015).

[15] E. G. Loewen and E. Popov, *Diffraction Gratings and Applications* (CRC Press, 1997).

[16] J. Meaburn, *Detection and Spectrometry of Faint Light*, Vol. 56 (Springer Science & Business Media, 2012).

[17] W. G. Fastie, *A small plane grating monochromator,* Journal of the Optical Society of America **42**, 641 (1952).

[18] R. C. Lord and T. K. McCubbin, *Infrared spectroscopy from 5 to 200 microns with a small grating spectrometer*,* Journal of the Optical Society of America **47**, 689 (1957).

[19] S. Grabarnik, R. Wolffenbuttel, A. Emadi, M. Loktev, E. Sokolova, and G. Vdovin, *Planar double-grating microspectrometer,* Optics Express **15**, 3581 (2007).

[20] S. Grabarnik, A. Emadi, H. Wu, G. de Graaf, and R. F. Wolffenbuttel, *High-resolution microspectrometer with an aberration-correcting planar grating,* Applied Optics **47**, 6442 (2008).

[21] Q. Nie, Z. Wen, and J. Huang, *A high-performance scanning grating based on tilted (111) silicon wafer for near infrared micro spectrometer application,* Microsystem Technologies **21**, 1749 (2014).

[22] Q. Zhou, J. Pang, X. Li, K. Ni, and R. Tian, *Concave grating miniature spectrometer with an expanded spectral band by using two entrance slits,* Chinese Optics Letters **13**, 110501 (2015).

[23] F. Zheng, L. Liu, G. Zhang, K. Huan, Y. Li, and X. Shi, *Compact spectrometer based on concave grating,* in *SPIE Proceedings*, Vol. 9795 (2015) pp. 97951C–97951C–4.

[24] S. H. Kong, D. D. L. Wijngaards, and R. F. Wolffenbuttel, *Infrared micro-spectrometer based on a diffraction grating,* Sensors and Actuators A: Physical **92**, 88 (2001).

[25] R. Bell, *Introductory Fourier Transform Spectroscopy* (Elsevier, 2012).

[26] P. Fellgett, *I. - les principes généraux des méthodes nouvelles en spectroscopie interférentielle - a propos de la théorie du spectrométre interférentiel multiplex,* J. Phys. Radium **19**, 187 (1958).

[27] P. Jacquinot, C. Dufour, and J. Rech, *Optical conditions in the use of photo-electric cells in spectrographs and interferometers,* do CNRS **6**, 91 (1948).

[28] J. R. Connes, *Recherches sur la spectroscopie par transformations de Fourier* (Éd. de la" Revue d'optique théorique et instrumentale, 1961).

[29] A. Michelson, *The relative motion of the earth and the luminiferous ether,* American Journal of Science **22**, 120–129 (1881).

[30] O. Manzardo, Y. Petremand, H. P. Herzig, W. Noell, and N. De Rooij, *Micro-sized Fourier spectrometer,* in *Diffractive Optics and Micro-Optics*, OSA Trends in Optics and Photonics Series, Vol. 75 (Optical Society of America, 2002) p. DTuC5.

[31] M. Kraft, A. Kenda, T. Sandner, and H. Schenk, *MEMS-based compact FT-spectrometers - a platform for spectroscopic mid-infrared sensors,* in *IEEE Sensors* (2008) pp. 130–133.

[32] A. Kenda, M. Kraft, A. Tortschanoff, W. Scherf, T. Sandner, H. Schenk, S. Lüttjohann, and A. Simon, *Development, characterization and application of compact spectrometers based on MEMS with in-plane capacitive drives,* in *SPIE Proceedings*, Vol. 9101 (2014) pp. 910102–910102–10.

[33] Y. M. Sabry, D. Khalil, and T. Bourouina, *Monolithic silicon-micromachined free-space optical interferometers onchip,* Laser & Photonics Reviews **9**, 1 (2015).

[34] E. R. Deutsch, D. Reyes, E. R. Schildkraut, and J. Kim, *High-resolution miniature FTIR spectrometer enabled by a large linear travel MEMS pop-up mirror,* in *SPIE Proceedings*, Vol. 7319 (2009) pp. 73190J–73190J–8.

[35] O. Manzardo, R. Michaely, F. Schädelin, W. Noell, T. Overstolz, N. De Rooij, and H. P. Herzig, *Miniature lamellar grating interferometer based on silicon technology,* Optics Letters **29**, 1437 (2004).

[36] H. R. Seren, S. Holmstrom, N. P. Ayerden, J. Sharma, and H. Urey, *Lamellar-grating-based MEMS Fourier transform spectrometer,* Journal of Microelectromechanical Systems **21**, 331 (2012).

[37] N. P. Ayerden, U. Aygun, S. T. S. Holmstrom, S. Olcer, B. Can, J.-L. Stehle, and H. Urey, *High-speed broadband FTIR system using MEMS,* Applied Optics **53**, 7267 (2014).

[38] J. P. Coates, *New microspectrometers: Building on the principle that simple is beautiful,* Spectroscopy **15**, 21 (2000).

[39] J. H. Correia, G. de Graaf, S. H. Kong, M. Bartek, and R. F. Wolffenbuttel, *Single-chip CMOS optical microspectrometer,* Sensors and Actuators A: Physical **82**, 191 (2000).

[40] G. Minas, J. C. Ribeiro, J. S. Martins, R. F. Wolffenbuttel, and J. H. Correia, *An array of Fabry-Perot optical-channels for biological fluids analysis,* Sensors and Actuators A: Physical **115**, 362 (2004).

[41] S. Feng, X. Zhang, and P. J. Klar, *Waveguide Fabry-Perot microcavity arrays,* Applied Physics Letters **99**, 053119 (2011).

[42] A. T. T. D. Tran, Y. H. Lo, Z. H. Zhu, D. Haronian, and E. Mozdy, *Surface micromachined Fabry-Perot tunable filter,* IEEE Photonics Technology Letters **8**, 393 (1996).

[43] J. H. Correia, M. Bartek, and R. F. Wolffenbuttel, *Bulk-micromachined tunable Fabry–Perot microinterferometer for the visible spectral range,* Sensors and Actuators A: Physical **76**, 191 (1999).

[44] C. A. Barrios, V. R. Almeida, R. R. Panepucci, B. S. Schmidt, and M. Lipson, *Compact silicon tunable Fabry-Perot resonator with low power consumption,* IEEE Photonics Technology Letters **16**, 506 (2004).

[45] J. S. Milne, J. M. Dell, A. J. Keating, and L. Faraone, *Widely tunable MEMS-based Fabry-Perot filter,* Journal of Microelectromechanical Systems **18**, 905 (2009).

[46] D. K. Tripathi, F. Jiang, R. Rafiei, K. K. M. B. D. Silva, J. Antoszewski, M. Martyniuk, J. M. Dell, and L. Faraone, *Suspended large-area MEMS-based optical filters for multispectral shortwave infrared imaging applications,* Journal of Microelectromechanical Systems **24**, 1102 (2015).

[47] A. Emadi, H. Wu, G. de Graaf, and R. Wolffenbuttel, *Design and implementation of a sub-nm resolution microspectrometer based on a linear-variable optical filter,* Optics Express **20**, 489 (2012).

[48] A. Emadi, H. Wu, S. Grabarnik, G. De Graaf, K. Hedsten, P. Enoksson, J. H. Correia, and R. F. Wolffenbuttel, *Fabrication and characterization of IC-compatible linear variable optical filters with application in a micro-spectrometer,* Sensors and Actuators A: Physical **162**, 400 (2010).

[49] N. P. Ayerden, M. Ghaderi, M. F. Silva, A. Emadi, P. Enoksson, J. H. Correia, G. de Graaf, and R. F. Wolffenbuttel, *Design, fabrication and characterization of LVOF-based IR microspectrometers,* in *SPIE Proceedings*, Vol. 9130 (2014) pp. 91300T–91300T–10.

[50] B. Sheng, P. Chen, C. Tao, R. Hong, Y. Huang, and D. Zhang, *Linear variable filters fabricated by ion beam etching with triangle-shaped mask and normal film coating technique,* Chinese Optics Letters **13**, 122301 (2015).

[51] J. Antila, A. Miranto, J. Mäkynen, M. Laamanen, A. Rissanen, M. Blomberg, H. Saari, and J. Malinen, *MEMS and piezo actuator-based Fabry-Perot interferometer technologies and applications at VTT,* in *SPIE Proceedings* (2010) pp. 76800U–76800U.

[52] R. Mannila, M. Tuohiniemi, J. Mäkynen, I. Näkki, and J. Antila, *Hydrocarbon gas detection with microelectromechanical Fabry-Perot interferometer,* in *SPIE Proceedings* (2013) pp. 872608–872608–9.

[53] R. Rubio, J. Santander, J. Fonollosa, L. Fonseca, I. Gràcia, C. Cané, M. Moreno, and S. Marco, *Exploration of the metrological performance of a gas detector based on an array of unspecific infrared filters,* Sensors and Actuators B: Chemical **116**, 183 (2006).

[54] L. Fonseca, R. Rubio, J. Santander, C. Calaza, N. Sabaté, P. Ivanov, E. Figueras, I. Gràcia, C. Cané, S. Udina, M. Moreno, and S. Marco, *Qualitative and quantitative substance discrimination using a CMOS compatible non-specific NDIR microarray,* Sensors and Actuators B: Chemical **141**, 396 (2009).

[55] N. Neumann, M. Ebermann, S. Kurth, and K. Hiller, *Tunable infrared detector with integrated micromachined Fabry-Perot filter,* Journal of Micro/Nanolithography, MEMS, and MOEMS **7**, 021004 (2008), 10.1117/1.2909206.

[56] C. A. Musca, J. Antoszewski, K. J. Winchester, A. J. Keating, T. Nguyen, K. K. M. Silva, J. M. Dell, L. Faraone, P. Mitra, J. D. Beck, M. R. Skokan, and J. E. Robinson, *Monolithic integration of an infrared photon detector with a MEMS-based tunable filter,* IEEE Electron Device Letters **26**, 888 (2005).

[57] A. J. Keating, J. Antoszewski, K. K. M. B. D. Silva, K. J. Winchester, T. Nguyen, J. M. Dell, C. A. Musca, L. Faraone, and O. Samardzic, *Fabry-Perot MEMS microspectrometers spanning the SWIR and MWIR,* in *SPIE Proceedings* (2007) pp. 65423G–65423G.

[58] H. Wu, A. Emadi, P. M. Sarro, G. d. Graaf, and R. F. Wolffenbuttel, *A surface micromachined thermopile detector array with an interference-based absorber,* Journal of Micromechanics and Microengineering **21**, 074009 (2011).

[59] C. Strandman, L. Rosengren, H. G. A. Elderstig, and Y. Backlund, *Fabrication of 45 degree mirrors together with well-defined v-grooves using wet anisotropic etching of silicon,* Journal of Microelectromechanical Systems **4**, 213 (1995).

[60] R. Drago, V. Danilo, A. Uros, M. Matej, and A. Slavko, *The role of Triton surfactant in anisotropic etching of 100 reflective planes on (100) silicon,* Journal of Micromechanics and Microengineering **15**, 1174 (2005).

[61] V. Mattias and B. Ylva, *Precise mask alignment to the crystallographic orientation of silicon wafers using wet anisotropic etching,* Journal of Micromechanics and Microengineering **6**, 279 (1996).

[62] H. Jun Hyun, R. Shankar, and L. Chung-Hoon, *A novel batch-processing method for accurate crystallographic axis alignment,* Journal of Micromechanics and Microengineering **23**, 055017 (2013).

[63] S. S. Singh, S. Veerla, V. Sharma, A. K. Pandey, and P. Pal, *Precise identification of <100> directions on si 001 wafer using a novel self-aligning pre-etched technique,* Journal of Micromechanics and Microengineering **26**, 025012 (2016).

[64] K. Rola, K. Ptasinski, A. Zakrzewski, and I. Zubel, *Characterization of 45 degrees micromirrors fabricated by silicon anisotropic etching in solutions containing different organic additives,* Procedia Engineering **47**, 510 (2012).

[65] D. W. de Lima Monteiro, O. Akhzar-Mehr, P. M. Sarro, and G. Vdovin, *Single-mask microfabrication of aspherical optics using KOH anisotropic etching of Si,* Optics Express **11**, 2244 (2003).

[66] D. L. Kendall, T. G. Digges Iii, W. P. Eaton, and R. P. Manginell, *Micromirror arrays using KOH:H_2O micromachining of silicon for lens templates, geodesic lenses, and other applications,* Optical Engineering **33**, 3578 (1994), 10.1117/12.179881.

[67] G. Gagliardi and H.-P. Loock, *Cavity-Enhanced Spectroscopy and Sensing* (Springer, 2014).

3

LVOF Design Approach

INTERFERENCE filters are wavelength selective devices that are highly suitable for the development of low-cost microspectrometers. The operating principle is based on the constructive interference of the light beam that is reflected multiple times between two reflectors. Although there is no consensus on the terminology, an interference filter is commonly denoted as an etalon if it is composed of a transparent plate with two reflecting surfaces or as a Fabry-Perot (FP) interferometer if the resonator is trapped between two highly reflective parallel mirrors. In this thesis, the terms FP filter and FP interferometer are used interchangeably to refer to an interference filter that is composed of two parallel mirrors with a resonator layer in-between.

The optical path difference between successively reflected beams must match the constructive interference condition to ensure filter operation. Since the thickness of the resonator layer is directly proportional to the optical path difference, it determines the wavelength to be transmitted through the filter [1]. High-resolution analysis in a wide wavelength range is crucial for spectroscopic applications. The wideband operation of these filters is achieved either by creating an array of FP filters with different resonator thicknesses [2–4], or by tuning the position of one of the mirrors to dynamically adjust the resonator layer thickness, i.e tunable FP filter [5–8]. In both configurations, the mirror parallelism is required for high-resolution measurements. In an array of fixed filters, high-parallelism can be achieved by a fine-tuned fabrication process, while the number of spectral channels; hence, the spectral resolving power of the spectrometer is limited by the number of filters. In tunable FP filters, continuous mechanical movement of one of the mirrors allows for more spectral channels, thereby increasing the spectral resolving power, whereas mirror parallelism and robustness become issues.

A linear variable optical filter (LVOF) is a wideband interferometer without any moving parts; thus, combining the high spectral resolving power of a tunable FP filter with the robustness of an array of fixed FP filters. An LVOF is composed of two mirrors; one flat and one slightly tilted, with a tapered resonator layer in-between. Therefore, the LVOF in principle represents a continuous array of infinitely many different FP filters. By combining the LVOF with an array of detectors, a wideband spectral response can be measured [9–11].

The increasing demand for microspectrometers has triggered the miniaturization of all the components in a spectrometer in addition to the monolithic integration of these components. In this thesis, the functional integration of a sample gas cell and an LVOF is investigated. To achieve that, the tapered resonator cavity of an LVOF serves as a gas cell besides wavelength selection. This requires highly reflective mirrors and a long resonator cavity to start with, which are demanding operating conditions for an LVOF.

The analysis of LVOFs reported in literature is based on dividing the filter in discrete FP structures. By using the FP description, perfectly parallel mirrors are assumed and

the tilt between the LVOF mirrors is implemented as a stepwise incremental resonator width between neighboring structures. In this chapter, a theoretical framework including both FP and LVOF structures is developed. The LVOF is described in terms of the Fizeau interferometer, which is a wedged FP filter. It is shown that the FP approach must be abandoned for designing an LVOF that should satisfy demanding operating conditions, as required in this application. Also, optical constraints on filter performance are explored and optimization methods to improve the spectral performance are provided.

3.1. APPROXIMATION AS AN ARRAY OF FABRY-PEROT FILTERS

Optical filters are conventionally designed using optical coating design software, such as The Essential Macleod or TFCalc. In these tools, an optical layer is defined by the material type and the thickness. The spectral response of a coating can be simulated by stacking thin-film layers and selecting the incident and the emergent medium as shown in Fig. 3.1.

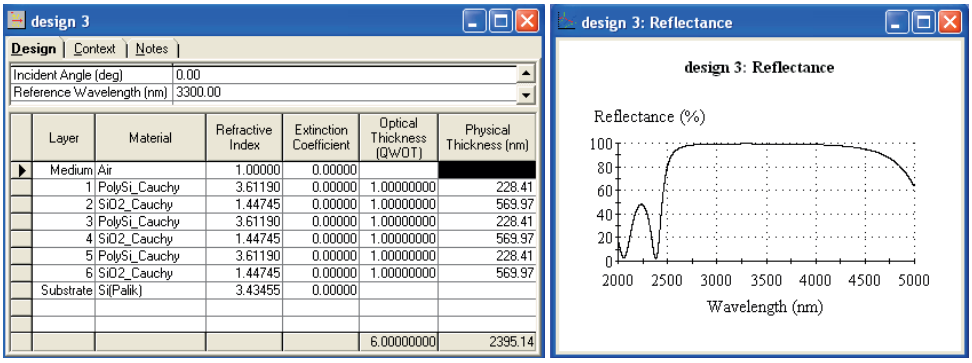

Figure 3.1: An example of coating design file and reflectance spectrum extracted from 'The Essential Macleod'.

A material in these tools is represented by the complex refractive index ($\tilde{n} = n - ik$), where the refractive index (n) and the extinction coefficient (k) are defined in terms of wavelength. The refractive index is a unitless number and is equal to the ratio of the speed of light in free space to that in the medium. Similar to the refractive index, the extinction coefficient is a unitless number and is related to the absorption coefficient (γ, usually in cm^{-1}) by $\gamma = 4\pi k/\lambda$ where λ is the wavelength. The material library includes commonly used thin-film materials; however, material data from external libraries or data that is extracted from ellipsometry measurements can be imported as custom materials in these software.

The thickness of a thin-film layer is defined either as physical or optical. The physical thickness is the actual thickness of the film represented usually in nanometers. In the

interference calculations of a coating, the most important quantity related to a thin-film layer is its effect on the phase of the light. The phase change during propagation depends on the wavelength of the light and the optical path, where the latter is the multiplication of the physical layer thickness and the refractive index of the layer material. Therefore, it is more common to denote layer thickness in terms of the optical path as either full-wave optical thickness (FWOT) or quarter-wave optical thickness (QWOT). In FWOT, the optical path is equal to the reference design wavelength, whereas in QWOT the optical path is equal to one quarter of the reference wavelength.

The optical coating design software is a very practical tool to design Bragg reflectors and FP filters, which are composed of multiple layers of thin-films. The transmittance and reflectance spectra of these devices can be easily calculated for different optical parameters; such as incidence angle, cone angle and polarization of the light source. In all these simulations, the thin-film layers are assumed to be smooth, flat and parallel.

An LVOF is usually simulated as an array of discrete FP filters with increasing resonator thickness $(h_1, h_2, ..., h_N)$ as the filter is scanned along its length away from the wedge apex (Fig. 3.2). However, mirror nonparallelism is inherent to the operating principle of an LVOF, where one of the mirrors is intentionally tilted.

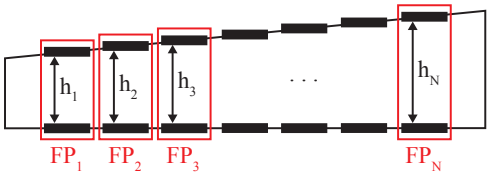

Figure 3.2: LVOF approximated as an array of FP filters.

Due to the nonparallelism of the mirrors, the spectral response of an LVOF diverges from an FP filter, which becomes particularly noticeable when the reflectivity of the mirrors approaches to ideal. Highly reflective mirrors are required to be able to use the resonator cavity of an LVOF also as a gas cell. Therefore, it is crucial to study the difference between an FP filter and an LVOF to develop a mathematical framework for the optical design of our devices.

3.2. THEORETICAL BACKGROUND

The interference filters are composed of two mirrors with a resonator layer in-between. The optical path between the mirrors, or equivalently the thickness of the resonator layer, determines the wavelength to be transmitted. The interference theory is based on calculating the phase difference associated with multiple reflections in the resonator and subsequently summing these waves to simulate the overall effect on the transmis-

sion or reflection. In an FP filter, the mirrors are perfectly parallel and the resonator layer between these mirrors has a fixed thickness. An LVOF on the other hand is composed of one flat and one tilted mirror with a tapered resonator in-between. Therefore, an LVOF resembles to a wedged interferometer, i.e. Fizeau interferometer, rather than an array of FP filters. In the following sections, the theoretical background of FP and Fizeau interferometers will be investigated to build a mathematical framework for the LVOF design at demanding operating conditions.

3.2.1. FABRY-PEROT INTERFEROMETER

The theoretical background of an FP interferometer was explained in detail by Born and Wolf [12]. Assume that a collimated monochromatic light beam is impinging on an FP interferometer with refractive index n' and resonator thickness h at an incidence angle of θ as shown in Fig. 3.3.

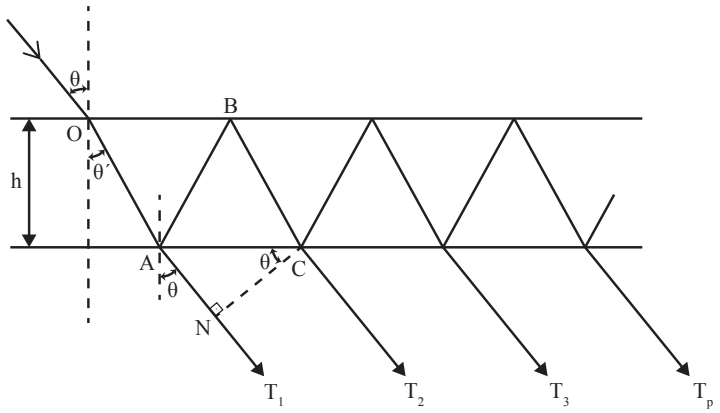

Figure 3.3: Fabry-Perot interferometer.

The light beam hits the second flat of the interferometer at an incidence angle of θ' and the refractive index of the surrounding medium is n. Then the optical path difference between the first and the pth wave that is transmitted through the filter is

$$\Delta S_p = \left(n'\left(AB+BC\right) - nAN\right)\left(p-1\right), \tag{3.1}$$

where $n'\left(AB+BC\right) - nAN$ is the optical path difference between two consecutively transmitted waves such as T_1 and T_2 or T_{p-1} and T_p. Using trigonometry, physical values AB, BC and AN can be defined in terms of the resonator thickness and the incidence angle.

$$AB = BC = \frac{h}{\cos\theta'} \tag{3.2}$$

$$AN = AC\sin\theta = 2h\tan\theta'\sin\theta \tag{3.3}$$

By applying Snell's Law ($n\sin\theta = n'\sin\theta'$) to the equations above, the optical path difference can be calculated as in Eq. 3.4. The phase change related to the reflection from the mirrors is neglected. This could be an issue in metal-based mirrors; however, can be disregarded in dielectric mirrors [13].

$$\Delta S_p = \left(\frac{2n'h}{\cos\theta'} - \frac{2nh\sin\theta'\sin\theta}{\cos\theta'}\right)(p-1) = \left(2n'h\cos\theta'\right)(p-1) \tag{3.4}$$

Hence, the phase difference between the first and the pth wave that is transmitted through the filter is given by Eq. 3.5 where λ_0 is the wavelength of the light source.

$$\delta_p = \frac{2\pi}{\lambda_0}\Delta S_p = \frac{4\pi}{\lambda_0}n'h\cos\theta'\left(p-1\right) \tag{3.5}$$

3.2.2. FIZEAU INTERFEROMETER

A Fizeau interferometer can be described as a wedged FP interferometer, where one of the mirrors is slightly tilted to create fringes of equal thickness when illuminated with monochromatic light. Such interferometers are used for measuring optical flatness with high accuracy [14]. An LVOF can therefore be defined as a Fizeau interferometer illuminated with a broadband light source for spectroscopic purposes.

The multiple beam interference of Fizeau wedges was theoretically studied by Brossel [15]. Based on this theory, the shape and the location of multiple beam fringes were later calculated thanks to the advances in computation [16, 17]. The wedge material is assumed to have a refractive index n' surrounded with a medium of refractive index n. Two mirror surfaces on each side of the wedge are inclined at an angle α. The device is illuminated with a plane wave of monochromatic light, whose wave-fronts are passing through the wedge apex. The angle of incidence θ', is defined as positive if the light impinges on the flat surface from the side of the normal nearest the wedge apex and negative otherwise. The phase change associated with the reflection from the mirrors is neglected.

POSITIVE INCIDENCE

After multiple reflections in the wedge, the light moves away from the wedge apex if the incidence angle is positive. At the pth reflection from the flat surface, the angle between the beam and the normal is $\theta' + 2\left(p-1\right)\alpha$ as shown in Fig. 3.4.

The exit angle from the wedge for all transmitted waves can be defined using Snell's

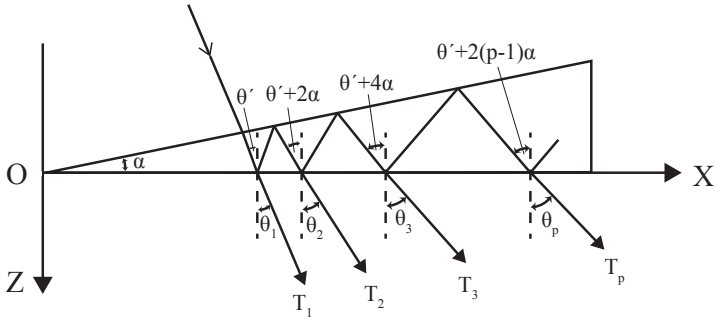

Figure 3.4: Multiple reflections in Fizeau interferometer at a positive incidence angle.

Law.

$$\begin{aligned} n\sin\theta_1 &= n'\sin\theta' \\ n\sin\theta_2 &= n'\sin\left(\theta'+2\alpha\right) \\ &\vdots \\ n\sin\theta_p &= n'\sin\left(\theta'+2\left(p-1\right)\alpha\right) \end{aligned} \tag{3.6}$$

Multiple reflections inside the wedge give rise to a set of plane waves with wavefronts $W_1, W_2, ..., W_p$, which interfere at point $P(x,z)$ as shown in Fig. 3.5.

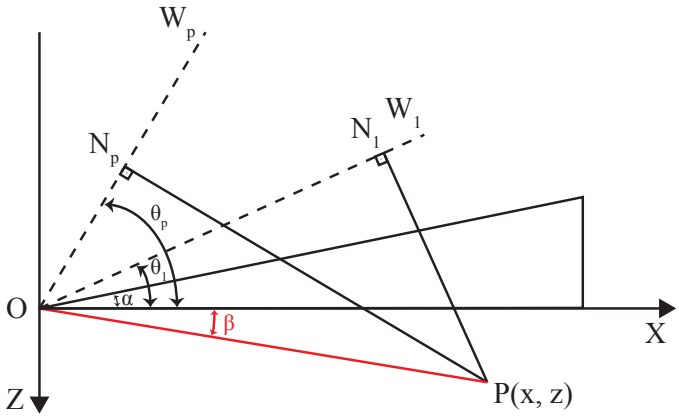

Figure 3.5: Optical path difference after multiple reflections in Fizeau interferometer at a positive incidence angle.

The optical path difference between the first and the pth transmitted wave can be calculated as,

$$\Delta S_p = n\left(PN_p - PN_1\right). \tag{3.7}$$

Assuming that OP makes an angle of β with the x-axis, the difference of PN_p and

PN_1 can be represented in terms of OP, β and the exit angles using trigonometry.

$$PN_p = OP\left(\sin\left(\theta_p + \beta\right)\right) = OP\left(\sin\theta_p \cos\beta + \sin\beta\cos\theta_p\right) \tag{3.8}$$

$$PN_1 = OP\left(\sin\left(\theta_1 + \beta\right)\right) = OP\left(\sin\theta_1 \cos\beta + \sin\beta\cos\theta_1\right) \tag{3.9}$$

$$PN_p - PN_1 = OP\left[\cos\beta\left(\sin\theta_p - \sin\theta_1\right) + \sin\beta\left(\cos\theta_p - \cos\theta_1\right)\right] \tag{3.10}$$

Since, $OP\cos\beta = x$ and $OP\sin\beta = z$,

$$\Delta S_p = nx\left(\sin\theta_p - \sin\theta_1\right) + nz\left(\cos\theta_p - \cos\theta_1\right). \tag{3.11}$$

Combining Eq. 3.6 and Eq. 3.11, one can define the optical path difference in terms of θ', α, and p. If the resonator layer and the surrounding medium are both air ($n = n' = 1$) as in our case, the optical path difference can be simplified as in Eq. 3.12.

$$\Delta S_p = x\left[\sin\left(\theta' + 2\left(p-1\right)\alpha\right) - \sin\theta'\right] + z\left[\cos\left(\theta' + 2\left(p-1\right)\alpha\right) - \cos\theta'\right] \tag{3.12}$$

NEGATIVE INCIDENCE

If the light beam approaches the flat surface of the wedge from the side of the normal away from the wedge apex, the incidence angle is negative. In this case, the light spot moves toward the apex after multiple reflections in the wedge. At the pth reflection from the flat surface, the angle between the beam and the normal becomes $\varphi' - 2\left(p-1\right)\alpha$ assuming an incidence angle of φ', as shown in Fig. 3.6. As in the positive incidence

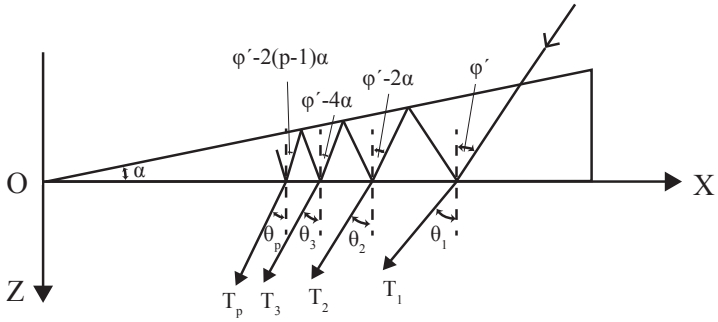

Figure 3.6: Multiple reflections in Fizeau interferometer at a negative incidence angle.

case, multiple reflections inside the wedge result in a set of plane waves with wavefronts $W_1, W_2, ..., W_p$, which interfere at point P(x,z) as shown in Fig. 3.7. The optical path difference between the first and the pth transmitted wave can be calculated as,

$$\Delta S_p = n\left(PN_p - PN_1\right). \tag{3.13}$$

Using trigonometry PN_1 and PN_p can be represented in terms of x, z and the exit angles.

$$PN_p = PB\cos\theta_p = (z - AB)\cos\theta_p = (z - x\tan\theta_p)\cos\theta_p = z\cos\theta_p - x\sin\theta_p \tag{3.14}$$

$$PN_1 = PC\cos\theta_1 = (z - AC)\cos\theta_1 = (z - x\tan\theta_1)\cos\theta_1 = z\cos\theta_1 - x\sin\theta_1 \tag{3.15}$$

Therefore the optical path difference is

$$\Delta S_p = nx(\sin\theta_1 - \sin\theta_p) + nz(\cos\theta_p - \cos\theta_1). \tag{3.16}$$

Assuming unity refractive index for both the resonator and the surrounding medium, the optical path difference can further be simplified as in Eq. 3.17.

$$\Delta S_p = x[\sin\varphi' - \sin(\varphi' - 2(p-1)\alpha)] + z[\cos(\varphi' - 2(p-1)\alpha) - \cos\varphi'] \tag{3.17}$$

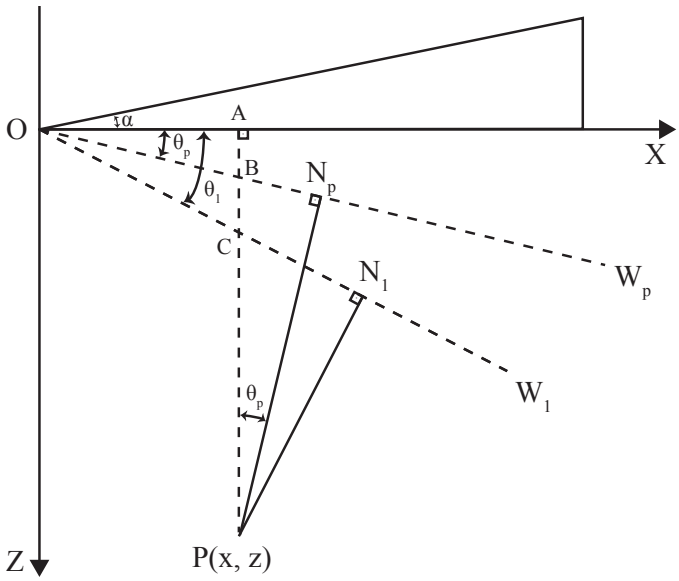

Figure 3.7: Optical path difference after multiple reflections in Fizeau interferometer at a negative incidence angle.

Using $\varphi' = -\theta'$ as the negative incidence angle, the optical path difference can be translated into Eq. 3.18.

$$\Delta S_p = x[\sin(-\theta') - \sin(-\theta' - 2(p-1)\alpha)] + z[\cos(-\theta' - 2(p-1)\alpha) - \cos(-\theta')] \tag{3.18}$$

Using trigonometric equalities $\sin(-\theta) = -\sin\theta$ and $\cos(-\theta) = \cos\theta$ to convert Eq. 3.18 to Eq. 3.19, one can see that the optical path difference for negative incidence angle is the same as the optical path difference for positive incidence.

$$\Delta S_p = x\left[-\sin\theta' + \sin\left(\theta' + 2\left(p-1\right)\alpha\right)\right] + z\left[\cos\left(\theta' + 2\left(p-1\right)\alpha\right) - \cos\theta'\right] \tag{3.19}$$

Then, the phase difference for both positive and negative incidence is given as follows:

$$\begin{aligned}\delta_p &= \frac{2\pi}{\lambda_0}\Delta S_p \\ &= \frac{2\pi}{\lambda_0}\left(x\left[\sin\left(\theta' + 2\left(p-1\right)\alpha\right) - \sin\theta'\right] + z\left[cos\left(\theta' + 2\left(p-1\right)\alpha\right) - \cos\theta'\right]\right).\end{aligned} \tag{3.20}$$

Therefore, the phase difference between the pth and the directly transmitted waves can be calculated using Eq. 3.5 and Eq. 3.20 for FP and Fizeau interferometers respectively.

3.2.3. FILTER TRANSMISSION

The complex amplitudes of the waves transmitted through the filter can be calculated using the transmission and reflection coefficients of the mirrors around the resonator. Let r be the reflection coefficient (ratio of reflected and incident amplitudes) and t the transmission coefficient (ratio of transmitted and incident amplitudes) for a wave traveling from the surrounding medium into the resonator. For a wave traveling from the resonator to the surrounding medium r' and t' are the reflection and transmission coefficients, respectively. If $A^{(i)}$ is the amplitude of the light source, then the complex amplitudes of the waves transmitted through the filter are:

$$\underbrace{tt'A^{(i)}e^{i\delta_1}}_{T_1}, \underbrace{tt'r'^2A^{(i)}e^{i\delta_2}}_{T_2}, \underbrace{tt'r'^4A^{(i)}e^{i\delta_3}}_{T_3}, ..., \underbrace{tt'r'^{2(p-1)}A^{(i)}e^{i\delta_p}}_{T_p}. \tag{3.21}$$

Then, the amplitude of infinitely many transmitted waves interfering at point P($A^{(t)}$) can be defined as in Eq. 3.22, given that R and T are the reflectivity and the transmissivity of the mirrors respectively.

$$A^{(t)} = A^{(i)}tt'\sum_{p=1}^{\infty} r'^{2(p-1)}e^{i\delta_p} = A^{(i)}T\sum_{p=1}^{\infty} R^{(p-1)}e^{i\delta_p} \tag{3.22}$$

The intensity is calculated by taking the square of the transmitted wave amplitude as

in Eq. 3.23.

$$I^{(t)} = \left(A^{(i)}\right)^2 T^2 \left| \sum_{p=1}^{\infty} R^{(p-1)} e^{i\delta_p} \right|^2 \tag{3.23}$$

The spectral response of an FP interferometer can be simulated by sweeping the wavelength for a given cavity length using Eq. 3.5 and Eq. 3.23. To calculate the transmittance of a Fizeau interferometer, the x-position on the slope of the LVOF (i.e. the cavity length at that position) must be swept for a particular wavelength using Eq. 3.20 and Eq. 3.23.

3.3. OPTICAL CONSTRAINTS ON FILTER PERFORMANCE

Using the resonator cavity of an LVOF also as a gas cell requires the elongation of a µm-level physical cavity to a mm-level effective optical path length. To achieve such an elongation using multiple reflections, a relatively long µm-level physical cavity ($h \approx 25$µm) must be combined with highly reflective mirrors ($R \geq 95\%$). These demanding operating conditions affect the transmission of an LVOF considerably, due to the nonparallel configuration of the mirrors. Moreover, since the light beam is incident on a sloped mirror surface, normal incidence does not necessarily provide an optimum result. It is shown that the angle of incidence can be optimized at a given filter-detector separation. In addition, the collimation of the light beam has a strong effect on the transmission of an optical filter. Therefore, all these factors should be taken into account to assess and optimize the performance of an LVOF and are discussed in the next subsections.

3.3.1. THE EFFECT OF OPERATING ORDER AND REFLECTIVITY

The operating order is an important parameter in optical filter design and is directly correlated to the resonator layer thickness. The relation between the operating order and the thickness of the resonator layer can be described by the phase difference that is created by multiple reflections of light in an FP filter. When the phase difference between two successive waves becomes equal to 2π, the spectral response of the filter starts repeating itself. For normal incidence ($\theta' = 0°$) and air cavity ($n' = 1$), Eq. 3.5 can be simplified to $\frac{4\pi}{\lambda_0} h = 2\pi m$, where m is the order of interference or the operating order. Hence, the operating order is directly proportional to the resonator thickness for a specific wavelength.

The necessity of a relatively long physical resonator cavity to maximize the effective optical path length forces the filter to operate at a high order ($m > 10$) for a given wavelength range. The transmission of an FP and a Fizeau interferometer for both moderate and high operating orders with various mirror reflectivity values are calculated using the theoretical descriptions given in the previous section. Fig. 3.8 shows the simulation

results at the 3rd and the 15th order. Normal incidence ($\theta' = 0°$) is assumed and interference is observed directly after the interferometer ($z = 0$ mm). For the FP interferometer, a cavity length of respectively 5.085 µm and 25.425 µm is selected. These correspond to the 3rd and the 15th operating orders for a wavelength of 3.39 µm. The 11.4 mm long mirrors of the Fizeau interferometer are inclined at an angle of 15.6 millidegree. The x-position of the Fizeau interferometer is swept in such a way that the 3rd and the 15th operating orders are captured. The wavelength and the x-position values are correlated through the interference equation and Fizeau wedge angle using $x\text{-position} = \frac{m\lambda_0}{2\tan\alpha}$. The transmission curve for the 3390 nm wavelength is located approximately at 18 700 µm and 93 500 µm away from the wedge apex for the 3rd and the 15rd order, respectively, for the device described above.

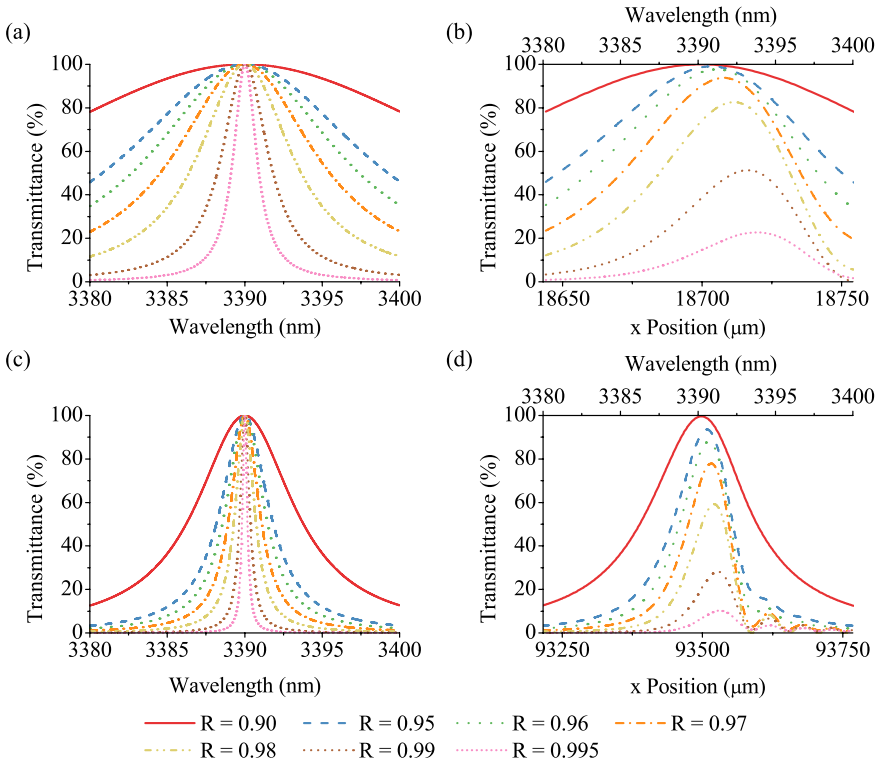

Figure 3.8: Comparison of FP and Fizeau interferometers for various reflectivity values at 3390 nm: (a) 3rd order FP interferometer, (b) 3rd order Fizeau interferometer, (c) 15th order FP interferometer, and (d) 15th order Fizeau interferometer.

The difference in transmission between the FP and the Fizeau representations is evident from the results. The transmittance of an FP interferometer can theoretically reach 100% at any operating order and reflectivity (Fig. 3.8(a) and Fig. 3.8(c)), which is not

the case for the Fizeau interferometer (Fig. 3.8(b) and Fig. 3.8(d)). The resolution of the transmission curves of both FP and Fizeau interferometers improves with increasing order and reflectivity. At 90% reflectivity, the Fizeau interferometer exhibits a similar performance to the FP interferometer. However, at higher reflectivity values the peak transmittance of the Fizeau interferometer deviates substantially. The reduced transmittance, as compared to the FP interferometer, is due to walk-off [18]. Moreover, the transmission curve loses its symmetry and side peaks appear, which are due to the uneven shape of the structure. It should be noted that the reduction of peak transmittance with increased mirror reflectivity is more significant at higher orders of operation.

A multi-pass gas-filled resonance cavity operating at high order of resonance with highly reflective mirrors is required to enable the use of the LVOF cavity as a gas cell. Both the high order of operation and the high reflectance make it necessary to simulate the transmission on the tapered slope in an LVOF by treating it as a Fizeau interferometer, rather than an array of discrete FP filters with parallel mirrors.

3.3.2. THE EFFECT OF INCIDENCE ANGLE AND FILTER-DETECTOR SEPARATION

The sharpness of the fringes in a Fizeau interferometer is highly dependent on the incidence angle of the light. The phase difference between the transmitted waves varies both along the length of the interferometer (x) and toward the detector (z) depending on the incidence angle. This complex relation was previously studied and it was shown that there is an optimum incidence angle for every interferometer-detector separation, at which the peak transmittance is maximized and the best resolution is achieved [19–22].

Multiple reflections between nonparallel mirrors cause the light beam to laterally shift and eventually walk out of the wedge shaped cavity. The nonsymmetrical shape of the transmission curves of a Fizeau interferometer that exhibit lower peak transmittance compared to an equivalent FP filter can be explained by this walk-off. This observation also has significant consequences to any numerical simulations; after a certain number of reflections, the change in the transmission curve becomes negligible and a stable result is obtained. As discussed before, a positive incidence angle, at which the angle of reflection increases at each reflection on the tapered mirror, pushes the multiple-reflected light beam away from the wedge apex. In contrast, in the case of a negative angle of incidence, the angle of reflection decreases at each reflection at the tapered mirror and the multiple-reflected light beam is pushed toward the wedge apex. Hence, applying a positive incidence angle on a Fizeau interferometer is similar to enhancing the effect of walk-off, thereby deteriorating the performance. Therefore, the optimum incidence

angle must be negative to counteract the walk-off effect. However, this does not imply that a more negative angle results in a higher peak transmittance. After a number of reflections, the angle of reflection gets so close to zero (i.e. normal incidence) that the reflected beams start to move away from the wedge apex. When these beams that are reflecting away from the wedge apex cancel the effect of the beams reflecting toward the wedge apex, the transmission curve starts to diverge from the optimum shape again.

The angle of incidence (θ') was defined as the angle of the light impinging on the flat mirror of the wedge. The trajectory of the beam is illustrated in Fig. 3.9 for various incidence angles, assuming 4 reflections from the flat mirror in each case. For both normal and positive incidence, the reflected beam moves away from the wedge apex with normal incidence giving a sharper curve at a slightly higher transmittance. When changing the angle of incidence between the optimum and normal, the beam is firstly reflected toward the wedge apex, until the angle of normal incidence is reached (or surpassed) and then moves away from the wedge apex. The distinction becomes clear at this point; if the beam passes the x-position of the initial beam that enters the wedge, the reflections moving away from the wedge apex cancel the effect of the reflections toward the wedge apex. If the reflected beam does not exceed this point, the system is operated at the optimum angle of incidence. As the incidence angle gets even smaller than the optimum value (i.e. more negative), the beam gets reflected toward the wedge apex; however, its trajectory resembles the mirrored version of the trajectory of a beam at a positive incidence angle with a smaller value.

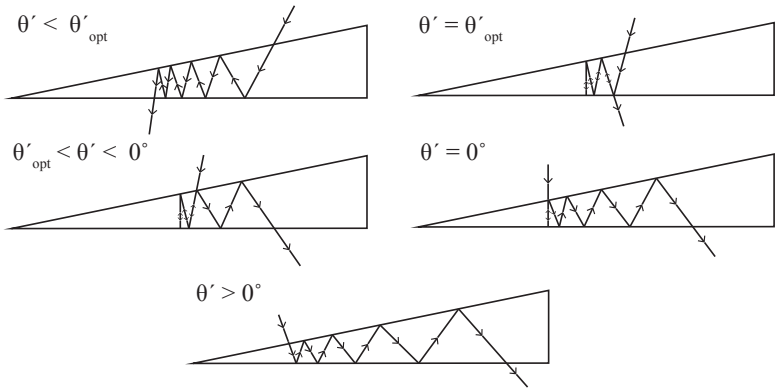

Figure 3.9: The trajectory of a beam in a wedge at different values of the angle of incidence. The light beam gets reflected 4 times off the flat mirror in each case.

The spectral response of a Fizeau interferometer with a slope of a 15.6 millidegree angle between its mirrors is simulated for various incidence angles as shown in Fig. 3.10. The x-position range is selected such that the transmission curve of 3.39 µm wavelength

operating at the 15th order is captured. The interference is observed right after the filter, i.e. $z = 0$ mm and the reflectivity of both mirrors is $R = 0.985$. The optimum incidence angle for this particular case is $-2.2°$ and it can be observed in Fig. 3.10 that any incidence angle other than this value results in wider transmission curves with lower peak transmittance. The curves with incidence angles that are higher than the optimum value lean away from the wedge apex, while the curves with incidence angles that are lower than the optimum value lean toward the wedge apex. This is consistent with the discussion on trajectory, when considering the fact that any incidence angle smaller than the optimum value directs the beam toward the wedge apex. Moreover, incidence angles higher than the optimum value either first sends the beam toward the wedge apex and then away from the wedge apex or directly away from the wedge apex. The transmission curve for the optimum incidence angle acts as a transition point and looks rather symmetric, except for the side peaks. As explained before, a beam with an incidence angle smaller than the optimum value follows a trajectory similar to that of a beam with a positive incidence angle with a smaller value. The transmission curves at an incidence angle of $-5°$ and $3°$ appear like the mirrored version of each other.

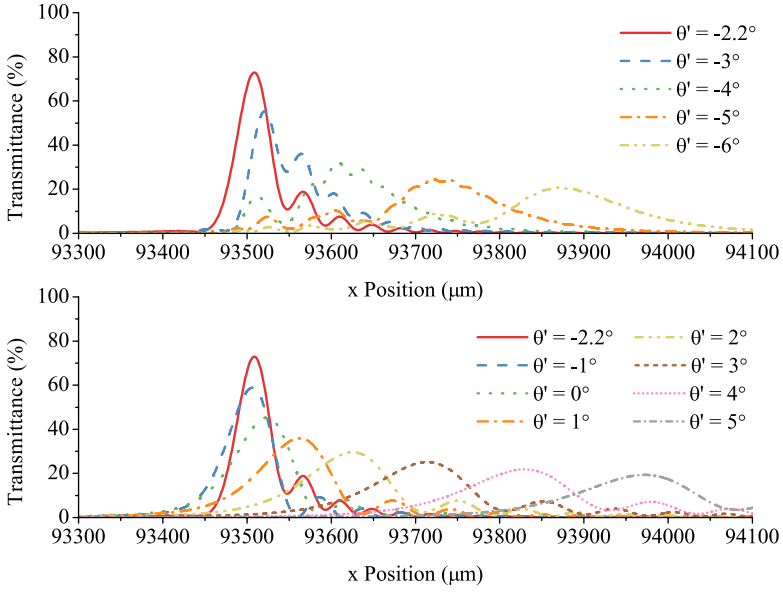

Figure 3.10: The transmission curves for a Fizeau interferometer at different values of the angle of incidence.

Rotating a Fizeau interferometer around the wedge apex or changing the incidence angle of the light impinging on the filter is equivalent to rotating the coordinate system of the wedge. Therefore, the effect of filter-detector separation can be analyzed, since the same interference pattern can be observed at different detector planes at different

incidence angles. The transmission curves of the Fizeau wedge described above are simulated at normal and optimum incidence for various filter-detector separation values and the results are shown in Fig. 3.11. The value of the incidence angle that would be required for the same optimum transmission curve at increasing filter-detector separation would be more negative. The reason is that the z-position of the beam waist of the interfering waves shifts with the incidence angle and by adjusting the incidence angle, beam width on the detector plane can be minimized to achieve a narrower transmission curve [23]. A similar reasoning holds for normal incidence; as the detector plane moves away from the filter, the z-position of the beam waist diverges from the optimum resulting in a wider transmission curve with lower peak transmittance.

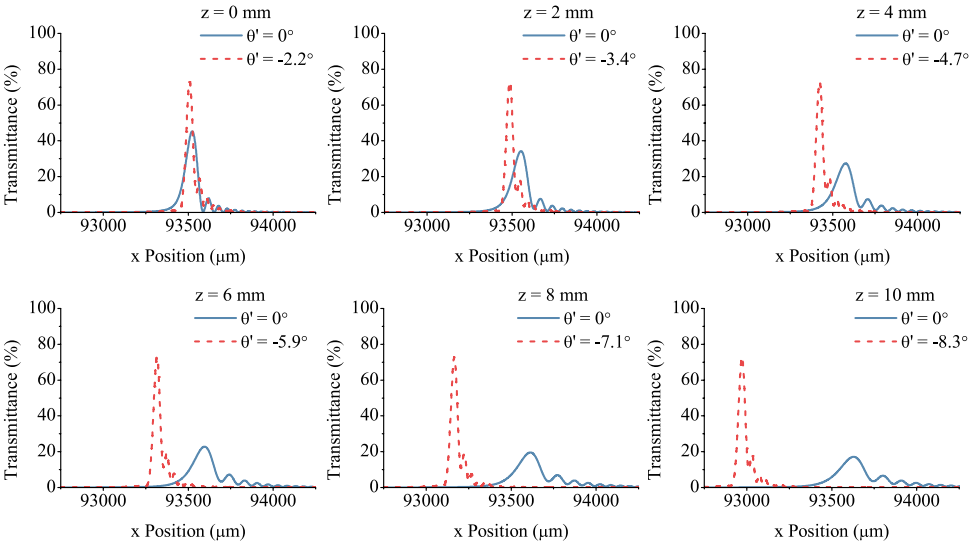

Figure 3.11: The effect of filter-detector separation on the spectral response of a Fizeau interferometer.

Are these results relevant to our devices? In an integrated MEMS implementation of an LVOF and a detector array, the filter-detector separation is negligible. However, even if the detector is placed right after the filter, the optimum incidence angle has an offset. Moreover, filter-detector spacing is inevitable in characterization. By studying the discrepancy between theory and experiment at nonzero filter-detector separation, the optimum incidence angle can be adjusted for the final device, where the filter would be right on top of the detector array.

3.3.3. THE EFFECT OF CONE ANGLE

The light source was assumed to be perfectly collimated in the transmission simulations so far. To achieve a perfectly collimated light beam, a point source must be placed at

the focal point of a lens. However, in reality, a light source has a finite size and the rays emerging from the part of the source that does not lie on the optical axis result in the divergence of the light. Therefore, the effect of collimation of the light source should be taken into account in the optical simulations. The effect of collimation of the light on FP filters had been both theoretically and experimentally discussed [24, 25]. Due to the cosine effect given in Eq. 3.5, all the beams, except for the one normal to the filter, shift the transmission curve to the shorter wavelengths. Hence, the overall transmission response of the filter will decrease in amplitude, while moving to a shorter wavelength than before. For low resolution filters the effect of cone angle is negligible. However, high resolution filters as in this application are very sensitive to even small changes in the cone angle.

A cone of beam with a half cone angle of ψ and amplitude $A^{(i)}$ can be described as a collection of N beams with an amplitude of $A^{(i)}/N$ and incidence angles ranging between $-\psi$ and ψ, as shown in Fig. 3.12. By calculating the interference of all these waves, the effect of cone angle on an FP or a Fizeau interferometer can be simulated.

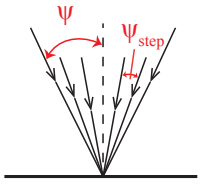

Figure 3.12: The illustration of a cone of light beam impinging on the flat mirror of an LVOF.

In addition to the transmission response of the FP interferometer operating at the 15^{th} order, the Fizeau interferometer that has been introduced before is simulated at $z = 0\,\text{mm}$ for various half cone angle values divided into a number of beams that correspond to $\psi_{step} = 0.1°$ in the angle of incidence. As shown in Fig. 3.13(a), the transmission curves of the FP interferometer widen and move toward shorter wavelengths as the cone angle of the light increases. Also, in agreement with the theory, the overall transmittance decreases with increasing cone angle. In the spectral response of the Fizeau interferometer on the other hand, the transmission curves corresponding to 0.5°, 1° and 2° half cone angle move to shorter wavelengths or equivalently to smaller x-position values, while having lower peak transmittance compared to perfect collimation, as shown in Fig. 3.13(b). However, at even higher values of the half cone angle, the peak of the transmission curves start moving slightly to the right. This change in the spectral response does not coincidentally occur between 2° and 3° of half cone angle, where the absolute value of the optimum incidence angle of −2.2° resides. Correlated to the effect of the incidence angle, as was shown in Fig. 3.10, the transmission curves shift to higher

x-position values at incidence angles that are lower than the optimum value. Therefore, the overall response of the interferometer at a half cone angle higher than 2.2° shifts away from the wedge apex. The decrease in the peak transmittance on the other hand is linearly linked to the increase in half cone angle at which the Fizeau interferometer is less sensitive. This difference can be explained by the uneven structure of the Fizeau interferometer. In the FP interferometer, the mirrors are perfectly parallel while in the Fizeau interferometer, the light beam -even if it is normal to the surface-, is shifting to the sides due to nonparallel mirrors. In other words, the effect of a converging beam is partially similar to the operating principle of the Fizeau interferometer. Therefore, the effect of cone angle is less significant in the Fizeau interferometer compared to the FP interferometer.

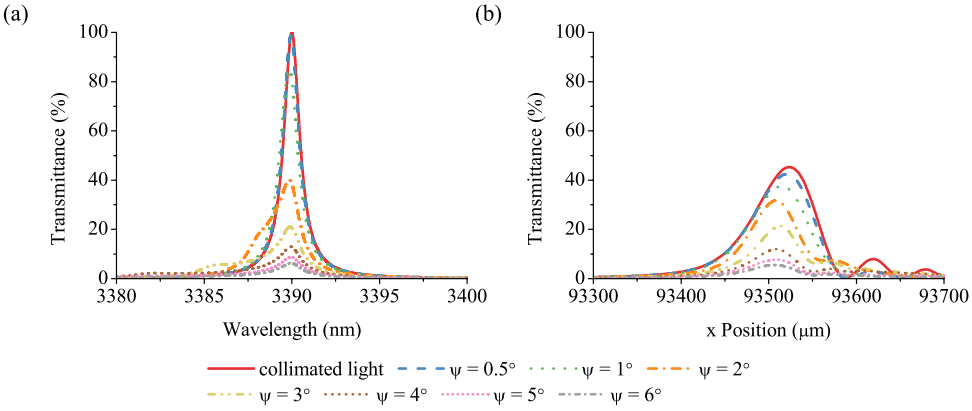

Figure 3.13: The effect of cone angle on the spectral response of (a) FP and (b) Fizeau interferometer, both operating at the 15th order with a reflectivity of $R = 0.985$.

Out of the three aspects that have been analyzed using the description of LVOF in terms of the Fizeau interferometer, the dependence of the transmittance on cone angle of the light source is the only external constraint. The results indicate that a highly collimated light source with a half cone angle of less than 2° is required for proper operation of the LVOF at demanding conditions.

REFERENCES

[1] G. Hernández, *Fabry-Perot Interferometers*, Vol. 3 (Cambridge University Press, 1988).

[2] J. H. Correia, G. de Graaf, S. H. Kong, M. Bartek, and R. F. Wolffenbuttel, *Single-chip CMOS optical microspectrometer,* Sensors and Actuators A: Physical **82**, 191 (2000).

[3] R. Rubio, J. Santander, J. Fonollosa, L. Fonseca, I. Gràcia, C. Cané, M. Moreno, and S. Marco, *Exploration of the metrological performance of a gas detector based on an array of unspecific infrared filters,* Sensors and Actuators B: Chemical **116**, 183 (2006).

[4] L. Fonseca, R. Rubio, J. Santander, C. Calaza, N. Sabaté, P. Ivanov, E. Figueras, I. Gràcia, C. Cané, S. Udina, M. Moreno, and S. Marco, *Qualitative and quantitative substance discrimination using a CMOS compatible non-specific NDIR microarray,* Sensors and Actuators B: Chemical **141**, 396 (2009).

[5] J. H. Correia, M. Bartek, and R. F. Wolffenbuttel, *Bulk-micromachined tunable Fabry–Perot microinterferometer for the visible spectral range,* Sensors and Actuators A: Physical **76**, 191 (1999).

[6] N. Neumann, M. Ebermann, S. Kurth, and K. Hiller, *Tunable infrared detector with integrated micromachined Fabry–Perot filter,* Journal of Micro/Nanolithography, MEMS, and MOEMS **7**, 021004 (2008).

[7] J. S. Milne, J. M. Dell, A. J. Keating, and L. Faraone, *Widely tunable MEMS-based Fabry-Perot filter,* Journal of Microelectromechanical Systems **18**, 905 (2009).

[8] J. Antila, A. Miranto, J. Mäkynen, M. Laamanen, A. Rissanen, M. Blomberg, H. Saari, and J. Malinen, *MEMS and piezo actuator-based Fabry-Perot interferometer technologies and applications at VTT,* in *SPIE Proceedings* (2010) pp. 76800U–76800U.

[9] J. P. Coates, *New microspectrometers: Building on the principle that simple is beautiful,* (2000).

[10] A. Piegari and J. Bulir, *Variable narrowband transmission filters with a wide rejection band for spectrometry,* Applied Optics **45**, 3768 (2006).

[11] A. Emadi, H. Wu, G. de Graaf, and R. Wolffenbuttel, *Design and implementation of a sub-nm resolution microspectrometer based on a linear-variable optical filter,* Optics Express **20**, 489 (2012).

[12] M. Born and E. Wolf, *Principles of Optics: Electromagnetic Theory of Propagation, Interference and Diffraction of Light*, 7th ed. (Cambridge University Press, 1999).

[13] A. D. Rakić, A. B. Djurišić, J. M. Elazar, and M. L. Majewski, *Optical properties of metallic films for vertical-cavity optoelectronic devices,* Applied Optics **37**, 5271 (1998).

[14] R. Bünnagel, H. A. Oehring, and K. Steiner, *Fizeau interferometer for measuring the flatness of optical surfaces,* Applied Optics **7**, 331 (1968).

[15] J. Brossel, *Multiple-beam localized fringes: Part I.-Intensity distribution and localization,* Proceedings of the Physical Society **59**, 224 (1947).

[16] K. Kinosita, *Numerical evaluation of the intensity curve of a multiple-beam Fizeau fringe,* Journal of the Physical Society of Japan **8**, 219 (1953).

[17] T. Hall, *Fizeau interferometer profiles at finite acceptance angles,* Journal of Physics E: Scientific Instruments **2**, 837 (1969).

[18] M. A. Rob, *Limitation of a wedged étalon for high-resolution linewidth measurements,* Optics Letters **15**, 604 (1990).

[19] P. Langenbeck, *Fizeau interferometer - fringe sharpening,* Applied Optics **9**, 2053 (1970).

[20] Y. H. Meyer, *Fringe shape with an interferential wedge,* Journal of the Optical Society of America **71**, 1255 (1981).

[21] J. R. Rogers, *Fringe shifts in multiple-beam Fizeau interferometry,* Journal of the Optical Society of America **72**, 638 (1982).

[22] T. T. Kajava, H. M. Lauranto, and R. R. E. Salomaa, *Fizeau interferometer in spectral measurements,* Journal of the Optical Society of America B **10**, 1980 (1993).

[23] R. R. McLeod and T. Honda, *Improving the spectral resolution of wedged etalons and linear variable filters with incidence angle,* Optics Letters **30**, 2647 (2005).

[24] C. R. Pidgeon and S. D. Smith, *Resolving power of multilayer filters in nonparallel light,* Journal of the Optical Society of America **54**, 1459 (1964).

[25] M. L. Baker and V. L. Yen, *Effects of the variation of angle of incidence and temperature on infrared filter characteristics,* Applied Optics **6**, 1343 (1967).

4

Optical Design

BENCHTOP spectrometers are widely used for material identification through optical absorption in a diverse range of fields, such as medicine [1–5], forensics [6, 7], quality control [8, 9], research [10, 11] and atmospheric [12–14] applications. In these instruments light is passed through a sample and the ratio of transmitted to incident radiation is recorded over a wide wavelength range, usually in the infrared (IR). The acquired spectrum is then compared to a database to identify the composition of the sample [15]. These instruments usually employ the Fourier transform infrared spectroscopy (FTIR) technique. FTIR spectrometers are composed of a broadband light source, a Michelson interferometer, a detector and collimating and focusing optics [16]. The interferometer (with Au coated flat mirrors) and the optics (Au coated parabolic and elliptic mirrors, ZnSe beam splitter, KBr windows) are coated such that these can be operated over a wide wavelength range. With a broadband light source and a wideband detector, an FTIR spectrometer can cover a large part of the spectrum (2.5 µm to 16 µm); therefore, is capable of analyzing a large variety of materials. Although FTIR spectrometers are in high demand due to their wide operating wavelength range and high resolution, these instruments are cumbersome laboratory equipment with high cost.

Many applications would favor portable instruments, which has triggered the development of handheld spectrometers. Microelectromechanical system (MEMS) implementations of the Michelson interferometer [17, 18] and examples of a slightly more robust interpretation, called lamellar grating interferometer (LGI) [19, 20], have been reported in the literature. Despite these efforts, there are only a handful of portable spectrometers available in the market [21, 22].

Miniaturization of benchtop spectrometers, while maintaining the wide wavelength range operation, is challenging. Moreover, the movable components in the interferometer compromise the robustness of miniaturized spectrometers, especially in handheld applications. Interference filter based microspectrometers offer a significant reduction in size and improvement in robustness in exchange for limited wavelength range and resolution [23]. Therefore, a linear variable optical filter (LVOF) combined with a miniaturized light source, a detector array and a sample chamber can serve as a wafer-level microspectrometer in a rather narrow wavelength range compared to general-purpose benchtop spectrometers.

The optical design of the interference filter based microspectrometers relies mainly on the application. The optical design flow of an interference filter is summarized in Fig. 4.1. The operating wavelength range and the required resolution is selected based on the spectra of the samples to be distinguished. Then, the operating order and the mirror reflectivity must be calculated to achieve the required resolution. The mirror reflectivity and the overall operation of the filter depend highly on the material selection. The refractive index contrast between the mirror materials is crucial for obtaining high re-

flectivity. Moreover, materials must be non-absorbing in the desired wavelength range to maximize the light throughput after transmission as the proper operation of the filter is assured.

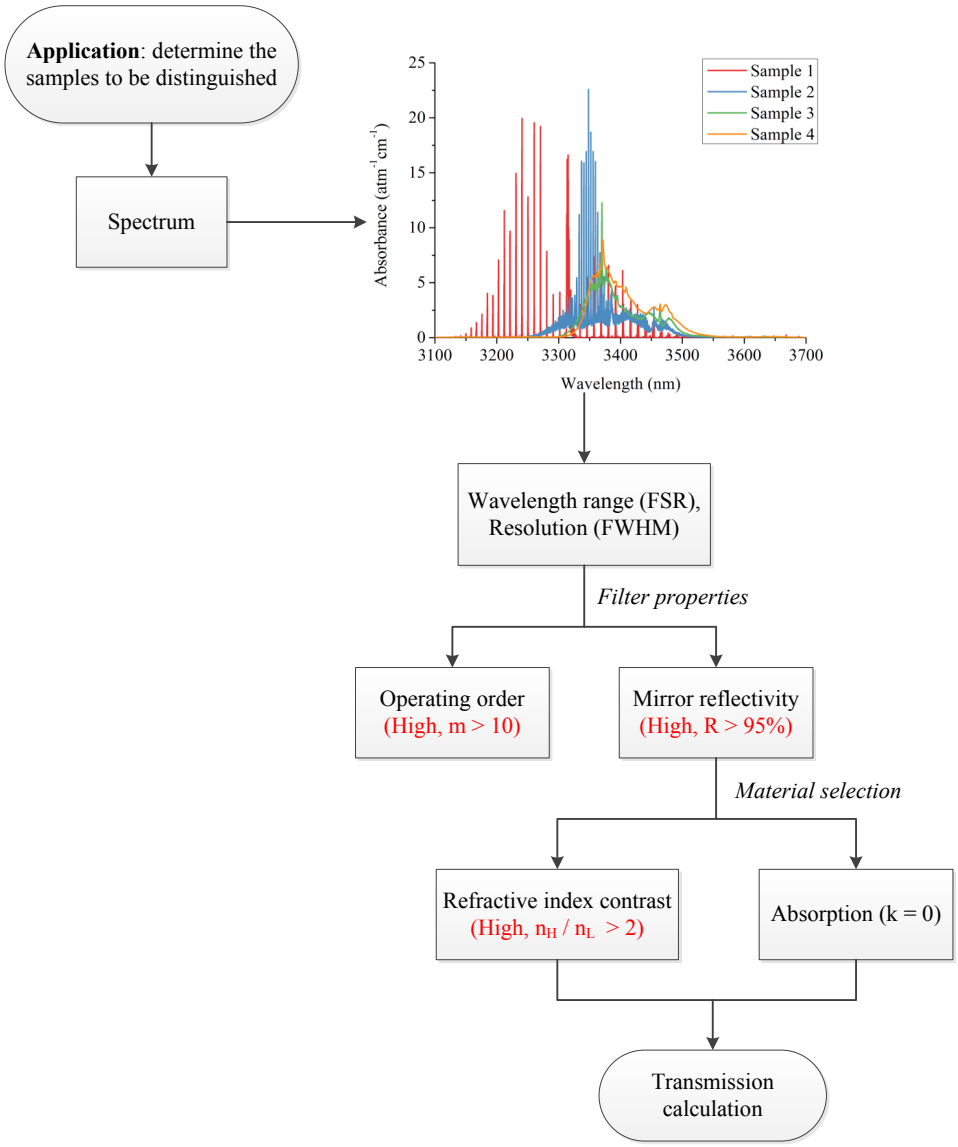

Figure 4.1: Flowchart for the optical design of an interference filter. The requirements depicted in red are for the use of the filter cavity also as a gas cell.

As discussed in chapter 3, the use of the resonator cavity of an LVOF also as a gas cell

requires a mm-level effective optical path length. To achieve such an effective optical path length, the physical length of the resonator cavity must be relatively high, which forces the filter to operate at a high order ($m > 10$). Moreover, the mirrors on both sides of the cavity must be highly reflective ($R > 95\%$) to enhance elongation through multiple reflections between these mirrors. The material selection for the mirrors becomes crucial when high reflectivity is required. The optical properties, refractive index (n) and extinction coefficient (k) of the layers, determine the spectral response of the mirror. Therefore, these must be carefully studied.

In this chapter, the optical design of the gas-filled LVOF is explained step-by-step. The operating wavelength range and the resolution required to distinguish the different hydrocarbons in natural gas are extracted from their mid-IR spectrum. Based on these specifications and considering the particular requirements imposed by the application of using the cavity of the LVOF also as a gas cell, the operating order and mirror reflectivity are subsequently discussed. After explaining the rationale behind the material selection, the transmission calculations with and without the gas are presented.

4.1. SPECTRA OF HYDROCARBONS

Hydrocarbons have a fingerprint region in the 3.1 µm to 3.7 µm wavelength range in the mid-IR. For the selection of the operating wavelength range of the filter and the required resolution to distinguish these gases, the spectral response must be analyzed. Moreover, since the cavity of the LVOF is also used as a gas cell, the absorbance of the gases must be taken into account in the optical design.

The absorption coefficient is a wavelength-dependent intrinsic property of a material that is influenced solely by pressure and temperature. The absorbance or transmittance, on the other hand, is dependent on both the optical path that the light beam travels through the sample and the instrument resolution. Since the resolving power of the LVOF determines the instrument resolution in this application, it is crucial to use the correct *evaluated absorption coefficient* (i.e. values that are calculated by modifying the absorption coefficient using the appropriate instrument resolution). Taking the corrected values for unit optical path length (OPL) would enable the use as an exponential attenuation factor in the optical simulations.

There are three main databases available to the public for infrared absorption spectra of hydrocarbons in the gas phase. In the following sections these three databases are briefly described and the differences between them are outlined.

4.1.1. NIST DATABASE

The National Institute of Standards and Technology (NIST) provides the measured transmittance and absorbance spectra of hydrocarbons [24]. The database covers a wide wavelength range in the IR from 2.2 µm to 22 µm. The grating-based measurement instrument has a resolution of 4 cm^{-1} and an optical path length of 5 cm. The sample gas is diluted with nitrogen at 1:3 ratio to reach 600 mmHg total pressure. The evaluated absorption coefficient per unit pressure (1 atm) and unit optical path length (1 mm) is extracted from NIST database for methane, ethane, propane and butane as shown in Fig. 4.2.

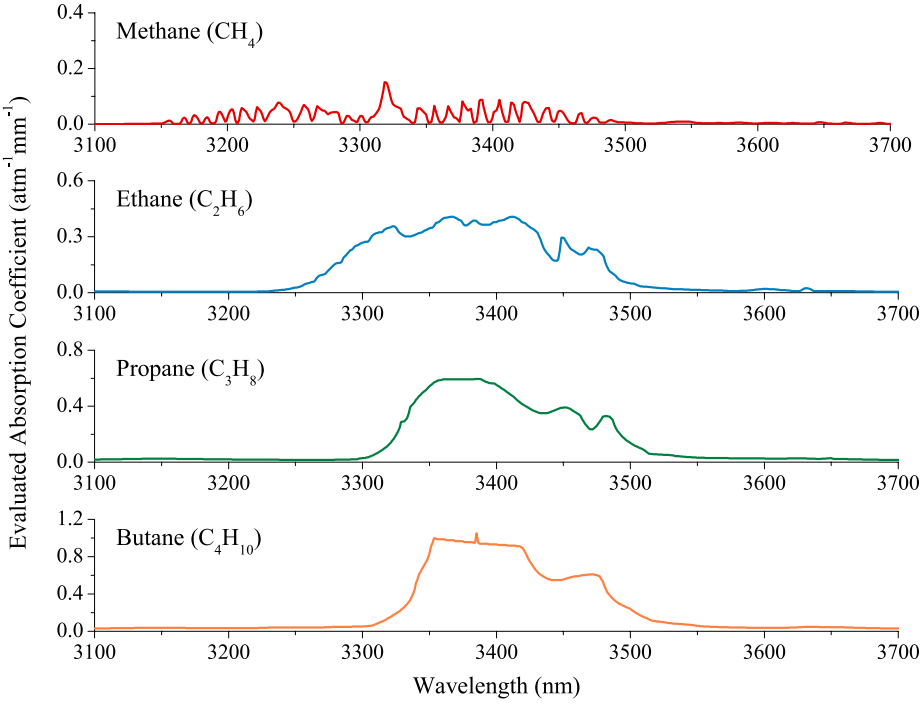

Figure 4.2: The evaluated absorption coefficient spectra of methane, ethane, propane and butane per unit pressure and optical absorption path extracted from NIST database.

4.1.2. PNNL DATABASE

Pacific Northwest National Laboratory (PNNL) presents vapor-phase infrared spectra of pure chemicals in a narrower window in the IR (1.5 µm to 16.6 µm) [25]. The data is captured by the FTIR spectrometer IFS 66v/s (Bruker Optics, Germany) at 0.112 cm^{-1} resolution. The spectral data is given as absorbance for a unit sample concentration of 1 ppm over a unit optical path length of 1 m at a temperature of 25 °C. The evaluated absorption

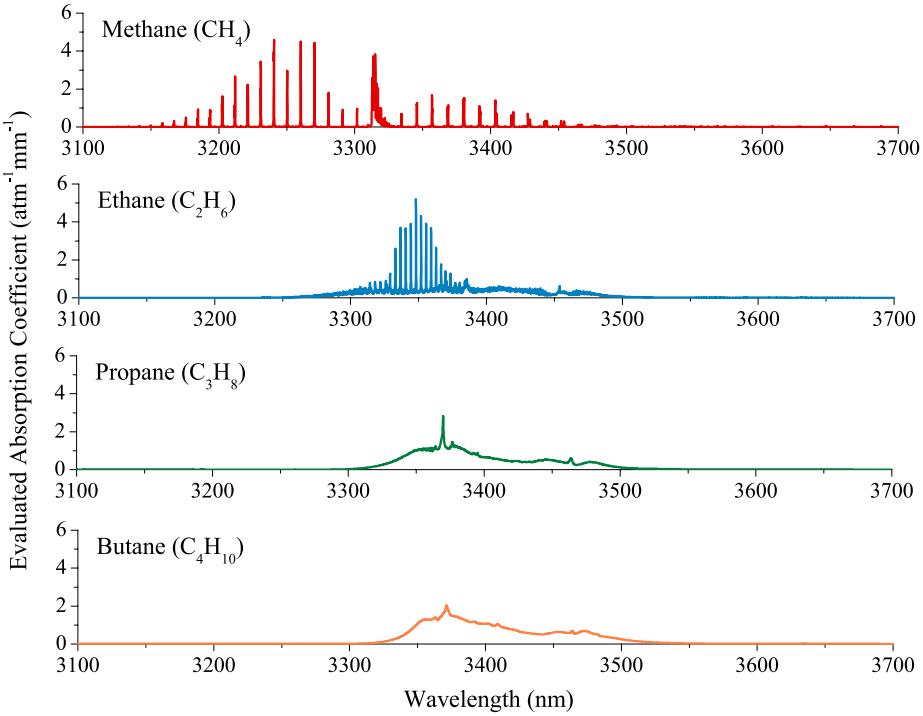

Figure 4.3: The evaluated absorption coefficient spectra of methane, ethane, propane and butane per unit pressure and optical absorption path extracted from PNNL database.

coefficients of methane, ethane, propane and butane are subsequently extracted using Naperian conversion (natural logarithm). These spectra are shown in Fig. 4.3.

Compared to the NIST database, PNNL offers more detailed spectra due to the high-resolution measurements. As evident from the spectra of especially methane and ethane, it is obvious that narrower spectral lines can be measured if instruments with higher resolving power are used. It should also be noted that the peak evaluated absorption coefficient values also increase as the resolving power gets higher. For our application, the dependence of absorption coefficient on the instrument resolution is crucial for proper calculation of the optical path elongation that the devices can achieve.

4.1.3. HITRAN DATABASE

HITRAN is a high-resolution molecular absorption database for the analysis of atmospheric gases. The data that is presented as line-by-line intensity in cm/mol is a combination of direct observation, theoretical calculation and semi-empirical values [26]. To be able to use this high-resolution spectral data, first a Voigt broadening function is applied. Then, based on the resolution of the instrument, which is the FWHM resolution of

the LVOF in our application, a Gaussian function is convolved with the spectrum to calculate the absorbance that can be resolved by the filter. By choosing a unit optical path length of 1 mm, the evaluated absorption coefficient that can be resolved by the filter is achieved, which can later be used in the optical simulations for other optical path length values. Data manipulation is performed using the information-calculating system Spectroscopy of Atmospheric Gases, http://spectra.iao.ru (ICS SPECTRA) [27]. Among the hydrocarbons that we are interested in, only the spectrum of methane is fully covered in the desired wavelength range. As an example, the evaluated absorption coefficient for methane is extracted from the HITRAN database using a Gaussian profile with 0.1 cm^{-1} resolution and the result is shown in Fig. 4.4.

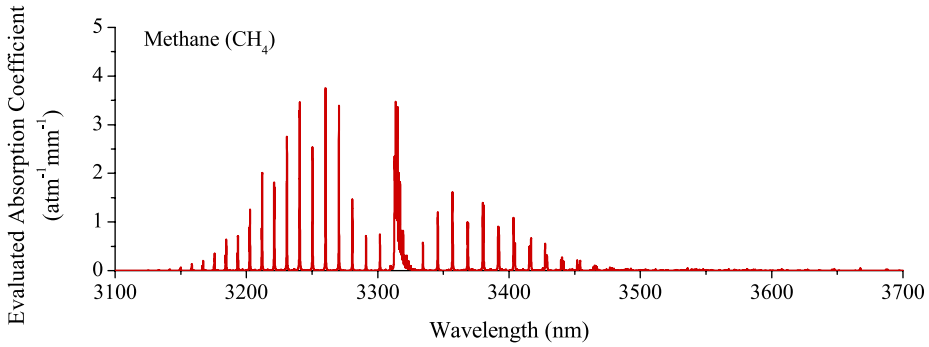

Figure 4.4: The evaluated absorption coefficient of methane per unit pressure and optical absorption path extracted from HITRAN database using a Gaussian profile with 0.1 cm^{-1} resolution.

To compare the HITRAN database to the PNNL database, evaluated absorption coefficient of methane is extracted from the HITRAN database per unit pressure and optical path at 0.112 cm^{-1} resolution. In the modification of the HITRAN database, a sinc function instead of the Gaussian profile is employed to replicate the effect of Michelson interferometer in the FTIR measurements of the PNNL database. As shown in Fig. 4.5, at the same resolution, these two databases exhibit a highly similar spectral performance with slight differences at the peak positions. The difference can be explained by the data acquisition method; the PNNL database is extracted from measurements only, while the HITRAN database is a combination of measurement and theoretical calculations.

The modification of the absorption coefficient according to the resolution of the device is crucial for both the optical simulations and the analysis of the experimental data. As will be discussed in Chapter 6, a highly collimated laser is used for characterization of the sensor. Compared to the filter, the laser has very high resolution (i.e. narrow linewidth). Therefore, the resolution of the system is defined by the light source rather than the filter in the measurements with gas. This leads to the preferred use of high-resolution HITRAN database rather than PNNL or NIST for quantitative analysis in this

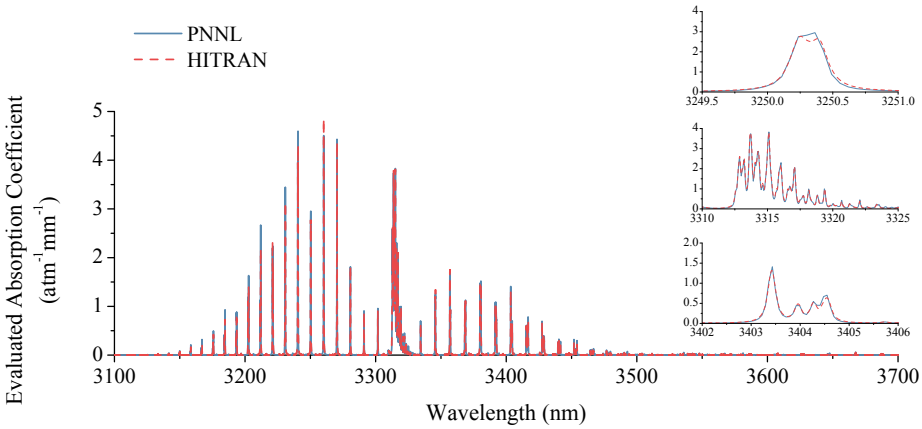

Figure 4.5: The comparison of PNNL and HITRAN databases. The evaluated absorption coefficient of methane per unit pressure and optical absorption path extracted from the PNNL database with a measured resolution of 0.112 cm^{-1} while the HITRAN database is modified using a sinc profile with the same resolution. The insets show three absorption peaks at different wavelengths in detail.

thesis.

4.2. OPERATING ORDER

In the previous chapter, it was shown that an LVOF must be designed using the Fizeau approach, rather than the Fabry-Perot (FP) approximation at demanding operating conditions. However, for a quick assessment of the relation between the operating order, resonator thickness and bandwith, FP approach provides adequate results. As previously explained, when the phase difference between two successive waves becomes equal to 2π, the spectral response of the filter starts repeating itself. For normal incidence ($\theta' = 0°$) and air cavity ($n' = 1$), Eq. 3.5 can be simplified to $\frac{4\pi}{\lambda_0} h = 2\pi m$, where m is the operating order, h is the resonator layer thickness or the physical cavity length in this case and λ_0 is the wavelength to be transmitted when the filter is illuminated with a broadband light source. This equation indicates that at a given physical cavity length, the filter transmits multiple wavelengths, depending on the operating order. Due to this repetitive spectral response, FP filters are usually combined with optical band-pass filters for proper operation in the desired wavelength range.

The spectral response of an FP filter with an air cavity is simulated at $R = 0.85$ and $h = 24.75\,\mu$m using the theoretical description given in the previous chapter. As shown in Fig. 4.6, the spectral separation between successive operating orders become smaller as the operating order increases. Therefore, a filter can operate in a wide wavelength range either by moving one of the mirrors as in a tunable FP filter, or by tapering the cavity

length as in an LVOF, provided that the transmission curve of the next order remains out of this band.

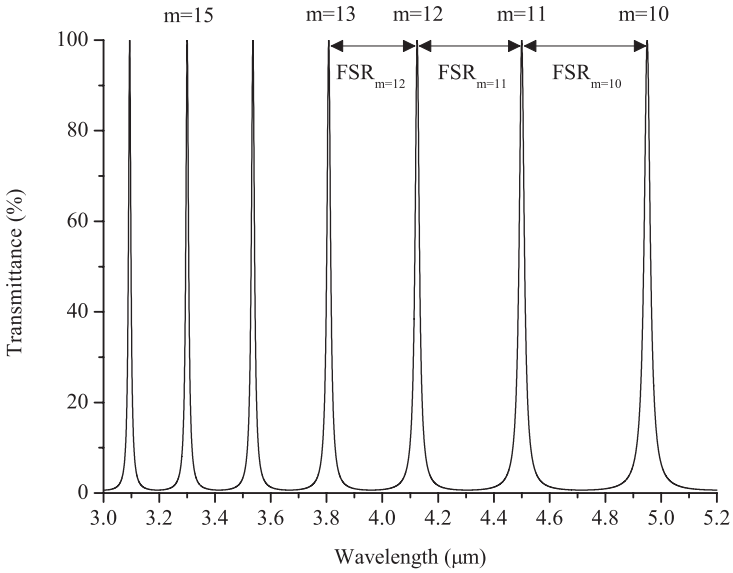

Figure 4.6: The transmission curves calculated for an FP filter with air cavity at $R = 0.85$ and $h = 24.75\mu m$.

The free spectral range (FSR) describes the operating wavelength range of a wide-band interference filter. For a filter operating at the m^{th} order, FSR is defined as the spectral separation between the m^{th} and the $(m+1)^{th}$ order. Using the constructive interference condition $\frac{4\pi}{\lambda_0}h = 2\pi m$, while assuming normal incidence ($\theta' = 0°$) and air cavity ($n' = 1$) to extract the position of the m^{th} and the $(m+1)^{th}$ orders in wavelength, FSR_m can be calculated as

$$FSR_m = \frac{2h}{m} - \frac{2h}{m+1} = \frac{2h}{m(m+1)}. \tag{4.1}$$

In an operating bandwidth from λ_{min} to λ_{max}, the FSR is limited by the minimum wavelength. Using the interference equation, the FSR can be defined in terms of m and λ_{min} as given in Eq. 4.2.

$$FSR_m = \frac{2h}{m(m+1)} = \frac{\lambda_{\min} m}{m(m+1)} = \frac{\lambda_{\min}}{(m+1)} \tag{4.2}$$

As investigated in the previous section, hydrocarbons have a fingerprint region at the 3.1 μm to 3.7 μm wavelength range in the mid-IR with characteristic absorption peaks. However, selecting such a wide wavelength range limits the operating order to $m = 4$, thereby restricting the physical cavity length to less than 10 μm. To be able to use the

resonator cavity of the filter also as a gas cell, the physical cavity must be elongated to a mm-level effective OPL. Considering the fact that mirror reflectivity is strongly dependent on actual layer thicknesses, which are subject to tolerances in deposition rate of the equipment used, starting with moderate values of the reflectivity combined with a long resonator cavity provides a higher chance of achieving sufficient absorption in the device. Therefore, instead of the wide 3.1 µm to 3.7 µm region, a narrower wavelength range where the spectra of hydrocarbons have distinguishing signatures, namely 3.2 µm to 3.4 µm, is selected. In this narrow band, methane (CH_4) has oscillating absorption peaks through the entire range, while ethane (C_2H_6) starts to absorb light around 3.25 µm. This provides a spectral window to distinguish between methane and ethane easily. Propane (C_3H_8) and butane (C_4H_{10}) on the other hand have very similar spectra starting from 3.3 µm and require detailed post-processing analysis to extract their individual concentrations from the spectrum of a mixture.

Selecting $\lambda_{min} = 3.2\,\mu m$ and 200 nm as the minimum operating bandwidth, one can calculate that the highest operating order is $m = 15$ using Eq. 4.2. This translates into a physical cavity length that varies from $h_1 = 24\,\mu m$ to $h_2 = 25.5\,\mu m$, corresponding to $\lambda_{min} = 3.2\,\mu m$ and $\lambda_{max} = 3.4\,\mu m$ respectively.

4.3. REFLECTIVITY

The use of the LVOF as a gas cell in addition to a wavelength-selective device requires highly reflective mirrors to enhance the optical path elongation. In the previous chapter, it was shown that even a slight change in reflectivity has a substantial effect on the peak transmittance at reflectivity values higher than 90%. Moreover, the effect is more profound at high order of operation as is actually required in this application.

As explained in the following chapter about fabrication, the tapered cavity results from bonding a flat mirror with a tapered mirror at the wafer-level. Both mirrors are of Bragg type and composed of thin-film layers. Since the tapered mirror is fabricated by tapering one of the thin-film layers, the spectral response of the mirror becomes position dependent, as the thickness of the tapered layer changes along the length of the filter.

In this section, firstly the transfer-matrix method for calculating the spectral response of the Bragg mirrors is introduced. Subsequently, the available materials that are suitable for mid-IR and their optical characterization are discussed. Lastly, the design and the optimization of the Bragg mirrors are presented.

4.3.1. TRANSFER-MATRIX METHOD

The transfer-matrix method is used to analyze the propagation of electromagnetic waves through a layered medium in one-dimensional systems [28, 29]. It is commonly em-

ployed in the design of optical filters, antireflection coatings and polarizers [30, 31]. In the transfer-matrix method, propagation through each layer and boundary can be described with a matrix. Since it is a one-dimensional system, there are two components of a wave at every boundary, one going left and one going right and also two states of the wave, one before and one after the boundary. Also for the propagation through a layer, left and right going components exist with two states, one at the beginning and one at the end of the layer. Therefore, both boundaries and layers can be represented by 2×2 matrices.

Propagation through a multilayer of thin-films with N layers is illustrated schematically in Fig. 4.7. The wave is assumed to propagate from left to right. The parameters of incidence and exit media are represented with subscripts 0 and N+1, respectively. The incident wave is reflected and refracted at every boundary and the left and right going waves are shown with superscripts L and R. An additional star means that the quantity belongs to the right side of the boundary. The thicknesses of the layers are represented by $h_1, h_2, ..., h_N$, while the refractive indices of the media are indicated as $n_0, n_1, ..., n_N, n_{N+1}$. The angles of refraction at each boundary $(\theta_0, \theta_1, ..., \theta_N, \theta_{N+1})$ are correlated by Snell's Law.

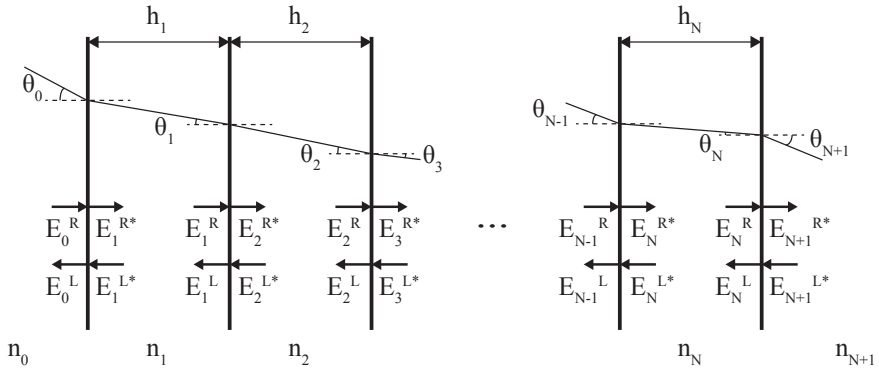

Figure 4.7: A multilayer of thin-films.

The transition through a boundary from its right to its left is described by the refraction matrix **W**,

$$\begin{pmatrix} E^R_{k-1} \\ E^L_{k-1} \end{pmatrix} = \mathbf{W}_{k-1,k} \begin{pmatrix} E^{R*}_k \\ E^{L*}_k \end{pmatrix} = \frac{1}{t_{k-1,k}} \begin{pmatrix} 1 & r_{k-1,k} \\ r_{k-1,k} & 1 \end{pmatrix} \begin{pmatrix} E^{R*}_k \\ E^{L*}_k \end{pmatrix}, \tag{4.3}$$

where $r_{k-1,k}$ and $t_{k-1,k}$ are the Fresnel coefficients for reflection and transmission respectively. The Fresnel coefficients for p- (i.e. parallel polarization, TM wave) and s-polarization (i.e. perpendicular polarization, TE wave) are calculated as follows [32]:

$$
\begin{aligned}
r^p_{k-1,k} &= \frac{n_{k-1}\cos\theta_k - n_k\cos\theta_{k-1}}{n_{k-1}\cos\theta_k + n_k\cos\theta_{k-1}} \\
t^p_{k-1,k} &= \frac{2n_{k-1}\cos\theta_{k-1}}{n_{k-1}\cos\theta_k + n_k\cos\theta_{k-1}} \\
r^s_{k-1,k} &= \frac{n_{k-1}\cos\theta_{k-1} - n_k\cos\theta_k}{n_{k-1}\cos\theta_{k-1} + n_k\cos\theta_k} \\
t^s_{k-1,k} &= \frac{2n_{k-1}\cos\theta_{k-1}}{n_{k-1}\cos\theta_{k-1} + n_k\cos\theta_k}
\end{aligned}
\quad . \tag{4.4}
$$

The propagation through a layer is defined by the phase matrix $\mathbf{P}$,

$$
\begin{pmatrix} E^{R*}_k \\ E^{L*}_k \end{pmatrix} = \mathbf{P}_k \begin{pmatrix} E^R_k \\ E^L_k \end{pmatrix} = \begin{pmatrix} e^{i\delta_k} & 0 \\ 0 & e^{-i\delta_k} \end{pmatrix} \begin{pmatrix} E^R_k \\ E^L_k \end{pmatrix}, \tag{4.5}
$$

where $\delta_k = \frac{2\pi}{\lambda} n_k h_k \cos\theta_k$ is the phase difference introduced by the k$^{\text{th}}$ layer.

The system transfer matrix is therefore the multiplication of the refraction and propagation matrices of all the boundaries and layers that the light travels through as shown in Eq. 4.6.

$$
\begin{pmatrix} E^R_0 \\ E^L_0 \end{pmatrix} = \underbrace{\mathbf{W}_{01}\mathbf{P}_1\mathbf{W}_{12}\mathbf{P}_2\mathbf{W}_{23}\ldots\mathbf{W}_{N-1,N}\mathbf{P}_N\mathbf{W}_{N,N+1}}_{\mathbf{S}} \begin{pmatrix} E^{R*}_{N+1} \\ E^{L*}_{N+1} \end{pmatrix} \tag{4.6}
$$

The reflection and transmission coefficients of the multilayer are calculated as given in Eq. 4.7.

$$
\begin{aligned}
r^R = r_{0,N+1} &= \left.\frac{E^L_0}{E^R_0}\right|_{E^{L*}_{N+1}=0} = \frac{\mathbf{S}_{21}}{\mathbf{S}_{11}} \\
t^R = t_{0,N+1} &= \left.\frac{E^{R*}_{N+1}}{E^R_0}\right|_{E^{L*}_{N+1}=0} = \frac{1}{\mathbf{S}_{11}} \\
r^L = r_{N+1,0} &= \left.\frac{E^{R*}_{N+1}}{E^{L*}_{N+1}}\right|_{E^R_0=0} = -\frac{\mathbf{S}_{12}}{\mathbf{S}_{11}} \\
t^L = t_{N+1,0} &= \left.\frac{E^L_0}{E^{L*}_{N+1}}\right|_{E^R_0=0} = \frac{\mathbf{S}_{11}\mathbf{S}_{22} - \mathbf{S}_{12}\mathbf{S}_{21}}{\mathbf{S}_{11}}
\end{aligned}
\tag{4.7}
$$

As a result, the reflectivity and transmissivity of the multilayer are calculated as,

$$
R = |r|^2, T = |t|^2. \tag{4.8}
$$

COHERENCE

Coherence is a property of an optical system that defines the ability to produce an interference pattern. An optical system is referred to as coherent if the interference effect is at maximum, while incoherence describes the complete lack of it. The coherence of an optical system depends on the variations in both the light source and the system itself. Coherence length is a commonly used term dedicated to the light source, to describe the ability of the light beam to interfere. The coherence related solely to the optical system is defined in terms of the thickness of the optical layers. A thin-film is regarded as coherent, while a substrate must be treated as incoherent due to its thickness and variations in its thickness [33].

The transfer-matrix method assumes coherent thin-film layers, while ignoring the incoherent nature of the substrate, which results in unrealistic high-frequency oscillations in reflectivity and transmissivity of the system. These oscillations are not observed in measurements either due to incoherence of the substrate or the limited sensitivity of the measurement. The spectral response that is observed is the average of the high-frequency fringe pattern. To be able to simulate the optical properties of a multi-layer system that contains both coherent and incoherent layers, two approaches come forward. The first approach clusters the coherent layers and forms the transfer-matrix for each cluster, while the incoherent layers are treated as phase matrices with both having the absolute square of their coefficients, thereby using intensities rather than the field amplitudes. The multiplication of these matrices yields the overall transfer matrix of the system [34]. The second approach introduces an additional factor to the phase difference in the phase matrix given in subsection 4.3.1 from 0 to 2π either randomly [35] or at equidistant values [36] for incoherent layers, followed by averaging at the reflectivity and transmissivity level. Using equidistant values was proved to converge toward the exact solution faster; hence, the optical properties in this thesis are calculated by the transfer-matrix method using phase matrices altered with equidistant phase factors for incoherent substrates.

4.3.2. MATERIAL SELECTION

Material selection is crucial for the optical design of interference filters. To achieve wavelength selection through transmission, non-absorbing materials must be selected for adequate light throughput. As shown in Fig. 4.8, this requirement eliminates many metals such as gold (Au), aluminum (Al) and silver (Ag) that are commonly used in IR mirrors due to their high reflectivity (> 96%) over a wide wavelength range (0.8 µm to 20 µm).

Bragg mirrors are composed of alternate layers of high and low refractive index materials. The reflectivity of a Bragg mirror increases with increasing refractive index contrast between materials (n_{high}/n_{low}) and the number of layers. Since highly reflective Bragg

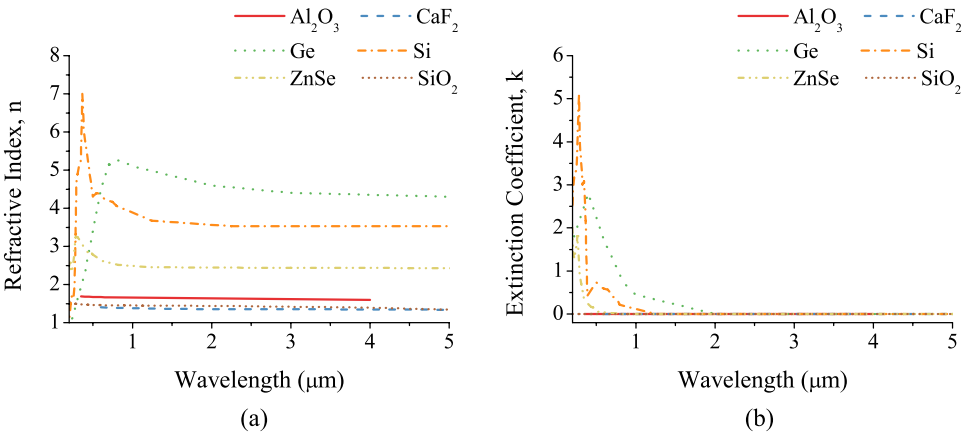

Figure 4.8: The refractive index (a) and extinction coefficient (b) of Ag, Al and Au. The data are extracted from the material database of 'The Essential Macleod'.

mirrors are required for optical path elongation in a transmission filter in this application, extra attention must be paid to the refractive index of materials in addition to their extinction coefficients.

Silicon (Si), germanium (Ge) and zinc-selenide (ZnSe) are commonly used materials in commercially available mid-IR lenses [37]. The latter two are also widely used in anti-reflection coatings in the same wavelength range. Sapphire (Al_2O_3) and calcium fluoride (CaF_2) are often employed as window materials due to their low refractive index and zero extinction coefficient [38]. Silicon-dioxide (SiO_2) is also a non-absorbing material with low-refractive index that is frequently used in clean rooms. The optical properties of these IR materials are given in Fig. 4.9.

The performance of thin-film coatings is highly dependent on the quality of layer deposition. The thickness and the optical properties must be uniform throughout the layer and must be well controlled. Evaporation and sputtering are two widely used physical vapor deposition (PVD) methods for thin-film deposition. In the evaporation technique, the material to be deposited is brought to evaporation through heating inside a vacuum chamber and the vaporized material condenses on the wafer to form the thin-film layer. In sputtering on the other hand, a high voltage is applied between two parallel disks; the target (cathode), which is the material to be deposited and the substrate (anode), where the wafer to be deposited on resides. The inert gas, usually argon (Ar), flowing between these electrodes becomes a plasma when the voltage is applied. The target attracts positive ions from the plasma and these ions hit the target causing the ejection of neutral target atoms or molecules. These neutral atoms or molecules later travel toward the substrate, forming a thin-film layer [39]. The deposition rate of sputtering is usually

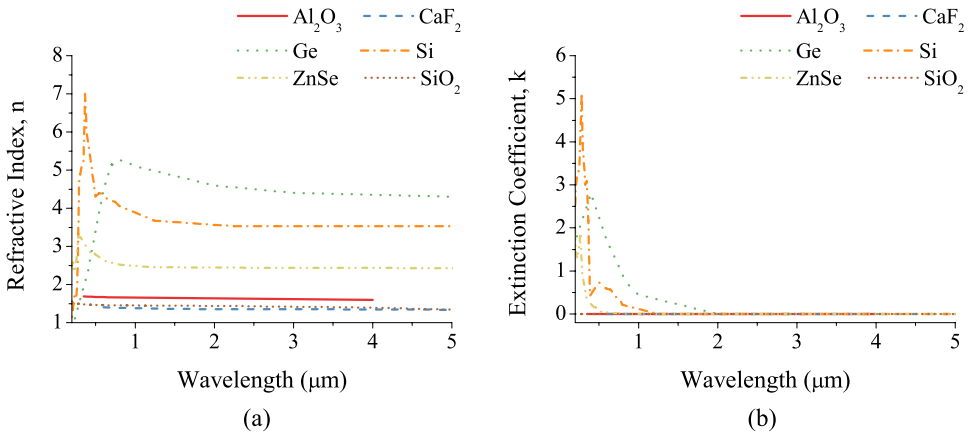

Figure 4.9: The refractive index (a) and extinction coefficient (b) of Al_2O_3, CaF_2, Ge, Si, ZnSe and SiO_2. The data are extracted from the material database of 'The Essential Macleod'.

slower but the film properties are more controllable than in evaporation. Although it is expensive and often used in industry rather than research, sputtering provides films with good uniformity and adhesion with negligible shadowing effect [40]. Due to the availability in our clean room facilities and its desirable performance in terms of uniformity and control over film properties, which is crucial in filter design, sputtering is selected as the thin-film deposition method for this project.

What is more limiting in terms of material selection is the availability of the target materials and related recipes in the instrument. For the instrument we had access to (FHR MS150, FHR Anlagenbau GmbH, Germany), the standard materials were Au, Ti, Si and Al in DC mode as well as TiN, TiO_2, SiO_2, Si_3N_4 and AlN in RF mode, reactively. Due to the availability of the target and its optical properties ($n = 1.41$ and $k = 0$ at $\lambda = 3.3\mu m$), SiO_2 is a very suitable low refractive index material. For the high refractive index material on the other hand, Ge is the best candidate because of its optical properties ($n = 4.38$ and $k = 0$ at $\lambda = 3.3\mu m$) that allows a refractive index ratio of $n_{high}/n_{low} = 3.11$ when combined with SiO_2. Although it is possible to sputter Ge, it was not available as a target in the instrument. Therefore, we selected the next best candidate, Si as the high refractive index material. With optical properties, $n = 3.53$ and $k = 0$ at $\lambda = 3.3\mu m$, Si-SiO_2 combination led to a refractive index ratio of $n_{high}/n_{low} = 2.50$.

THIN-FILM CHARACTERIZATION

Optical properties of thin films are highly dependent on deposition conditions. This necessitates the characterization of thin films at the actual sputtering conditions. Measuring the refractive index and the film thickness allows the designer to adjust the deposition equipment and to fine-tune the design.

Ellipsometry is a commonly used method for thin-film characterization. It measures the complex reflectance ratio (ρ) that describes the change in polarization state of light reflected from the surface of a sample [41]. The complex reflectance ratio is defined as the ratio of p- and s-polarized components of the reflected light, which is measured in terms of Ψ and Δ representing the amplitude ratio and phase difference respectively, as given in Eq. 4.9. Since the ratio of two values is measured in ellipsometry rather than absolute intensity, the results are more accurate and reproducible.

$$\rho = \frac{r_p}{r_s} = \tan(\Psi)\, e^{i\Delta} \tag{4.9}$$

A typical ellipsometer setup consists of a light source, a polarizer, an analyzer and a detector as shown in Fig. 4.10. The unpolarized light beam from the source is linearly polarized by the polarizer. Upon reflection off the sample, which is usually a thin-film layer on a silicon or glass wafer substrate, the light beam becomes elliptically polarized. By measuring the change in the polarization using the analyzer and the detector, the optical properties of the sample can be extracted.

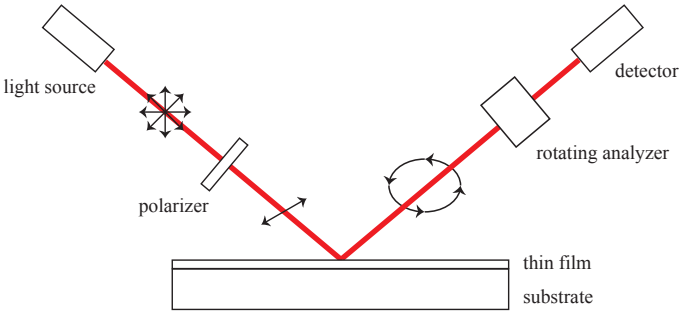

Figure 4.10: A schematic illustration of the ellipsometer setup.

Ellipsometric measurement data cannot be converted to the optical properties of a thin film directly. Following the measurement, a model must be constructed to predict the behavior of the film. The designer must generate data that closely matches the measured optical data by varying the parameters in the model during the fitting process. Quality of the fit is usually measured by the mean-squared error (MSE). The parameters in the model should be varied until the minimum MSE is achieved. After the best fit is attained, the refractive index and the extinction coefficient can be extracted in a wide wavelength range.

By adjusting the deposition recipes, both films have been sputtered on 2" Si wafers with thicknesses that are close to the target film thickness, which is calculated using the existing optical data. According to the previous fabrication runs, the deposition rates

for SiO_2 and Si were 0.225 nm/s and 0.657 nm/s respectively. The SiO_2 was sputtered for 2474 s to achieve a thickness of approximately 560 nm. For Si on the other hand, a shorter deposition time of 343 s was selected to achieve a layer with 230 nm thickness.

Woollam M-2000UI ellipsometer (J.A. Woollam Co. Inc., USA) working in the 245 nm to 1700 nm wavelength range and WVASE ellipsometry analysis software (J.A. Woollam Co. Inc., USA) have been used for material characterization. This instrument is capable of performing measurements at different incidence angles. The confidence in fitting the model is improved using two or three measurements around the Brewster angle. Oblique incidence close to the Brewster angle provides the most sensitive measurement, since the largest changes in polarization occur at these angles. However, for the analysis of simple one-layer coatings as we have, the incidence angle is not crucial. For SiO_2, three measurements at 45°, 50° and 55° have been recorded. The measured and fitted spectra of Ψ and Δ are shown in Fig. 4.11 for these incidence angles.

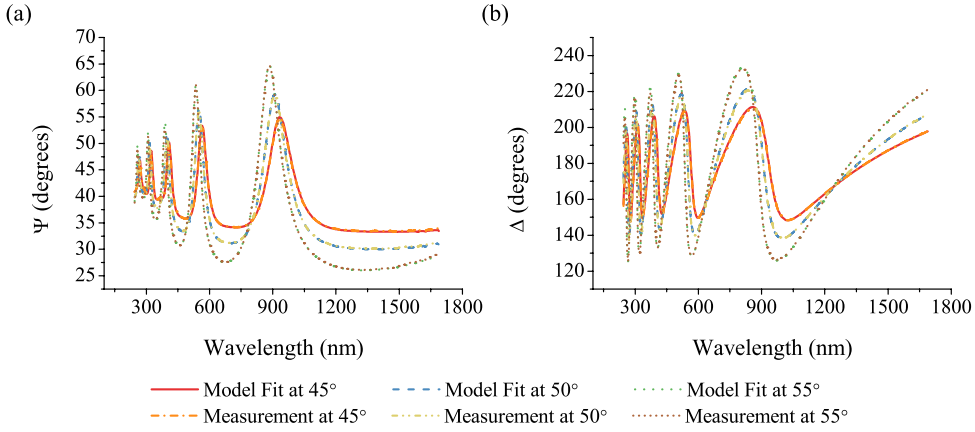

Figure 4.11: Measured (a) Ψ and (b) Δ spectra of the SiO_2 film compared to the model fit at various incidence angles.

The Cauchy model is usually employed to fit dielectric layers. In this model, the refractive index is represented by a slowly varying function of wavelength as $n(\lambda) = A + \frac{B}{\lambda^2} + \frac{C}{\lambda^4}$. The thickness has been fitted to 550.7 nm with an MSE of 19.73. The optical constants (n, k) calculated using the model fit is shown in Fig. 4.12. The refractive index is extrapolated linearly into mid-IR since the wavelength range of the ellipsometer extends only up to 1700 nm.

The refractive index of SiO_2 decays from 1.52 toward 1.45 in the visible to the near-IR region, which is consistent with the literature [42]. In the mid-IR, the decay of the refractive index becomes almost negligible, as is shown by the extrapolated refractive index in Fig. 4.12, also supported by the values reported in the literature [43].

The extinction coefficient of SiO_2 is well known to be close to zero in the mid-IR [43]. The absorbing peaks that are shown in Fig. 4.12 are similar to the spectrum of water, which might be a sign of water contained in the oxide, that possibly originates from the humidity during layer deposition. Since the wavelength range that we are interested in (3 µm to 5 µm) is free from water absorption, assuming zero extinction coefficient is acceptable.

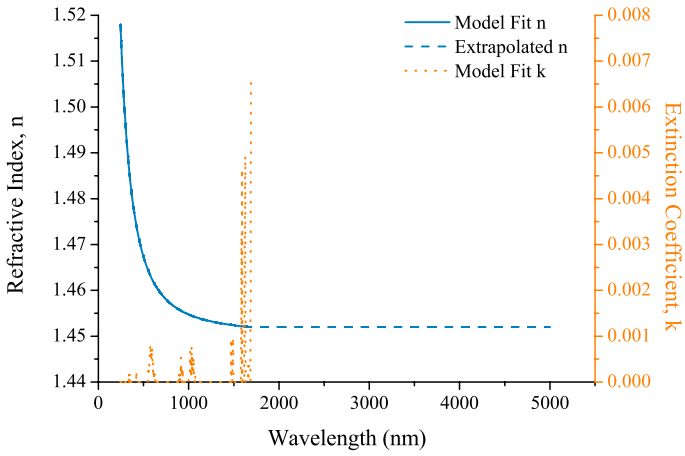

Figure 4.12: Refractive index and extinction coefficient of SiO_2 film modeled using ellipsometer measurements.

The thickness distribution map of the sputtered SiO_2 layer is measured using the same ellipsometer. The 2" wafer is divided into 21 sections and a mean thickness of 549.63 nm is calculated as shown in Fig. 4.13. The difference between the maximum and the minimum thickness is 7.72 nm, which corresponds to less than 1.5% thickness change over the entire wafer.

Previous fabrication runs indicated that the optical properties of our sputtered Si are very similar to amorphous Si [44]. A general oscillator layer of type Psemi-MO is first fitted to the optical properties of amorphous silicon. Then, the measured data is fitted to this model by adjusting the oscillator parameters as well as the thickness values. Native oxide layers have been added on the wafer and on the sputtered Si in the model. The measured Ψ and Δ is fitted with an MSE of 14.37 at incidence angles of 45°, 55° and 65° as shown in Fig. 4.14.

The refractive index and extinction coefficient of a 229.2 nm thick Si layer are shown in Fig. 4.15. As in amorphous Si, the refractive index has a peak in the visible range and later decays slowly in the near- and mid-IR [45, 46]. The extinction coefficient exhibits a similar behavior, it decreases down to negligible levels at around near-IR and remains practically zero in the mid-IR.

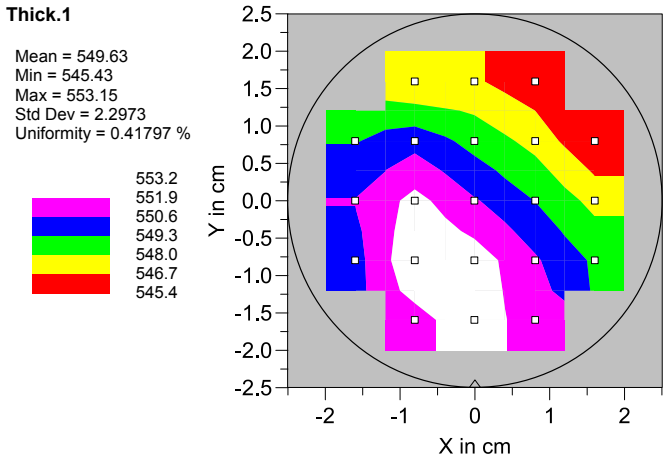

Figure 4.13: Measured distribution of the sputtered SiO_2 layer thickness over the wafer. The thickness values are in nm.

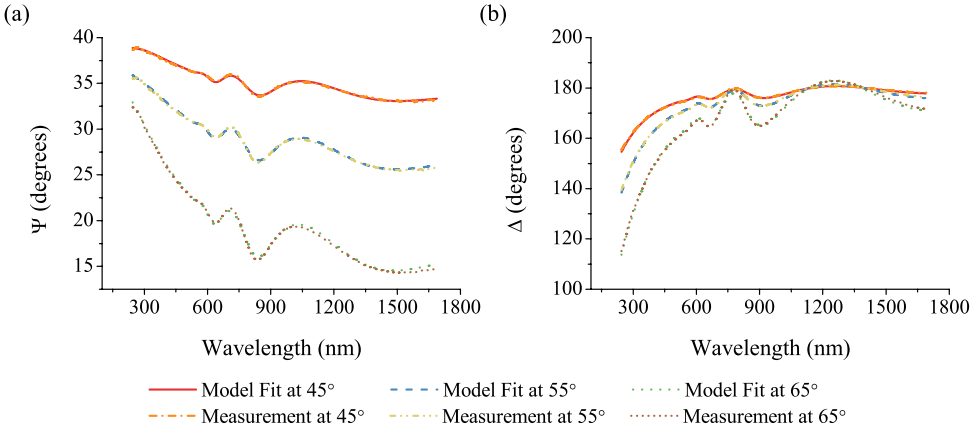

Figure 4.14: Measured (a) Ψ and (b) Δ spectra of the Si film compared to the model fit at various incidence angles.

The thickness distribution map of the sputtered Si layer is measured using the same procedure used for the SiO_2 layer. The 2" wafer is divided into 21 sections. An average thickness of 231.64 nm is calculated as shown in Fig. 4.16. The difference between the maximum and the minimum thickness is 10.9 nm, which corresponds to approximately 4.7% thickness change over the entire wafer.

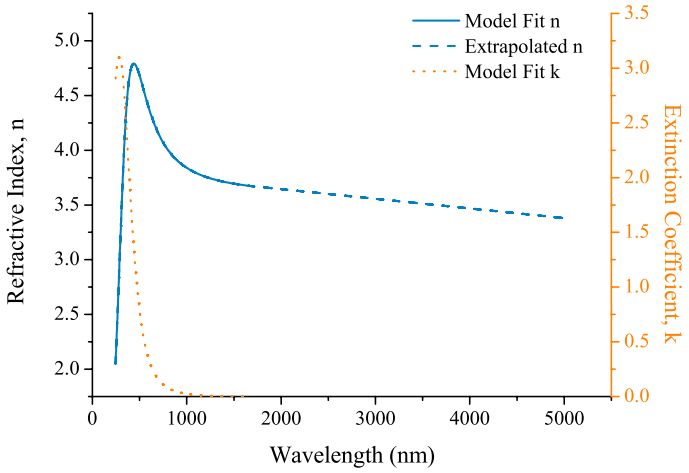

Figure 4.15: Refractive index and extinction coefficient of the Si film modeled using ellipsometer measurements.

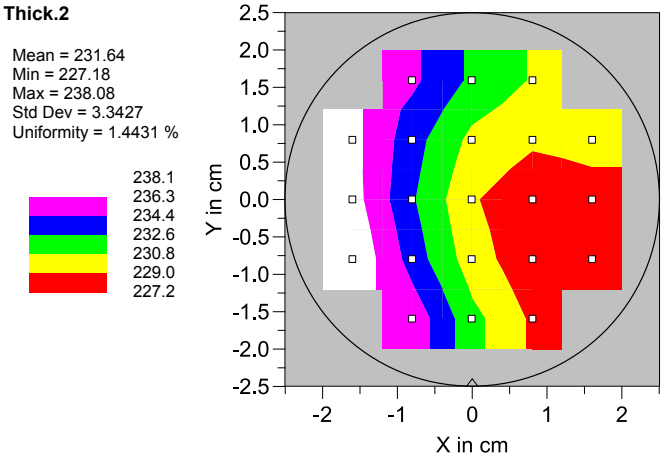

Figure 4.16: Measured distribution of the sputtered Si layer thickness over the wafer. The thickness values are in nm.

4.3.3. BRAGG MIRROR DESIGN

Quarter-wave Bragg mirrors are well known to provide a reflectivity that is comparable to the high values in metallic coatings. With the right choice of non-absorbing materials they can be used in transmissive optical filters. Bragg mirrors are composed of alternate layers of high and low refractive index materials with quarter wavelength optical thickness. The constructive interference of the reflected beams, i.e. high reflectivity, occurs due to the following rules:

(i) the reflected waves undergo π phase shift when traveling from low to high index medium and no phase shift occurs when they travel from a high to a low index medium, so that the continuity of boundary conditions for the electromagnetic field vectors are maintained

(ii) a phase change of π is equivalent to shifting a wave by half a wavelength

The reflections from a 4-layer quarter-wave stack with the associated phases are shown in Fig. 4.17. For an initial phase of δ, all the reflected waves experience an equivalent phase shift of π and interfere constructively if the optical thickness of the layers are a quarter of the wavelength. Obviously, the same effect applies for layers with a thickness equal to five quarters of the wavelength. Constructive interference occurs if the phase difference between the waves is an integer multiple of the wavelength (i.e. $\delta_2 - \delta_1 = m\lambda$). Therefore, increasing the layer thickness is equivalent to a higher order of interference. Similar to the FSR in filter design, high order of operation in a dielectric mirror results in a limited operating wavelength range with undesired side peaks.

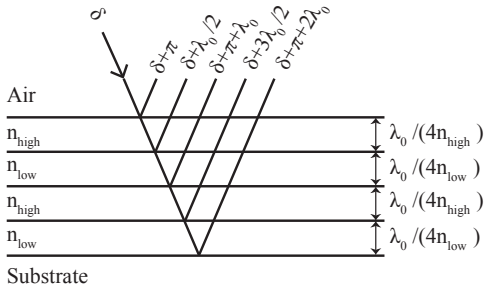

Figure 4.17: A 4-layer quarter-wave stack.

The effect of number of thin-film pairs and refractive index contrast on Bragg mirror reflectivity is studied using the transfer-matrix method. The low and high refractive index materials are selected as SiO_2 and Si respectively, while the layer thicknesses are calculated according to the reference wavelength of 3300 nm. As shown in Fig. 4.18(a),

increasing the number of thin-film pairs in a Bragg mirror increases the reflectivity, while limiting the operating bandwidth. The effect of refractive index contrast is analyzed by assuming SiO_2 as the low-index material and calculating the high-index for contrast ratios 2, 3 and 4. As given in Fig. 4.18(b), a high refractive index contrast between the mirror materials improves both reflectivity and operating bandwidth.

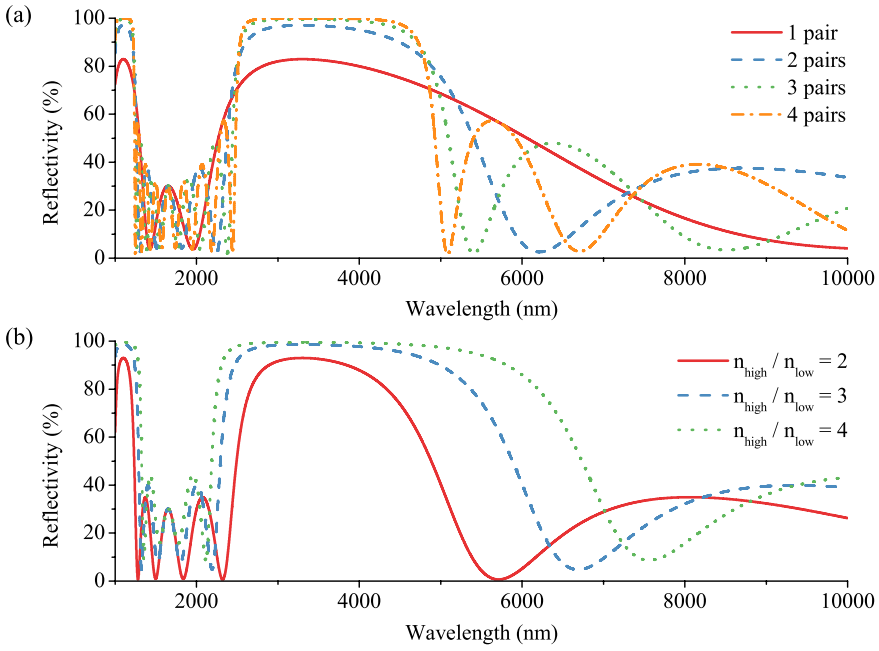

Figure 4.18: (a) The effect of number of thin-film pairs and (b) refractive index contrast on reflectivity in a Bragg mirror. The reference wavelength used in layer thickness calculation is 3300 nm.

The reflection and transmission coefficients used for calculating the reflectivity of the Bragg mirrors and eventually the transmittance of an FP filter are identical for the top and the bottom mirror, due to its flat structure as shown in Fig. 4.19(a). To assure wideband operation in an LVOF, the resonator cavity must be tapered. This can be achieved by combining a flat mirror either with a tilted flat mirror or with a tapered mirror. Due to the challenges in the fabrication of a tilted mirror, we selected the latter and fabricated a tapered Bragg mirror by tapering the first SiO_2 layer. Since the thickness of this SiO_2 layer depends on the lateral position along the length of the filter, the optical properties of the tapered Bragg mirror requires more attention. Therefore, position dependent reflection ($r'_{tapered}$) and transmission ($t_{tapered}$) coefficients of the tapered mirror are combined with the constant reflection (r'_{flat}) and transmission (t'_{flat}) coefficients of the flat mirror to calculate the transmission through the linear variable optical filter as depicted in Fig. 4.19(b).

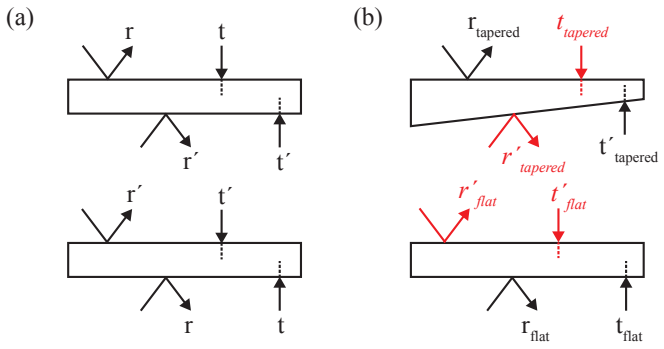

Figure 4.19: The reflection and transmission coefficients for (a) a Fabry-Perot filter and (b) an LVOF. The coefficients that are used for the calculating the transmission of an LVOF are shown in red.

To create the required cavity length along the filter varying from $h_1 = 24\,\mu m$ to $h_2 = 25.5\,\mu m$ as described in section 4.2, the level difference between the thickest and the thinnest part of the tapered SiO_2 layer must match the cavity length difference of merely $1.5\,\mu m$. The thickness of the tapered SiO_2 layer is thus selected to range from $d_2 = 960\,nm$ to $d_1 = 2460\,nm$ to align the maximum reflectivity to the reference wavelength of 3300 nm. The rest of the SiO_2 layers of the tapered mirror are $t_{SiO_2} = 569.97\,nm$ thick. The thickness of the Si layers used in both mirrors is $t_{Si} = 228.41\,nm$. The latter two were calculated using the reference wavelength of 3300 nm. The cross section of the device with related dimensions is shown in Fig. 4.20.

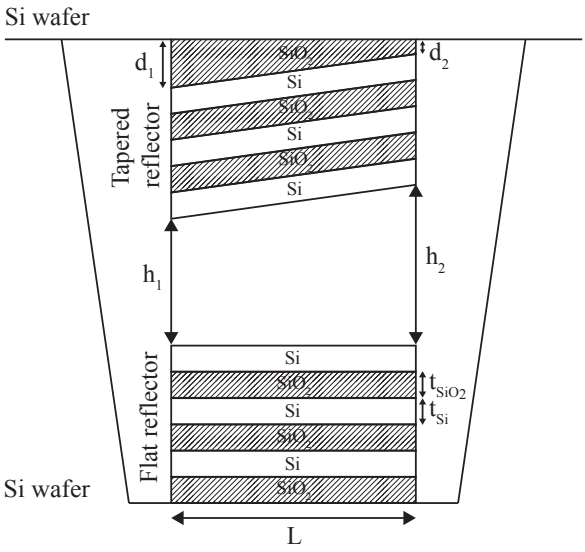

Figure 4.20: A schematic illustration showing the cross-section and layer stack of the LVOF.

The reflectivity and transmissivity values required to calculate the filter transmission are analyzed for both the FP filter and the LVOF assuming 3-pair Si/SiO_2 Bragg mirrors using Eq. 4.10.

$$\begin{aligned} R_{FP} &= \left|r' r'\right| \\ T_{FP} &= \left|t t'\right| \\ R_{LVOF} &= \left|r'_{flat} r'_{tapered}\right| \\ T_{LVOF} &= \left|t_{tapered} t'_{flat}\right| \end{aligned} \tag{4.10}$$

The effect of substrate coherence is taken into account by using phase matrices altered with equidistant phase factors in the transfer-matrix method as described in subsection 4.3.1. Moreover, the effect of polarization has been investigated for oblique incidence at $\theta' = 5°$. The simulated reflectivity and transmissivity of the FP filter and the LVOF are shown in Fig. 4.21.

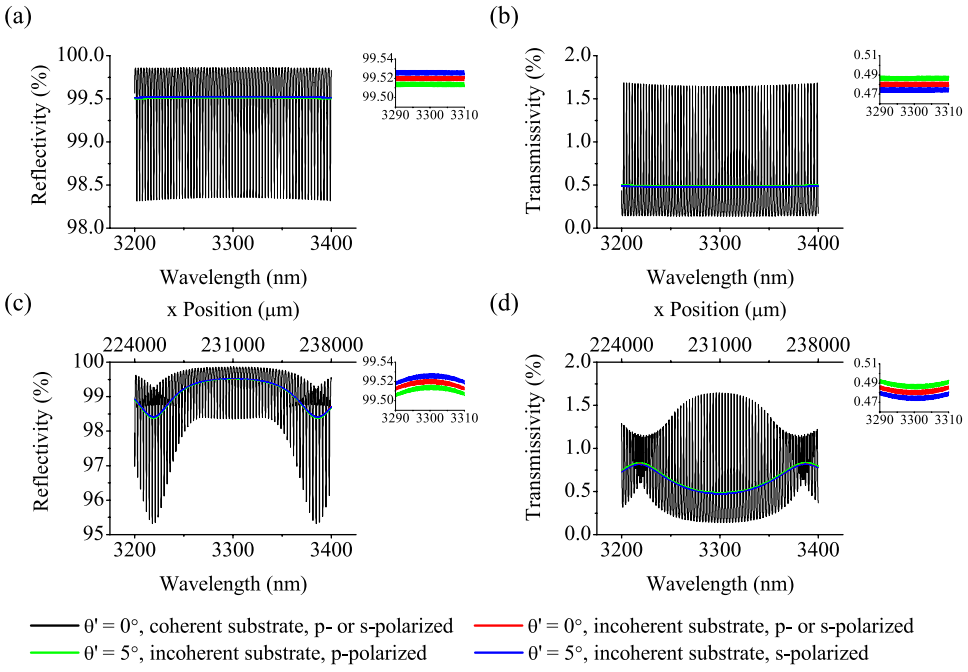

Figure 4.21: The reflectivity and transmissivity of the FP filter (a, b) and LVOF (c, d) in the 3.2 µm to 3.4 µm wavelength range.

The reflectivity and transmissivity of the FP filter is almost constant over the 3.2 µm to 3.4 µm wavelength range. There is a slight decrease in reflectivity and increase in transmissivity away from 3300 nm, since the physical thicknesses of the layers are calculated

according to the reference wavelength of 3300 nm. In contrast, the LVOF has a wavelength dependent reflectivity and transmissivity due to the tapered mirror. The difference between the maximum and the minimum reflectivity is approximately 1%. Such a small change in reflectivity might be negligible for many applications; however, it must be taken into account in LVOFs where highly reflective mirrors are required.

The dependency of reflectivity and transmissivity on polarization at oblique incidence is shown in the insets of Fig. 4.21 for both the FP filter and the LVOF. In both configurations, the change in reflectivity and transmissivity is less than 0.02%, thus can be disregarded.

4.4. OPTICAL SIMULATIONS

The transmission through an LVOF is calculated by incorporating the phase difference of the Fizeau interferometer calculated by Eq. 3.20 into Eq. 3.23 as described in the previous chapter. By using the reflectivity and the transmissivity values simulated above for the tapered and flat Bragg mirrors, the spectral response of an LVOF with a tapered mirror can be obtained.

In Eq. 3.23, the plane wave propagating through the filter was defined as $e^{i\delta_p}$, where the effect of the absorbing sample was neglected. The attenuation of a wave in amplitude can be calculated by multiplying the initial amplitude by the exponential $e^{-\gamma z}$, where γ is the evaluated absorption coefficient per unit optical path length and z is the distance that the wave travels. In our application, the evaluated absorption coefficient is that of the gas sample that fills the cavity and the distance is the optical path difference. Therefore, to calculate the effect of an absorbing medium in the cavity, the exponential part of Eq. 3.23 must be replaced with Eq. 4.11.

$$e^{i\delta_p} e^{-\gamma \Delta S_p} = e^{\left(i-\gamma \frac{\lambda}{2\pi}\right)\delta_p} \tag{4.11}$$

The transmission of a 14 mm long LVOF in 3.2 µm to 3.4 µm wavelength range is numerically simulated with 2.5 nm steps. For the sake of readability, the transmission curves at every 10 nm are shown in Fig. 4.22(a). The spectral response is observed right after the filter ($z = 0$) and normal incidence is assumed ($\theta' = 0$). The x-axis shows the position along the length of the filter, which is the distance from the wedge apex. It should be noted that in a practical device, the wedge apex is imaginary and an offset is introduced to the x-position such that the resulting cavity length range covers the spectrum of interest. For a 14 mm long filter with $h_1 = 24$ µm and $h_2 = 25.5$ µm, the desired transmission peaks lie in the 224 mm to 238 mm range, away from the cavity wedge apex. Each transmission curve corresponds to a wavelength starting with 3.2 µm at 224 mm and ending with 3.4 µm at 238 mm. The average full-width-half-max (FWHM) resolution

of the curves is 1.55 nm, which translates into wavenumbers as 1.42 cm^{-1}. The same simulation is run for methane in the cavity, where the evaluated absorption coefficient of methane is extracted from the HITRAN database by convolving a Gaussian profile with 1.42 cm^{-1} resolution with the broadened database. Then these values are used as attenuation factors defined by Eq. 4.11. The effect of methane can be observed with a decrease in the peak transmittance as shown in Fig. 4.22(b). The most significant drop is in the peak at 3320 nm located at 232.4 mm, where the absorption of methane is the strongest. The transmittance of methane is then calculated by taking the ratio of the filter response with methane in the cavity to the filter response without the gas as shown in Fig. 4.22(c).

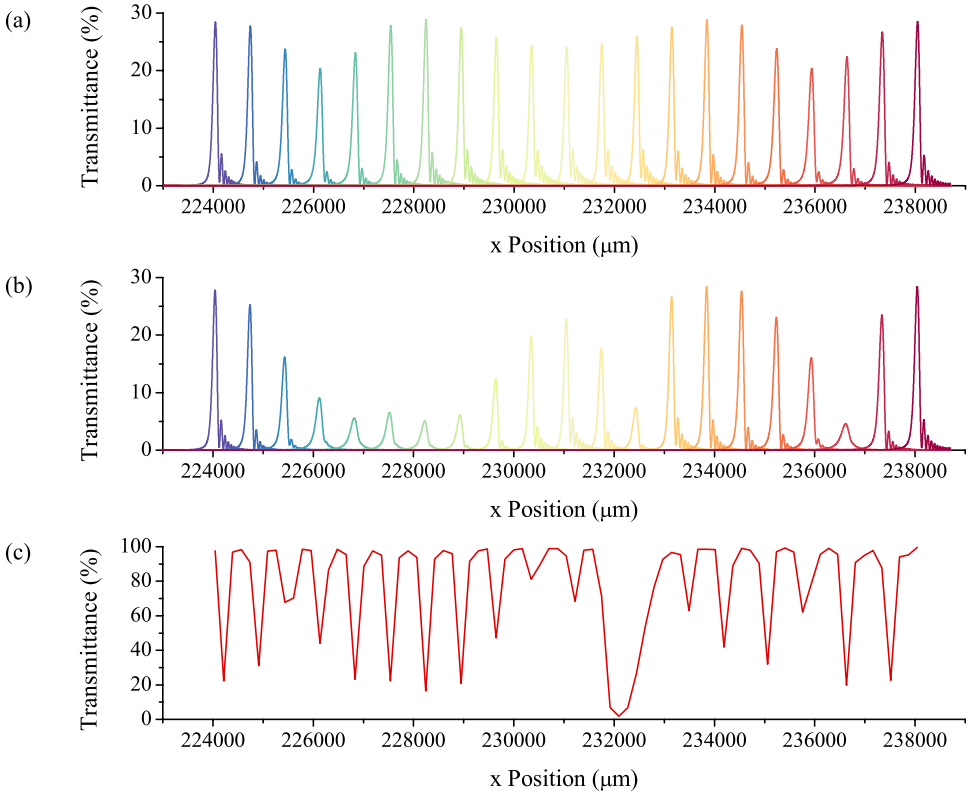

Figure 4.22: Transmission response of (a) the linear variable filter without gas, (b) the linear variable filter with methane in the cavity, and (c) methane alone at normal incidence ($\theta' = 0$) observed right after the filter ($z = 0$).

The OPL can be defined as the geometric length of the path that the light beam follows through the sample. The relation between the OPL and the absorption coefficient is rather straightforward in spectrometers with external sample cells with previ-

ously known dimensions. First a reference measurement is done to retrieve the spectral response of the filter only (T_{filter}), then the sample cell is filled with the sample and another measurement is run to obtain the combined effect of the filter and the sample ($T_{filter+sample}$). To extract the effect of the sample, the ratio of these two measurements is taken and the already known OPL of the sample cell is introduced in the equation as shown in Eq. 4.12. This gives the wavelength-dependent absorption coefficient of the sample, which enables quantitative identification through comparison with a material database.

$$T_{sample} = \frac{T_{filter+sample}}{T_{filter}} = \frac{T^2 \left| \sum_{p=1}^{\infty} R^{(p-1)} e^{i\delta_p} \right|^2 e^{-\gamma OPL}}{T^2 \left| \sum_{p=1}^{\infty} R^{(p-1)} e^{i\delta_p} \right|^2} = e^{-\gamma OPL} \tag{4.12}$$

When the cavity of an LVOF is used as a gas cell, extracting the absorption coefficient of a sample is not trivial. The measured transmission of the sample as given in Eq. 4.13 cannot be simplified further and hence cannot be linearly correlated to a fixed OPL value. In other words, the exponential attenuation in the equation depends on the phase difference between the reflected waves (δ_p) and cannot be taken out of the summation. Also, the optical path difference between the first and the pth transmitted wave, i.e. ΔS_p, which goes to infinity in theory, cannot be employed as the OPL value, since after a number of reflections the waves do not contribute to the interference pattern anymore.

$$T_{sample} = \frac{T_{filter+sample}}{T_{filter}} = \frac{T^2 \left| \sum_{p=1}^{\infty} R^{(p-1)} e^{\left(i - \gamma \frac{\lambda}{2\pi}\right)\delta_p} \right|^2}{T^2 \left| \sum_{p=1}^{\infty} R^{(p-1)} e^{i\delta_p} \right|^2} \tag{4.13}$$

The transmission of the device described above is further investigated at 3.3 µm wavelength, both with and without the absorbing medium in the cavity. The transmittance at the x-position of 231 mm is simulated and for each wave that passes through the filter, the transmittance is recorded. The number of transmitted waves is denoted by p, while the number of reflections inside the cavity is $2p-2$. The calculated transmittance values are shown in Fig. 4.23 for both high ($R = 0.985$) and medium ($R = 0.95$) reflectivity.

At high reflectivity, the filter transmittance reaches the steady state after approximately 600 reflections. When the absorbing sample with $\gamma = 0.2\,\mathrm{mm}^{-1}$ is inserted inside the cavity, the number of reflections required to reach the steady state decreases to 300. As the evaluated absorption coefficient goes even higher, less than 200 reflections are sufficient to come to a steady state in transmittance. As evident from the discussions in chapter 3, the transmittance values are higher in the simulations with medium reflectiv-

ity, compared to the simulations with high reflectivity. When mirrors with medium reflectivity are employed, the number of reflections required to reach the steady state are all below 200 and decreasing further as the evaluated absorption coefficient becomes higher.

Two important conclusions can be drawn from Fig. 4.23. Firstly, the higher the reflectivity of the mirrors, the higher the number of reflections; hence, the longer the effective optical path is. This makes the device more sensitive to low concentrations of the gas. A visual proof would be the spacing of the curves in Fig. 4.23(a) and 4.23(b). Since a lower concentration is equivalent to a lower evaluated absorption coefficient, the device would be able to sense lower concentrations if the spacing between the transmission curve without gas and the transmission curve with $\gamma = 0.2\,\mathrm{mm}^{-1}$ is wider. Comparing Fig. 4.23(a) and 4.23(b), one can conclude that the filter with highly reflective mirrors has a longer effective optical path and is more sensitive. Secondly, a short effective optical path does not necessarily mean that the filter is not serving its purpose. It means that there is either a very high absorption peak at that wavelength or the concentration of the sample is very high. The important aspect is the transmission distribution rather than the effective optical path length. Figure 4.23(a) shows that the filter is capable of sensing high absorption, while maintaining the sensitivity for lower concentrations.

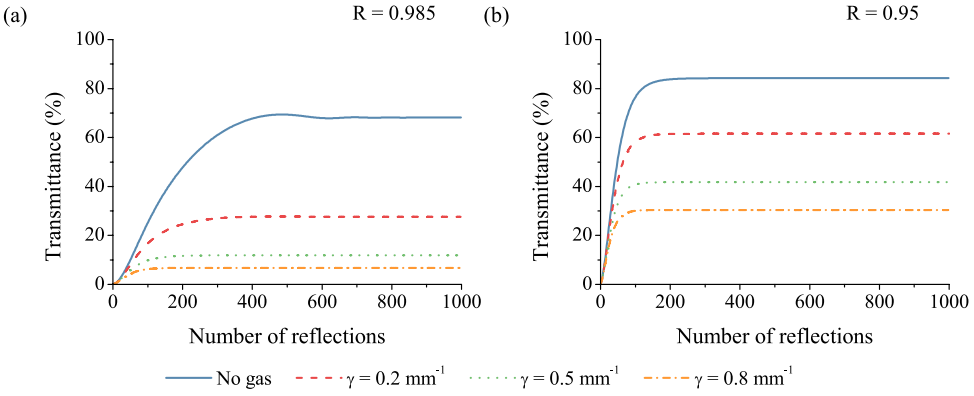

Figure 4.23: Transmittance calculated according to the number of reflections in the cavity of a 14 mm long device with a cavity taper angle of $\alpha = 6.1$ millidegree. The incidence angle is $\theta' = -1.61°$ and the spectral response is observed right after the filter. The transmittance belongs to 3.3 µm wavelength at an x-position of 231 mm corresponding to the 15^{th} order of interference.

The effect of absorption coefficient on OPL is investigated by simulating the spectral response of the LVOF for various absorption coefficients that are kept constant throughout the spectrum. After taking the ratio of the peak transmittance values, OPL is calculated using the known absorption coefficients. As shown in Fig. 4.24(a), the OPL decreases with increasing absorption coefficient. The change in OPL at absorption coeffi-

cients at the cm^{-1} level is negligible, while an absorption coeffient at the mm^{-1} level results in a sharper decrease in the OPL. Moreover, the combined effect of position-dependent reflectivity and cavity length results in a position-dependent path length.

Comparing the transmission response of methane to the database is not trivial, due to the position and absorption coefficient dependency of OPL. Hence, modifying the methane spectrum acquired from the database with a constant optical path length will not match the calculated transmission response of the linear variable filter. In a reverse manner, the elongated OPL can be calculated using the transmission response of methane and the wavelength dependent absorption coefficients. As shown in Fig. 4.24(b) the actual OPL varies from 2.8 mm to 6.5 mm, depending on the position on the filter. The effect of the cavity length can be eliminated by dividing the OPL to the cavity length at every position. Therefore, an elongation factor is achieved as shown in the right y-axis of Fig. 4.24(b). Both OPL and elongation plots show that the improvement is highly dependent on the mirror reflectivity due to the strong resemblance between the Bragg mirror reflectivity shown in Fig. 4.21 and Fig. 4.24(b). It should be noted that the irregularities in the OPL curve in Fig. 4.24(b) arise from the absorption coefficient dependency of the OPL. For instance, the dip at 232 mm corresponds to a major absorption peak in the spectrum of methane; hence the higher the absorption coefficient the shorter OPL is.

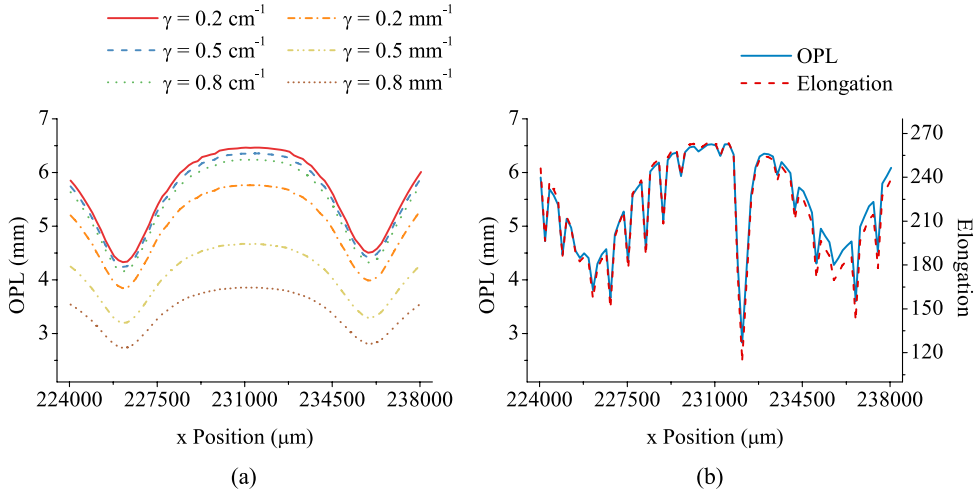

Figure 4.24: The calculated optical path length (OPL) of the linear variable filter using (a) constant absorption coefficients and (b) the evaluated absorption coefficient of methane.

In chapter 3, it was shown that the spectral response of an LVOF is highly dependent on the incidence angle of the input light beam and the filter-detector separation if the filter has highly reflective mirrors and is operating at a high order. At every detector

plane, there is an optimum incidence angle, which results in the narrowest transmission curves with the highest transmittance. However, due to the position dependency of the reflectivity, the optimum incidence angle is slightly different at different wavelengths along the length of the filter. To find the optimum value, the incidence angle was swept from −2° to −1.4° by 40 millidegree steps in the 3.2 µm to 3.4 µm wavelength range. The optimum incidence angle calculated for 21 different wavelength values are plotted in Fig. 4.25. Due to the change in reflectivity and transmissivity along the filter length, the optimum incidence angle fluctuates between −1.38° and −1.83°.

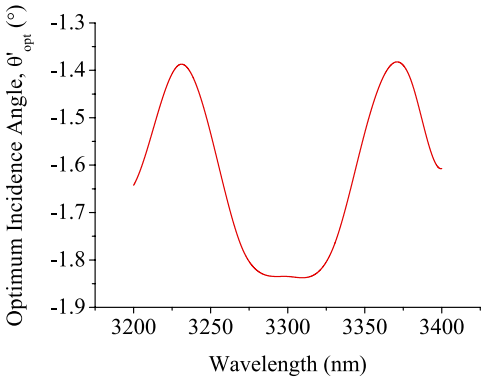

Figure 4.25: The optimum incidence angle.

In the final device, the wideband light can impinge on the device at only one incidence angle. Therefore, the optimum incidence angle is averaged to optimize the performance of the device in the given wavelength range. Then, the averaged optimum incidence angle, $\theta'_{opt,avg} = -1.61°$ is used for calculating the average FWHM resolution of the transmission curves. Subsequently, the average FWHM resolution, 0.92 nm or equivalently 0.84 cm^{-1}, is used as the resolution of the Gaussian profile to calculate the evaluated absorption coefficient of methane. As shown in Fig. 4.26, the absorption curves of methane are sharper and stronger at the optimum incidence angle. Therefore, a more detailed spectrum of the sample can be extracted if the filter is illuminated at the optimum incidence angle rather than at normal incidence.

To see the effect of the incidence angle on the spectral response of the filter, the same design has been simulated at $\theta' = -1.61°$ using the evaluated absorption coefficient of methane with 0.84 cm^{-1} FWHM resolution. The detector plane is right after the filter, i.e. $z = 0$. The results are shown in Fig. 4.27. Compared to Fig. 4.22, the transmission curves are narrower with higher transmittance. Moreover, the absorption of methane is higher as is evident from the difference between Fig. 4.22(c) and Fig. 4.27(c).

The increase in the absorption of methane at the optimum incidence angle can be

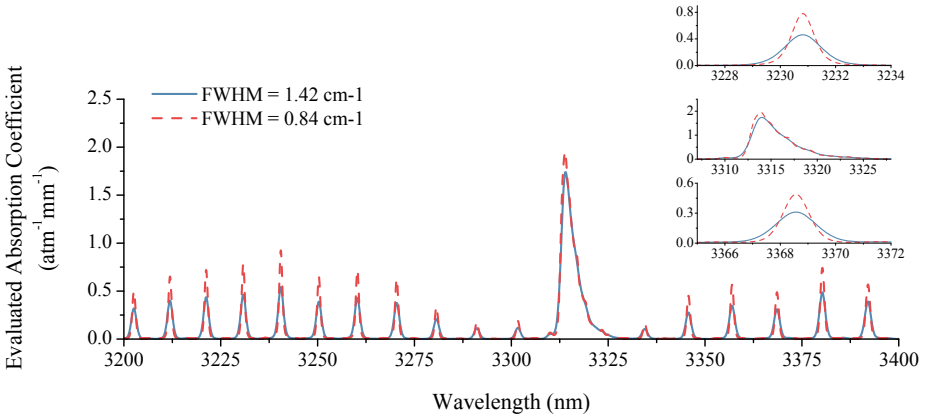

Figure 4.26: The evaluated absorption coefficient of methane calculated by convolving the HITRAN database with a Gaussian function at a FWHM resolution of 1.42 cm^{-1} and 0.84 cm^{-1}. The insets show expanded curves at various parts of the spectrum.

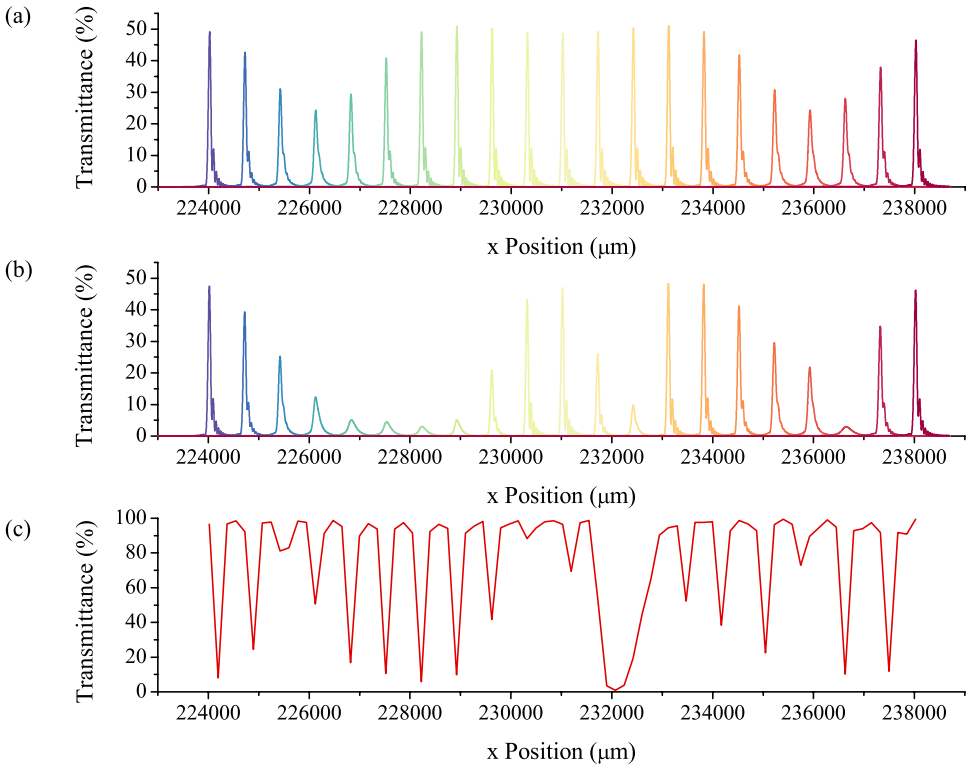

Figure 4.27: Transmission response of (a) the linear variable filter without gas, (b) the linear variable filter with methane in the cavity, and (c) methane alone at the optimum incidence angle of $\theta'_{opt} = -1.61°$ observed right after the filter ($z = 0$).

caused by either the higher evaluated absorption coefficient due to better resolution, or a longer OPL or the combination of the two. To see the effect of the incidence angle on the OPL, constant absorption coefficients of 0.2 mm^{-1}, 0.5 mm^{-1} and 0.8 mm^{-1} have been applied. As shown in Fig. 4.28(a), the effective OPL is still dominated by the reflectivity of the mirrors. However, the values are higher compared to the normal incidence case as was shown in Fig. 4.24(a). Furthermore, a similar comparison between Fig. 4.28(b) and 4.24(b) demonstrates the increase in the effective OPL and the corresponding elongation factor, when the actual evaluated absorption coefficient of methane is used. Therefore, by making use of the optimum incidence angle, the effective OPL can be increased in addition to improving the resolving power of the device.

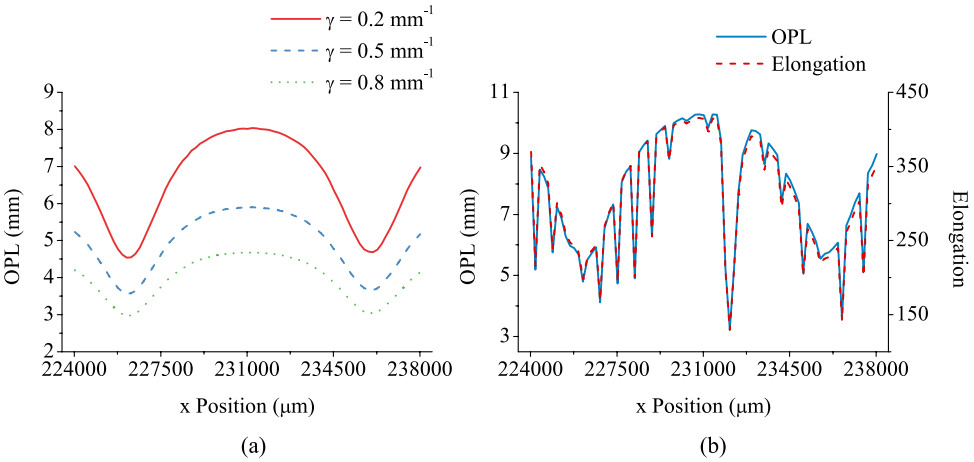

Figure 4.28: The calculated optical path length (OPL) of the linear variable filter using (a) constant absorption coefficients and (b) the evaluated absorption coefficient of methane at the optimum incidence angle of $\theta'_{opt} = -1.61°$ observed right after the filter ($z = 0$).

The absorption coefficient dependency of the OPL makes the spectral analysis of a gas filled LVOF more complex as compared to a spectrometer with an external sample holder. Together with the sample concentration, the analysis of a one-wavelength transmission measurement results in several combinations of absorption coefficient, concentration and OPL. The wideband operation of the device is the key factor in the analysis here. By putting together the spectral data measured over the operating wavelength range and using multivariate analysis methods, the composition of the sample can be extracted. It must be noted that the filter properties, such as mirror reflectivity and cavity length, must be known prior to the calculations.

REFERENCES

[1] Y. Shen, A. Davies, E. Linfield, P. Taday, D. Arnone, and T. Elsey, *Determination of glucose concentration in whole blood using Fourier-transform infrared spectroscopy,* Journal of Biological Physics **29**, 129 (2003).

[2] Y. C. Shen, A. G. Davies, E. H. Linfield, T. S. Elsey, P. F. Taday, and D. D. Arnone, *The use of Fourier-transform infrared spectroscopy for the quantitative determination of glucose concentration in whole blood,* Physics in Medicine and Biology **48**, 2023 (2003).

[3] C. Krafft, G. Steiner, C. Beleites, and R. Salzer, *Disease recognition by infrared and Raman spectroscopy,* Journal of Biophotonics **2**, 13 (2009).

[4] V. Erukhimovitch, M. Talyshinsky, Y. Souprun, and M. Huleihel, *FTIR spectroscopy examination of leukemia patients plasma,* Vibrational Spectroscopy **40**, 40 (2006).

[5] M. A. Mackanos and C. H. Contag, *FTIR microspectroscopy for improved prostate cancer diagnosis,* Trends in Biotechnology **27**, 661 (2009).

[6] N. J. Crane, E. G. Bartick, R. S. Perlman, and S. Huffman, *Infrared spectroscopic imaging for noninvasive detection of latent fingerprints,* Journal of Forensic Sciences **52**, 48 (2007).

[7] R. J. Cox, H. L. Peterson, J. Young, C. Cusik, and E. O. Espinoza, *The forensic analysis of soil organic by FTIR,* Forensic Science International **108**, 107 (2000).

[8] F. R. van de Voort, J. Sedman, and A. A. Ismail, *A rapid FTIR quality-control method for determining fat and moisture in high-fat products,* Food Chemistry **48**, 213 (1993).

[9] D. W. Lachenmeier, *Rapid quality control of spirit drinks and beer using multivariate data analysis of Fourier transform infrared spectra,* Food Chemistry **101**, 825 (2007).

[10] H. W. Siesler, *Fourier transform infrared (FTIR) spectroscopy in polymer research,* Journal of Molecular Structure **59**, 15 (1980).

[11] A.-M. Olsson and L. Salmén, *The association of water to cellulose and hemicellulose in paper examined by FTIR spectroscopy,* Carbohydrate Research **339**, 813 (2004).

[12] M. Schneider, P. Romero, F. Hase, T. Blumenstock, E. Cuevas, and R. Ramos, *Continuous quality assessment of atmospheric water vapour measurement techniques: FTIR, Cimel, MFRSR, GPS, and Vaisala RS92,* Atmospheric Measurement Techniques **3**, 323 (2010).

[13] J. R. Gosz, C. N. Dahm, and P. G. Risser, *Long-path FTIR measurement of atmospheric trace gas concentrations,* Ecology **69**, 1326 (1988).

[14] H. Kobayashi, A. Shimota, C. Yoshigahara, I. Yoshida, Y. Uehara, and K. Kondo, *Satellite-borne high-resolution FTIR for lower atmosphere sounding and its evaluation,* IEEE Transactions on Geoscience and Remote Sensing **37**, 1496 (1999).

[15] B. Stuart, *Infrared Spectroscopy: Fundamentals and Applications* (Wiley, 2004).

[16] P. R. Griffiths and J. A. De Haseth, *Fourier Transform Infrared Spectrometry*, Vol. 171 (John Wiley & Sons, 2007).

[17] M. Kraft, A. Kenda, T. Sandner, and H. Schenk, *MEMS-based compact FT-spectrometers - a platform for spectroscopic mid-infrared sensors,* in *IEEE Sensors* (2008) pp. 130–133.

[18] Y. M. Sabry, D. Khalil, and T. Bourouina, *Monolithic silicon-micromachined free-space optical interferometers onchip,* Laser & Photonics Reviews **9**, 1 (2015).

[19] O. Manzardo, R. Michaely, F. Schädelin, W. Noell, T. Overstolz, N. De Rooij, and H. P. Herzig, *Miniature lamellar grating interferometer based on silicon technology,* Optics Letters **29**, 1437 (2004).

[20] N. P. Ayerden, U. Aygun, S. T. S. Holmstrom, S. Olcer, B. Can, J.-L. Stehle, and H. Urey, *High-speed broadband FTIR system using MEMS,* Applied Optics **53**, 7267 (2014).

[21] Agilent Technologies, *4300 Handheld FTIR,* Accessed: 27.05.2016.

[22] Thermo Fisher Scientific, *TruDefender Handheld FTIR Spectrometer,* Accessed: 27.05.2016.

[23] J. P. Coates, *New microspectrometers: Building on the principle that simple is beautiful,* (2000).

[24] NIST Mass Spec Data Center and S. Stein, *Infrared spectra,* in *NIST Chemistry WebBook, NIST Standard Reference Database Number 69*, edited by P. Linstrom and W. Mallard (National Institute of Standards and Technology, Gaithersburg MD, 20899).

[25] S. W. Sharpe, T. J. Johnson, R. L. Sams, P. M. Chu, G. C. Rhoderick, and P. A. Johnson, *Gas-phase databases for quantitative infrared spectroscopy,* Applied Spectroscopy **58**, 1452 (2004).

[26] L. S. Rothman, I. E. Gordon, A. Barbe, D. C. Benner, P. F. Bernath, M. Birk, V. Boudon, L. R. Brown, A. Campargue, J. P. Champion, K. Chance, L. H. Coudert, V. Dana, V. M. Devi, S. Fally, J. M. Flaud, R. R. Gamache, A. Goldman, D. Jacquemart, I. Kleiner, N. Lacome, W. J. Lafferty, J. Y. Mandin, S. T. Massie, S. N. Mikhailenko, C. E. Miller, N. Moazzen-Ahmadi, O. V. Naumenko, A. V. Nikitin, J. Orphal, V. I. Perevalov, A. Perrin, A. Predoi-Cross, C. P. Rinsland, M. Rotger, M. Šimečková, M. A. H. Smith, K. Sung, S. A. Tashkun, J. Tennyson, R. A. Toth, A. C. Vandaele, and J. Vander Auwera, *The HITRAN 2008 molecular spectroscopic database,* Journal of Quantitative Spectroscopy and Radiative Transfer **110**, 533 (2009).

[27] E. V. Semiletova, Y. F. Arshinov, C. N. Mikhailenko, Y. L. Babikov, and V. F. Golovko, *Information-calculating system spectroscopy of atmospheric gases. The structure and main functions,* Atmospheric and Oceanic Optics **18**, 685 (2005).

[28] Z. Knittl, *Optics of Thin Films: An Optical Multilayer Theory* (Wiley London, 1976).

[29] P. Yeh, *Optical Waves in Layered Media*, Vol. 95 (Wiley New York, 1988).

[30] M. Born and E. Wolf, *Principles of Optics: Electromagnetic Theory of Propagation, Interference and Diffraction of Light*, 7th ed. (Cambridge University Press, 1999).

[31] E. Hecht, *Optics (4th Edition)* (Addison Wesley, 2001).

[32] P. W. Baumeister, *Optical Coating Technology* (SPIE Press, 2004).

[33] H. A. Macleod, *Thin-film Optical Filters* (CRC Press, 2010).

[34] C. C. Katsidis and D. I. Siapkas, *General transfer-matrix method for optical multilayer systems with coherent, partially coherent, and incoherent interference,* Applied Optics **41**, 3978 (2002).

[35] M. C. Troparevsky, A. S. Sabau, A. R. Lupini, and Z. Zhang, *Transfer-matrix formalism for the calculation of optical response in multilayer systems: from coherent to incoherent interference,* Optics Express **18**, 24715 (2010).

[36] R. Santbergen, A. H. M. Smets, and M. Zeman, *Optical model for multilayer structures with coherent, partly coherent and incoherent layers,* Optics Express **21**, A262 (2013).

[37] A. Mann, *Infrared Optics and Zoom Lenses* (SPIE Press, 2009).

[38] D. C. Harris, *Materials for Infrared Windows and Domes: Properties and Performance* (SPIE Press, 1999).

[39] S. Franssila, *Introduction to Microfabrication* (John Wiley & Sons, 2010).

[40] M. J. Madou, *Fundamentals of Microfabrication: The Science of Miniaturization* (CRC Press, 2002).

[41] H. G. Tompkins, *A User's Guide to Ellipsometry* (Academic Press, 2012).

[42] L. Gao, F. Lemarchand, and M. Lequime, *Refractive index determination of SiO_2 layer in the UV/Vis/NIR range: spectrophotometric reverse engineering on single and bi-layer designs,* Journal of the European Optical Society - Rapid publications **8** (2013).

[43] J. Kischkat, S. Peters, B. Gruska, M. Semtsiv, M. Chashnikova, M. Klinkmüller, O. Fedosenko, S. Machulik, A. Aleksandrova, G. Monastyrskyi, Y. Flores, and W. Ted Masselink, *Mid-infrared optical properties of thin films of aluminum oxide, titanium dioxide, silicon dioxide, aluminum nitride, and silicon nitride,* Applied Optics **51**, 6789 (2012).

[44] M. Ghaderi, N. P. Ayerden, A. Emadi, P. Enoksson, J. H. Correia, G. de Graaf, and R. F. Wolffenbuttel, *Design, fabrication and characterization of infrared LVOFs for measuring gas composition,* Journal of Micromechanics and Microengineering **24**, 084001 (2014).

[45] E. D. Palik, *Handbook of Optical Constants of Solids* (Elsevier, 1998).

[46] D. T. Pierce and W. E. Spicer, *Electronic structure of amorphous Si from photoemission and optical studies,* Physical Review B **5**, 3017 (1972).

5

DEVICE FABRICATION

THE increasing need for material identification in field applications calls for robust, reliable and low-cost microspectrometers. Thanks to the wafer-level batch fabrication, a microelectromechanical systems (MEMS) solution would make this possible, forcing the device to be miniaturized to the wafer-level. However, integrating the readout circuitry with the sensor at the wafer-level puts emphasis on the CMOS compatibility of the solution. Wafer bonding can be used to alleviate the compatibility constraints or to distribute microsystem complexity over more than one wafer. The latter argument is the reason why wafer bonding is used here.

A linear variable optical filter (LVOF) is a robust wavelength-selective MEMS device without any moving parts. The CMOS-compatible fabrication method using standard clean-room processes makes the LVOF highly suitable for building a robust and low-cost microspectrometer. Using the resonance cavity of an LVOF also as a gas cell (gas-filled LVOF), i.e. performing wavelength selection and absorption of light by the sample simultaneously allows for high reliability, low cost, wideband operation and a significant reduction in the size of MEMS-based spectrometers.

The fabrication of a gas-filled LVOF relies on manufacturing the flat and the tapered mirrors separately and subsequent wafer bonding as shown in Fig. 5.1. In this chapter, firstly, the fabrication flows of the flat and the tapered Bragg mirrors are explained. Then, the masks used in the fabrication of the device are described. After a discussion of the surface profile measurements, the chapter is finalized with a brief description of the device assembly through wafer bonding and subsequent inspection by a near-IR camera.

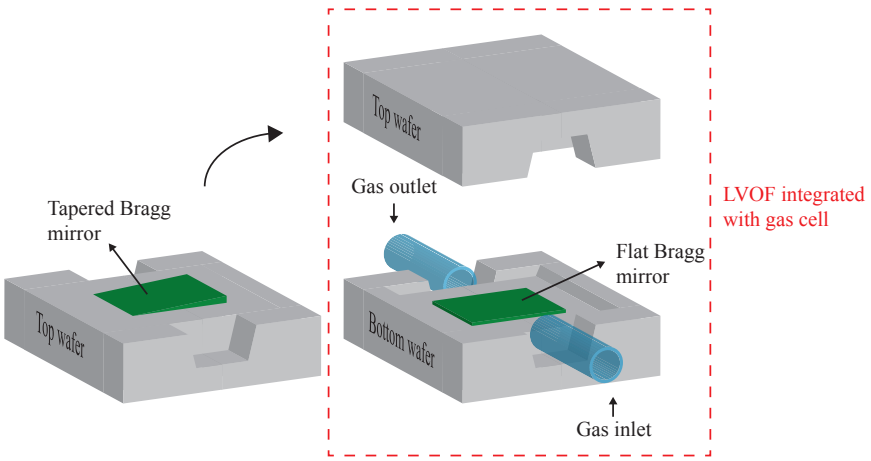

Figure 5.1: Schematic illustration of the device assembly.

5.1. FLAT BRAGG MIRROR

The fabrication of the flat Bragg mirror is based on opening a cavity, which forms the basis of the gas cell, by wet etching and subsequent mirror layer deposition. The fabrication steps of the flat reflector are shown in Fig. 5.2. Since the surface of the wafer must be very clean for wafer bonding, initially a 500 nm thick layer of thermal SiO_2 is grown on a bare wafer. Then, a 1 µm thick PECVD oxide is deposited for further protection. Subsequently, a 30 µm deep cavity is patterned by the cavity mask and opened by KOH etching. After that, the six alternate layers of Si and SiO_2 are sputtered without breaking the vacuum in the sputtering machine (FHR MS150, FHR Anlagenbau GmbH, Germany). Later, the mirror layers are patterned using the small cavity mask such that they only remain in the cavity. The layers on the frame and on the edges of the cavity are removed using RIE with CF_4, SF_6 and O_2 gases. Subsequently, 275 µm deep openings for gas inlet and outlet are etched using DRIE (Omega i2L Rapier, SPTS Technologies, USA). In the last step, the excess oxide layers on the frame are removed using BHF and the wafer goes through RCA1 cleaning followed by a Marangoni drying step for wafer bonding.

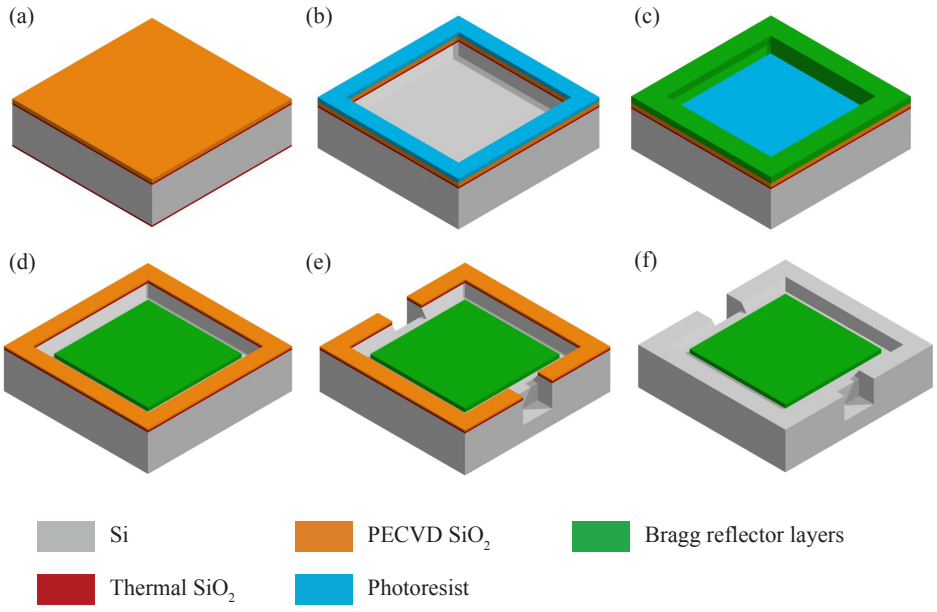

Figure 5.2: Fabrication steps of the flat Bragg mirror: (a) thermal and PECVD oxide deposition, (b) KOH etching of the cavity, (c) sputtering and patterning of the mirror, (d) plasma etching of the mirror layers on the frame, (e) DRIE for opening gas inlet and outlet, and (f) removing oxide on the frame and cleaning.

5.2. TAPERED BRAGG MIRROR

The tapered mirror is fabricated by tapering the first SiO_2 layer and then depositing the remaining quarter-wave thick layers on top. The key step of LVOF process is the fabrication of the vertically tapered SiO_2 layer with a small taper angle. Moreover, maintaining the same taper along the width of the layer is crucial to ensure sufficient light throughput.

Tapered MEMS structures are commonly used for coupling optical fibers to chips efficiently. These tapers are usually fabricated using a grayscale mask for patterning the resist and then transferring the tapered resist profile onto the substrate by dry etching [1, 2]. Despite the high cost of grayscale mask manufacturing, the limited taper length (< 1 mm) of these mode size converters allows for moderate resolution; hence, moderate cost. In contrast, the typical length of an LVOF (the taper length of the SiO_2 layer in this case) is higher (> 10 mm) to enable larger pixels in the detector array underneath, given the required number of filter channels. This necessitates an increased number of graytones in the mask for a smooth taper; thus, increasing the cost and the complexity of mask fabrication.

Another method used for taper fabrication is based on moving rectangular or trapezoidal masks in the deposition instrument. Detailed analysis of instrument operation and mask movement has been reported for mass production [3–5]. Moreover, Sheng *et al.* suggested the use of a triangular mask during the ion-beam etching of a flat thin film instead of using such a mask during deposition [6]. However, both methods require alteration in high-cost cleanroom instruments.

Emadi *et al.* developed a CMOS-compatible method for fabricating vertically tapered layers [7]. Similar to the method with grayscale mask, this method also relies on the fabrication of a tapered resist and subsequent transfer etching. However, the tapered resist profile is fabricated by low-cost methods using a conventional mask with linearly variable distanced trenches. The technique is based on the principle that the volume of a trench must be equal to the volume of the photoresist on both sides of the trench that must be removed to obtain the desired slope as shown in Fig. 5.3(a). After the resist is patterned with this mask as shown in Fig. 5.3(b), the wafer undergoes a thermal-chemical treatment to convert the resist layer with linearly variable distanced trenches to a smooth tapered structure. Then, this tapered resist layer is transferred to the underlying optical layer using one-to-one plasma etching.

Thermal reflow is based on heating the wafer coated with photoresist above the glass transition temperature, where the photoresist softens and the sharp edges/corners become round. However, the viscosity of the photoresist during thermal reflow is too high to achieve the required taper. Therefore, the thermal reflow is accompanied by chemical

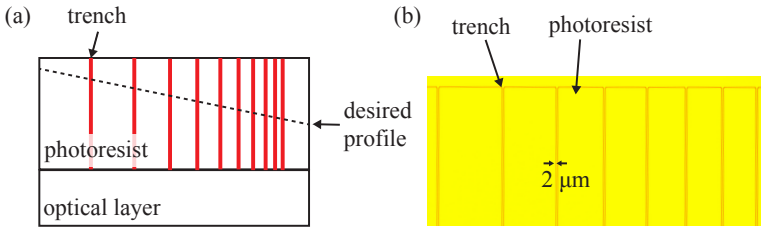

Figure 5.3: (a) Fabrication method for creating a tapered optical layer. (b) Microscope image of the photoresist after lithography and development.

reflow to decrease the viscosity of the resist. When the wafer is exposed to a solvent vapor, the resist absorbs the solvent and becomes less viscous. After the reflow, the wafer must be baked to remove the remaining solvent in the resist [8].

Negative photoresists are generally not suitable for reflow, since they cross-link after exposure and baking. The positive photoresist AZ9260 is selected for the reflow and has a glass transition temperature around 100 °C to 130 °C. Propylene glycol methyl ether acetate (PGMEA) is selected as the solvent, due to its compatibility with AZ-type photoresists in addition to its low vapor pressure and its suppression of particle formation in the resist layer. The solution prepared with PGMEA is heated up to 40 °C and the wafer with patterned resist is exposed to the vapor for 4 minutes as shown in Fig. 5.4. Subsequently, the wafer is baked on a hot plate at 100 °C for 2 minutes.

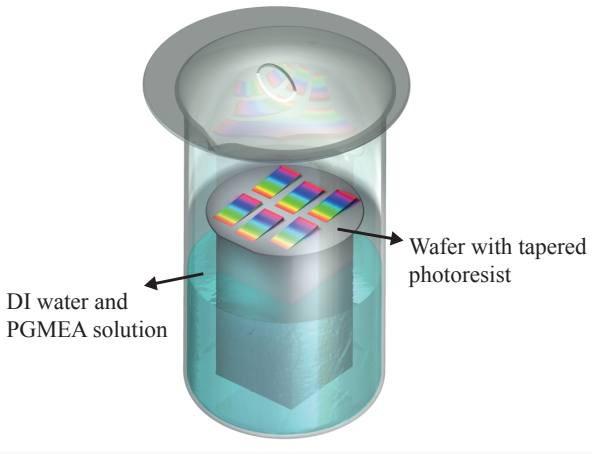

Figure 5.4: A schematic illustration of the reflow setup. The beaker is filled with the DI water and PGMEA solution. The wafer is placed on a holder inside the beaker such that the PGMEA vapor can reach the wafer surface. The beaker is placed on a temperature-controlled hot plate and the solution is kept at 40 °C.

The process steps for the fabrication of the tapered Bragg mirror are summarized in

Fig. 5.5. First, a 500 nm thick oxide layer is grown thermally for surface protection. Then, a 3 µm thick PECVD TEOS layer is deposited. Later, 6 µm thick AZ9260 positive photoresist is spin coated, patterned, and developed using the LVR mask, resulting in an array of trenches that are distanced in a linearly variable manner. A thermal-chemical treatment with PGMEA vapor at 40 °C transforms this layer into a smooth tapered structure. Subsequently, this layer is transferred to the TEOS layer underneath using plasma etching with the instrument Plasmalab System 100 (Oxford Instruments, Germany) with equal etch rate for resist and oxide. The recipe to achieve one-to-one transfer is based on a gas mixture of 2 sccm O_2, 9 sccm CF_4 and 77 sccm CHF_3 at 20 mTorr process pressure with 50 W power. The calculated etch rate for both the photoresist and SiO_2 is 15 nm/min.

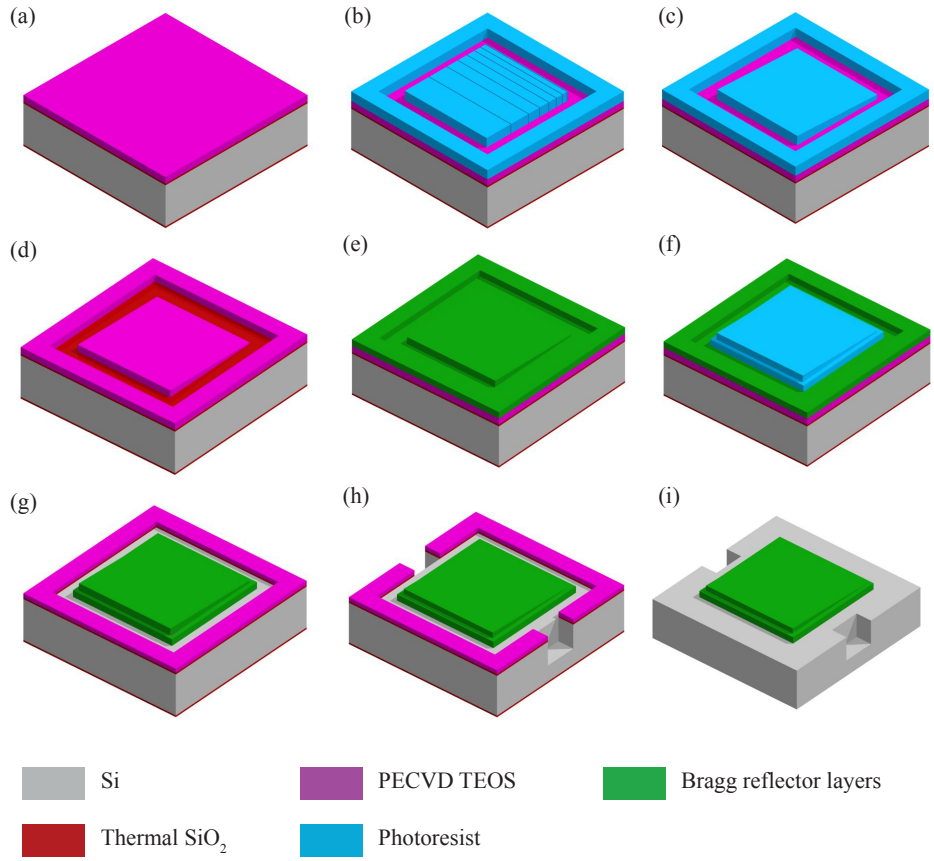

Figure 5.5: Fabrication steps of the tapered Bragg mirror: (a) thermal oxide and PECVD TEOS deposition, (b) photoresist patterning and development, (c) thermal-chemical treatment of the photoresist, (d) transfer etching of the tapered profile on the PECVD TEOS layer, (e) sputtering the remaining mirror layers, (f) removing excess mirror layers on the frame, (g) DRIE for opening gas inlet and outlet, and (h) removing oxide on the frame and cleaning.

The remainder of the fabrication steps for the tapered Bragg mirror are similar to those of the flat mirror. After the transfer etching of the tapered photoresist onto the SiO_2 layer, the remaining five layers of the mirror are sputtered. The excess mirror layers on the frame are removed by plasma etching after patterning by the small cavity mask. The 275 µm deep gas inlet and outlet are patterned by the pipe mask and etched by DRIE. Finally, the wafer goes through RCA1 cleaning and Marangoni drying for wafer bonding after the remaining oxide layers on the frame are removed by BHF.

5.3. MASK DESIGN

The gas-filled LVOF is fabricated in a 4-mask process. The combination of all these masks are shown in Fig. 5.6. The cavity mask is used in the fabrication of the flat mirror to etch the cavity, where the flat Bragg mirror layers are later deposited. The uppermost filter on the mask (LVR1) requires a cavity that is 32 mm wide and 12 mm tall. The cavities on the second row that consist of the short filters LVR2, LVR3 and LVR4 from the top to the bottom, are squares with a side length of 12 mm. The slightly larger cavities on the third row include the long filters LVR2-ver2, LVR3-ver2 and LVR4-ver2 from the top to the bottom. These cavities are also squares with a side length of 16 mm. The small cavities on the corners and on the fourth row are test structures with similar filters.

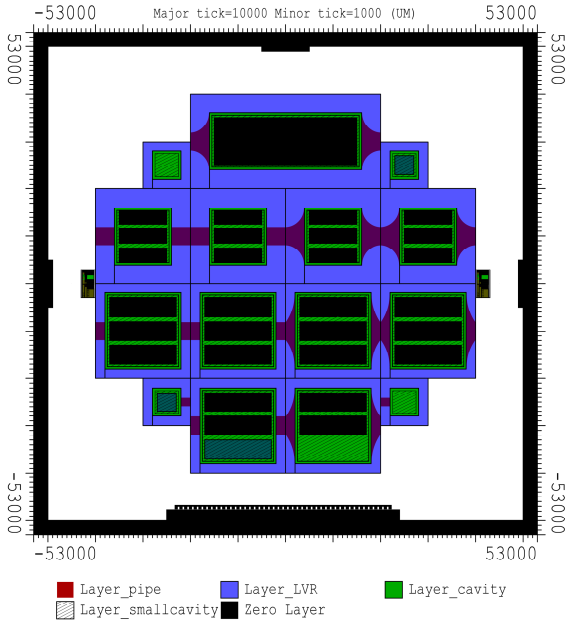

Figure 5.6: The combination of the masks for gas-filled LVOF fabrication.

The small cavity mask is used in the fabrication of both the flat and the tapered mirrors. It is employed in the removal of the sputtered Si and SiO_2 Bragg mirror layers from the frame and the edges of the cavity. The sides of the structures in this mask are 500 µm further inside the structures of the cavity mask. The pipe mask is composed of pipe-like structures to open deep cavities on the frame of the filter. These cavities serve as gas inlet and outlet after the wafer bonding. This mask is also used in the fabrication of both the flat and the tapered mirror wafers.

The linear variable reflector (LVR) mask is used for opening trenches with linearly varying distances. This mask is used to pattern a photoresist layer, which transforms into a tapered structure by a thermal-chemical treatment. Transfer etching of the tapered photoresist layer onto the underlying SiO_2 layer results in a tapered SiO_2 layer, which forms the basis of the tapered Bragg mirror.

The principle of the mask design to fabricate a tapered layer by the combination of thermal-chemical treatment of photoresist with subsequent transfer etching was previously explained in detail [9]. According to this principle, the volume of a trench (indicated with a pattern) must be equal to the volume of the photoresist on both sides of the trench that must be removed (shown in red) to obtain the desired slope (indicated with a dotted line) as shown in Fig. 5.7. This translates into Eq. 5.1, where w_t is the trench width and t_{PR} is the photoresist thickness. The parameters a and b define the size of the photoresist slab to be removed, while x_0 and x_1 defines the position of the slab along the length of the layer.

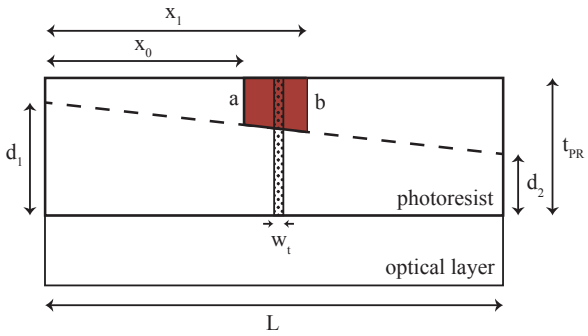

Figure 5.7: A schematic illustration of the principle of the mask design for fabricating a tapered layer.

$$w_t t_{PR} = \frac{(a+b)(x_1 - x_0)}{2} \tag{5.1}$$

The trench width is selected as $w_t = 2\mu m$ based on the minimum feature size that can be achieved with the contact aligner. The spacing between the trenches are calculated iteratively using the initial thickness of the photoresist (t_{PR}), the intended level

height at both ends of the tapered layer (d_1, d_2), the trench width (w_t) and the length of the layer (L). Previous fabrication runs show that the taper becomes slightly nonlinear closer to the edges and in some cases, undesired bumps start to appear at the corners as shown in Fig. 5.8. Therefore, the level difference calculated in Chapter 4 as 1.5 µm is extended above 2 µm.

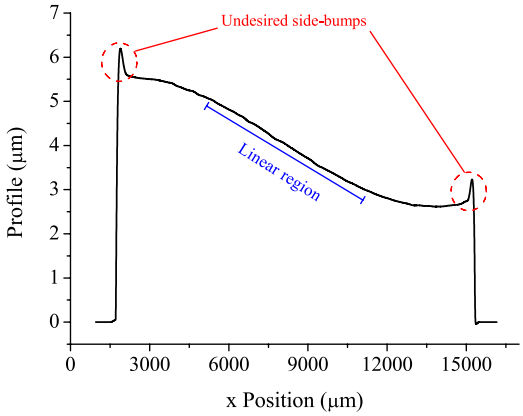

Figure 5.8: The measured profile of photoresist after thermal-chemical reflow.

A higher level difference, or equivalently taper angle, forces the trenches to be deeper to compensate for the increased volume of photoresist to be removed. Therefore, a thicker initial layer of photoresist is required to achieve the intended slope. The list of the devices with various lengths and level differences are summarized in Table 5.1. The initial photoresist thickness for all these devices is $t_{PR} = 6\,\mu m$.

Table 5.1: The tapered layer parameters used in the mask design.

Tapered mirror name	Level difference (nm)	Length (mm)	Width (mm)	Taper angle (millidegree)
LVR1	2900	30	10	5.54
LVR2	2900	10	3	16.61
LVR3	2500	10	3	14.32
LVR4	2000	10	3	11.46
LVR2-ver2	2900	14	4	11.87
LVR3-ver2	2500	14	4	10.23
LVR4-ver2	2000	14	4	8.18

5.4. SURFACE PROFILE MEASUREMENTS

The profiles of the various tapered SiO_2 layers listed in Table 5.1 are measured with a stylus profiler and the results are shown in Fig. 5.9. The measurement data has been

corrected for the thin-film stress induced curvature of the die on which the filter is fabricated. For this purpose, the thin-film-free parts on both sides of the tapered layer are used as a reference as shown in Fig. 5.10. A 3rd order polynomial is fitted to these parts to replicate the curvature over the entire layer. Then, the fitted curvature is subtracted from the measured profile, resulting in the plots given in Fig. 5.9.

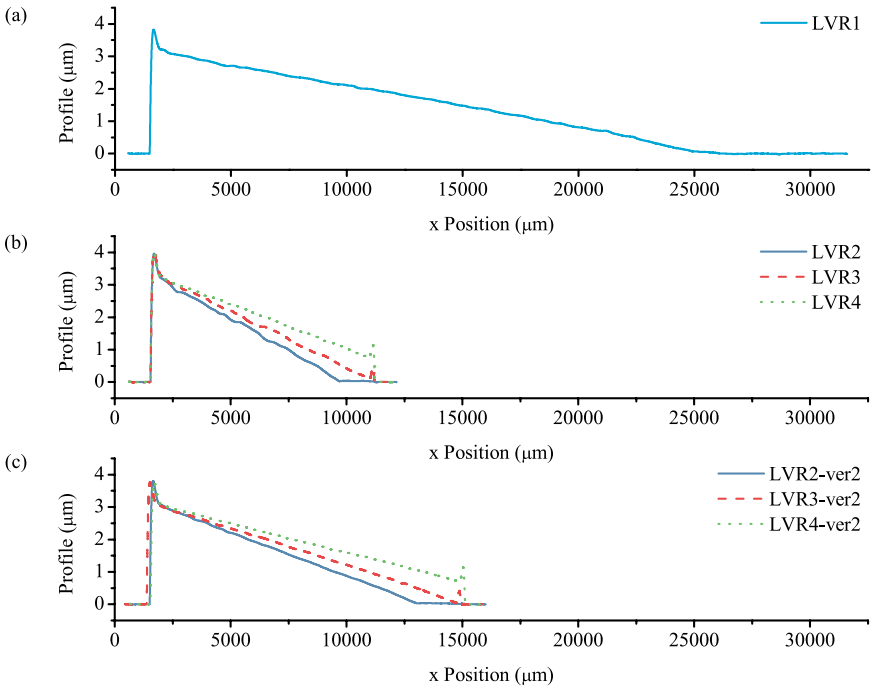

Figure 5.9: The profile of the tapered layers (a) LVR1, (b) LVR2, LVR3, LVR4 and (c) LVR2-ver2, LVR3-ver2, LVR4-ver2 measured over the length of the device with a stylus profiler.

Since all these layers are on the same wafer and are going through the same transfer-etch step, it is not possible to achieve a wedge shape with an apex at the end while keeping the length the same for all of the layers. One-to-one plasma etching is performed such that LVR3 and LVR3-ver2 would result in an ideal triangular tapered layer. As a consequence, LVR1, LVR2 and LVR2-ver2 were over-etched, meaning that the same level difference as in LVR3 and LVR3-ver2 is achieved, while the length of the layer is shorter. In contrast, LVR4 and LVR4-ver2 have a smaller level difference compared to LVR3 and LVR3-ver2, while the length of the layer remains the same.

As seen in all of the profiles in Fig. 5.9, undesired bumps have been observed at both ends of the tapered layer, except for the over-etched layers. The short devices in Fig. 5.9(b) are suffering from surface roughness, while the rest of the layers are smooth. In-

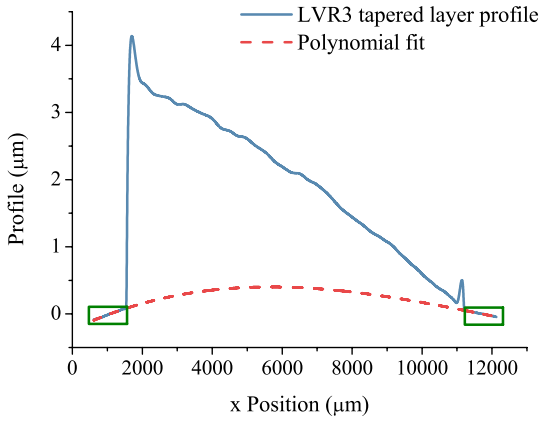

Figure 5.10: The correction of the stylus measurement data. The thin-film-free parts are indicated with green boxes.

tegrating a long filter with a detector array allows for a larger pixel size; thus, gives more freedom in the detector design. In addition, the longest device, LVR1, looks smooth and linearly tapered when its profile is compensated for the stress-induced curvature. However, it is not acceptable to ignore the effect of curvature on the taper slope in such a long device. Hence, the devices LVR2-ver2, LVR3-ver2 and LVR4-ver2 are the best candidates for proper filter operation due to their smooth surface and negligible bending thanks to their medium-level length.

The surface profiles of the tapered Bragg mirrors LVR2-ver2, LVR3-ver2 and LVR4-ver2 were measured before wafer bonding. The raw measurement data is shown in Fig. 5.11. Without any post-processing, the slope of the surface is almost linear with negligible roughness.

The performance of an LVOF with air cavity is highly dependent on the profile of the mirrors. The deviation from the linear taper might result in the nonuniform separation in the wavelength domain; thus, deteriorating the performance of the device. Moreover, since interference occurs at different positions along the length of the filter, the localized deviation of the taper, i.e. surface deformation, has a significant effect on the quality of the interference. The rule-of-thumb for the quality of an optical surface, either defined as surface form error of a lens [10] or dynamic deformation of a micro-scanner [11], is that the deviation from the nominal value must be less than $\lambda/10$, where λ is the shortest design wavelength. For a coarse pixel distribution in the detector array, such as 20 pixels over the length of 14 mm, results in a pixel size of 700 µm. As given in Fig. 5.12, the deviation from the ideal tapered profile at every 700 µm is within the limits of surface deformation, given that the shortest wavelength in the system is 3200 nm. Also, the highly linear measured profile of the tapered mirror allows for uniform separation of the

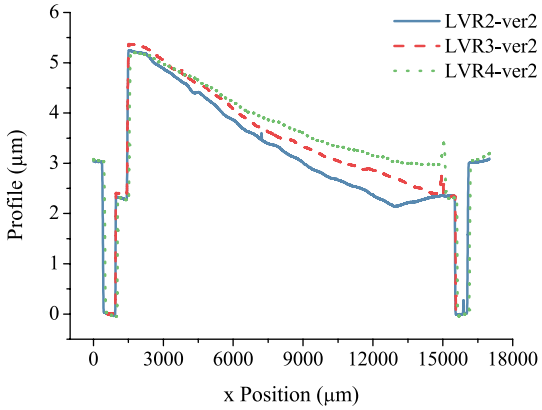

Figure 5.11: The raw profile data of the tapered Bragg mirrors LVR2-ver2, LVR3-ver2 and LVR4-ver2 measured before wafer bonding.

wavelengths.

5.5. WAFER BONDING

The flat and the tapered mirrors are integrated by direct wafer bonding [12]. Since direct wafer bonding relies on the short range intermolecular and interatomic attraction forces, the surface roughness becomes a critical parameter [13]. The frame of the device, where the two mirror wafers are bonded, had been protected by a thermal SiO_2 layer during the mirror fabrication. This protective layer is removed in a BHF bath before wafer bonding. Then, the wafer goes through the RCA1 cleaning step. In this step, the wafer is kept in a DI water, hydrogen peroxide(H_2O_2) and ammonium hydroxide (NH_4OH) solution of 5:1:1 volume ratio at 75 °C for 10 minutes. Later, the wafers are placed in the Marangoni drying bath filled with DI water at a neutral pH value. Drying takes place as the wafers are withdrawn from the bath while IPA is flowing toward the surface of the wafer at a rate of 500 sccm. The surface tension gradient introduced on the wafer forces the water film to drain back into the bath as described by the Marangoni effect [14]. As a consequence, the wafer comes out of the bath dry. For the Si-to-Si direct bonding, AML Aligner Wafer Bonder (Applied Microengineering Ltd, UK) is employed. The flat and tapered mirror wafers are aligned using the IR cameras installed in the system. Wafers are bonded in vacuum, using 3000 N force. In the last step, the bonded wafers are investigated under a near-IR camera as shown in Fig. 5.13(a). It was observed that the bonding was problematic around the edge of the wafer, while the dies close to the center were perfectly bonded. Finally, the bonded wafers are diced in 20 mm by 20 mm dies as shown in Fig. 5.13(b).

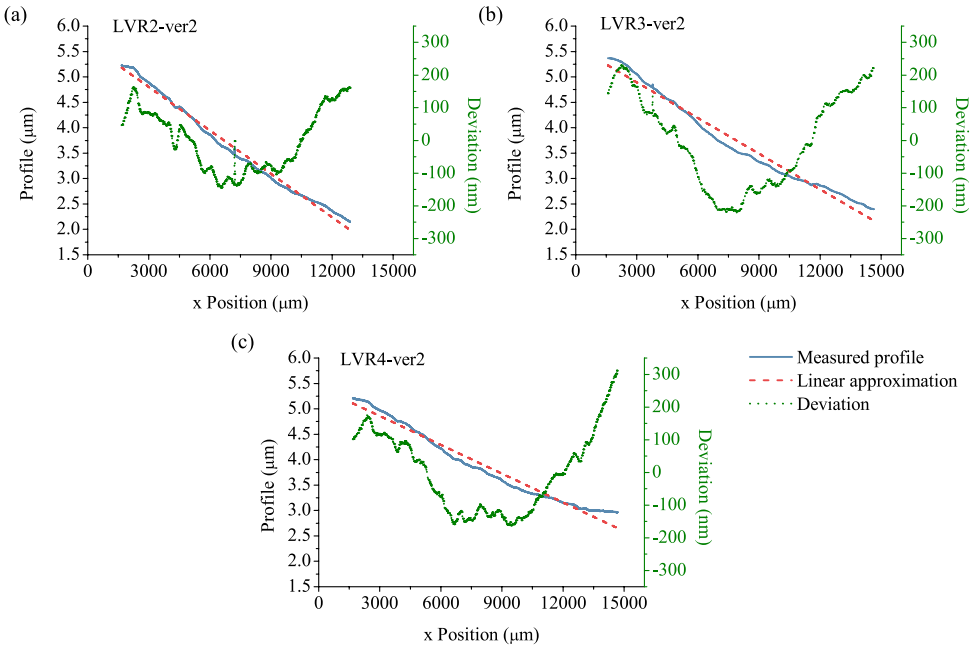

Figure 5.12: The measured profiles of the tapered Bragg mirrors LVR2-ver2, LVR3-ver2 and LVR4-ver2 compared with their linear approximations.

REFERENCES

[1] M. Fritze, J. Knecht, C. Bozler, C. Keast, J. Fijol, S. Jacobson, P. Keating, J. LeBlanc, E. Fike, B. Kessler, M. Frish, and C. Manolatou, *Fabrication of three-dimensional mode converters for silicon-based integrated optics,* Journal of Vacuum Science and Technology B **21**, 2897 (2003).

[2] A. Sure, T. Dillon, J. Murakowski, C. Lin, D. Pustai, and D. Prather, *Fabrication and characterization of three-dimensional silicon tapers,* Optics Express **11**, 3555 (2003).

[3] L. Abel-Tibérini, F. Lemarquis, and M. Lequime, *Masking mechanisms applied to thin-film coatings for the manufacturing of linear variable filters for two-dimensional array detectors,* Applied Optics **47**, 5706 (2008).

[4] A. Piegari, J. Bulir, and A. Krasilnikova Sytchkova, *Variable narrow-band transmission filters for spectrometry from space. 2. Fabrication process,* Applied Optics **47**, C151 (2008).

[5] C.-H. Ko, K.-Y. Chang, and Y.-M. Huang, *Analytical modeling and tolerance analysis of a linear variable filter for spectral order sorting,* Optics Express **23**, 5102 (2015).

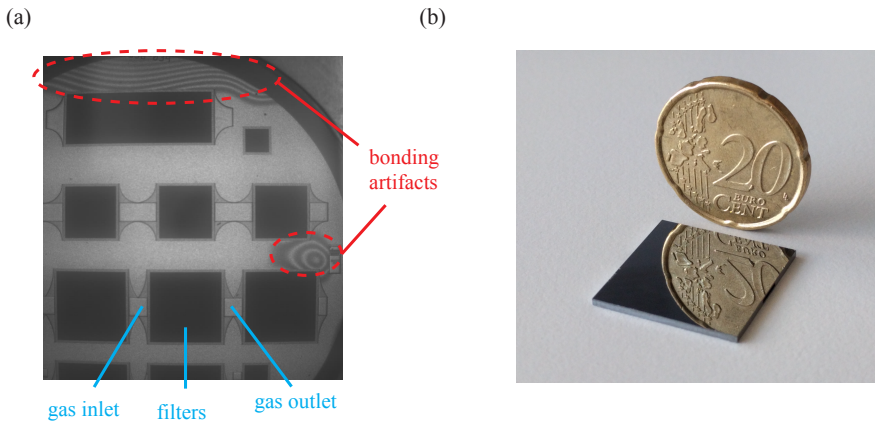

Figure 5.13: (a) The image of the bonded wafers, captured with a near-IR camera. (b) The photograph of a die with three filters.

[6] B. Sheng, P. Chen, C. Tao, R. Hong, Y. Huang, and D. Zhang, *Linear variable filters fabricated by ion beam etching with triangle-shaped mask and normal film coating technique,* Chinese Optics Letters **13**, 122301 (2015).

[7] A. Emadi, H. Wu, S. Grabarnik, G. de Graaf, and R. F. Wolffenbuttel, *Vertically tapered layers for optical applications fabricated using resist reflow,* Journal of Micromechanics and Microengineering **19**, 074014 (2009).

[8] A. Emadi, H. Wu, S. Grabarnik, G. De Graaf, K. Hedsten, P. Enoksson, J. H. Correia, and R. F. Wolffenbuttel, *Fabrication and characterization of IC-compatible linear variable optical filters with application in a micro-spectrometer,* Sensors and Actuators A: Physical **162**, 400 (2010).

[9] A. Emadi, *Linear-variable optical filters for microspectrometer application*, Ph.D. thesis, Delft University of Technology (2010).

[10] B. Braunecker, R. Hentschel, and H. J. Tiziani, *Advanced Optics Using Aspherical Elements*, Vol. 173 (SPIE Press, 2008).

[11] S. Hsu, T. Klose, C. Drabe, and H. Schenk, *Fabrication and characterization of a dynamically flat high resolution micro-scanner,* Journal of Optics A: Pure and Applied Optics **10**, 044005 (2008).

[12] M. Shimbo, K. Furukawa, K. Fukuda, and K. Tanzawa, *Silicon-to-silicon direct bonding method,* Journal of Applied Physics **60**, 2987 (1986).

[13] C. Gui, M. Elwenspoek, N. Tas, and J. G. E. Gardeniers, *The effect of surface roughness on direct wafer bonding,* Journal of Applied Physics **85**, 7448 (1999).

[14] A. F. M. Leenaars, J. A. M. Huethorst, and J. J. Van Oekel, *Marangoni drying: A new extremely clean drying process,* Langmuir **6**, 1701 (1990).

6

CHARACTERIZATION

QUANTITATIVE material identification in optical absorption spectroscopy is strongly related to the spectral performance of the measurement instrument. The resolution of these tools, usually specified in either wavenumbers (cm^{-1}) or wavelength (nm), determines which spectral lines in the spectrum could be resolved. The resolution of the instrument and the optical path length (OPL) of the sample cell largely determine the quality of the composition measurement.

The gas-filled linear variable optical filter (LVOF) also requires prior knowledge on the instrument resolution and the OPL of the sample cell to measure the composition of a gas mixture. Since the resonator cavity of an LVOF is used as a sample cell in the gas-filled LVOF, the effective OPL rather than the physical cavity length is taken into account. Unlike external sample cells with known dimensions, the assessment of the effective OPL of a gas-filled LVOF requires characterization with known samples at well-controlled experimental conditions.

In this chapter, the characterization of the gas-filled LVOF is presented in two parts. Firstly, the performance of the LVOF is investigated with both wideband and single-wavelength measurements. Secondly, the effect of the gas in the filter cavity is examined experimentally using a single-wavelength HeNe laser as well as a tunable optical parametric oscillator (OPO) laser as the light source in a custom-built optical setup.

6.1. FILTER CHARACTERIZATION

The spectral response of an LVOF can be measured by either combining it with a detector array or scanning the filter along its length with a single detector element. The latter is more flexible in the sense that the width of the detector element can be adjusted with a slit and the individual transmission curves can be constructed to assess the resolution, while the former would be more appropriate in a final microsystem. Therefore, the characterization of an LVOF in this thesis is based on scanning the filter along its length and measuring the transmission at every step in both wideband and single-wavelength arrangements.

6.1.1. WIDEBAND MEASUREMENTS

Fourier transform infrared (FTIR) spectrometers are commonly used for material identification in a wide wavelength range. The sample is quantitatively identified by measuring either the transmission (or equivalently absorption) through the sample or the reflection off the specimen based on its physical state. To acquire the spectral performance, first a reference measurement is done. Then, the sample is placed at the sample plane/chamber and another measurement is run. The ratio of the sample and the reference measurements is subsequently used for further data analysis.

Similarly, an FTIR spectrometer can be used to characterize an optical filter. The transmission through a Fabry-Perot (FP) filter can be measured by placing the filter at the sample plane and taking the ratio of the measurement with the filter to the measurement without the filter. Due to the repetitive nature of optical resonance, several orders of interference spanning the wavelength range of the FTIR spectrometer can be observed in the spectrum.

Analogous to characterizing a fixed FP filter, the incoming light beam can be limited by a slit, such that the spectral response of only one channel in an LVOF is acquired. Therefore, by placing an LVOF after a slit and scanning it along its length, a spectrum that is composed of several sets of interference orders can be measured.

Prior to the fabrication of the gas-filled LVOF, 3-pair Si/SiO_2 Bragg mirrors were prepared based on the design specifications discussed in chapter 4. The reflectivity of these mirrors is extracted from the transmission measurement assuming negligible absorption. An FTIR spectrometer (Vertex 70, Bruker Optics, Germany) with a Mercury Cadmium Telluride (MCT) detector that is cooled with liquid nitrogen is used in the measurements. The resolution of the instrument is selected as $4\,cm^{-1}$, while the aperture after the mid-IR emitter is set to 0.5 mm in diameter. After averaging over 32 scans, the reflectivity of the mirror is calculated using the transmission measurement as shown in Fig 6.1 in the 2 µm to 5 µm wavelength range.

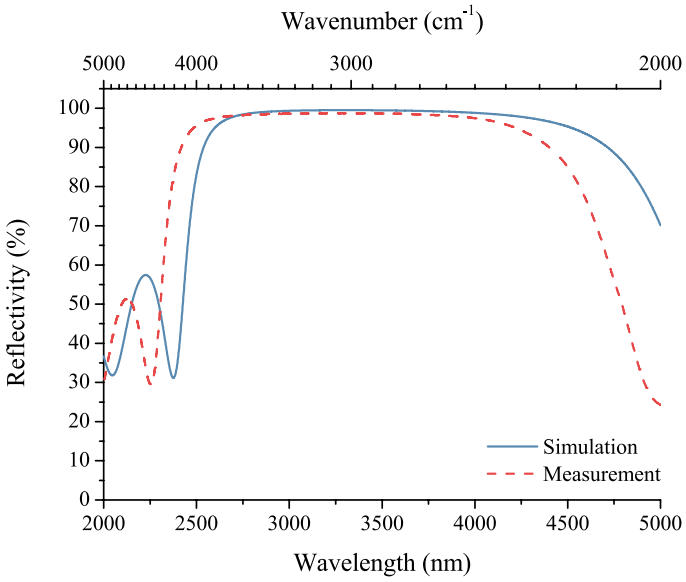

Figure 6.1: Measured and simulated reflectivity of a 3-pair Si/SiO_2 Bragg mirror.

The slight spectral shift between the simulated and measured reflectivities stems

mainly from the fabrication tolerances. The unavoidable fluctuations in the deposition conditions affect both the physical and the optical properties of the thin films. As a result, the reflectivity might slightly change in wavelength as well as in amplitude. However, since the wavelength range of the device is 3.2 µm to 3.4 µm, the slight shift in the reflectivity does not affect the operation of the filter.

Two flat Bragg mirrors, one fabricated on a bare Si wafer and the other on a 24.9 µm KOH etched cavity are clamped together. The response of the resulting FP filter that is tuned to 3320 nm at the 15th operating order is measured using an FTIR spectrometer as shown in Fig. 6.2. The transmission curves in the desired wavelength range are highly suppressed, while the curves of both higher and lower orders start to increase in amplitude as they shift to shorter and longer wavelengths.

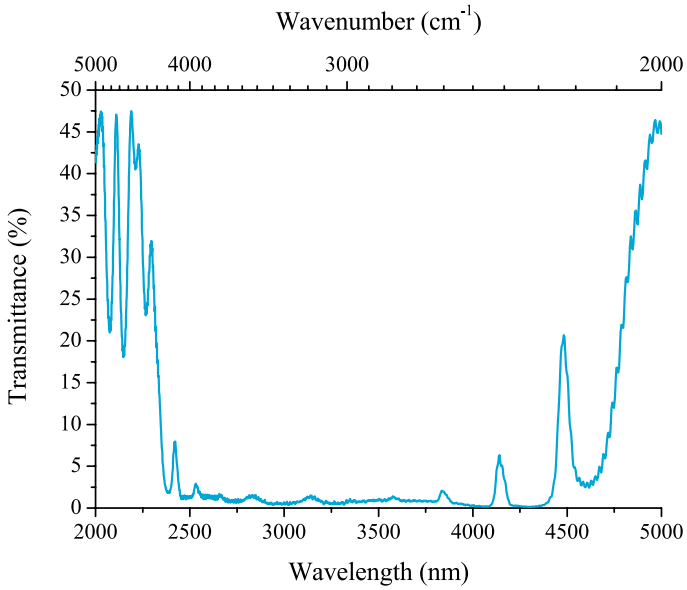

Figure 6.2: The measured transmission through an FP filter with a cavity length of 24.9 µm.

As discussed in chapter 3, the collimation of the light source has a substantial effect on the spectral performance of interference filters operated at demanding conditions. This forced us to investigate the measurement instrument in more detail, so that the limitations of the device and the instrument could be correctly analyzed.

OPTICAL LAYOUT OF THE FTIR SPECTROMETER

FTIR spectrometers are conventionally composed of a light source, a Michelson interferometer, a detector and optical components to collimate, focus and collect the light. The light beam is focused on the sample at the sample plane to allow for the analysis of

small specimens. Moreover, most FTIR spectrometers allow the user to adjust the spot size at the sample plane by changing the size of the aperture after the light source. In a perfect optical system, the spot size at the aperture would be replicated at the sample plane. However, due to divergence and the different effective focal length (EFL) of the collimating and focusing mirrors, the spot size at the sample plane differs from the selected aperture size. Moreover, the size of the aperture directly affects the cone angle of the light beam impinging on the sample surface. Therefore, it is crucial to study the propagation of the light beam in the measurement system to interpret the characterization results.

The optical layout of the FTIR spectrometer is shown in Fig. 6.3 [1]. The emission from the source is collected by an elliptical mirror, which then focuses the light beam on the aperture. Later, the light beam passes through the aperture and gets collected by a 90° off-axis parabolic mirror with 50 mm diameter and 100 mm EFL. After propagating from the first parabolic mirror (collimating) to the second (focusing) through the interferometer for 470 mm, the light beam gets reflected off the focusing mirror. The second 90° off-axis parabolic mirror has a diameter of 50 mm and an EFL of 180 mm. Later, the beam is focused at the sample plane after passing through a window with 40 mm diameter. Lastly, the light beam that is transmitted through the sample is focused on the detector by an elliptical mirror.

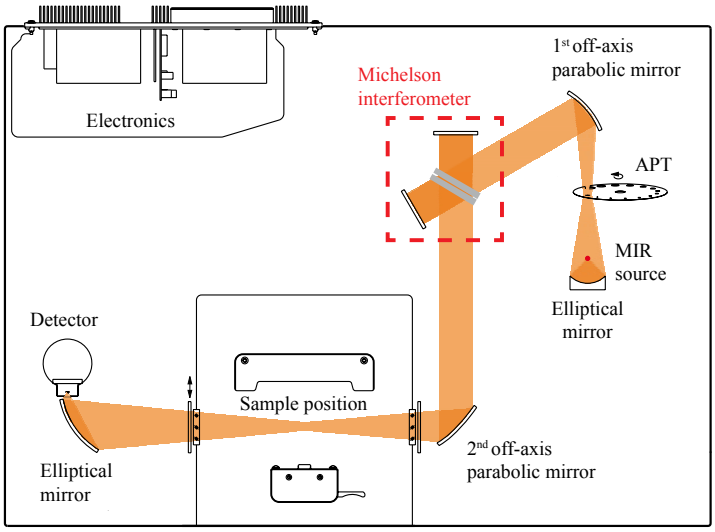

Figure 6.3: The layout of the FTIR spectrometer, Vertex 70 from Bruker Optics [1].

According to the information provided by the manufacturer, the diameter of the beam after the first off-axis parabolic mirror denoted by D is defined by Eq. 6.1, where APT is

the aperture diameter, $D_{m,eff}$ is the effective diameter of the mirror and d is the distance of the image plane from the mirror.

$$D \approx 2APT\frac{d}{EFL} + D_{m,eff} \tag{6.1}$$

To create a similar layout with the given specifications, a simple calculation using the sketch in Fig. 6.4 is done as follows: instead of an aperture and an off-axis parabolic mirror, an imaginary point source with a half cone angle (β) is introduced in the system, where the mirror is defined as a standard surface with 50 mm circular aperture in the ray tracing software, Zemax.

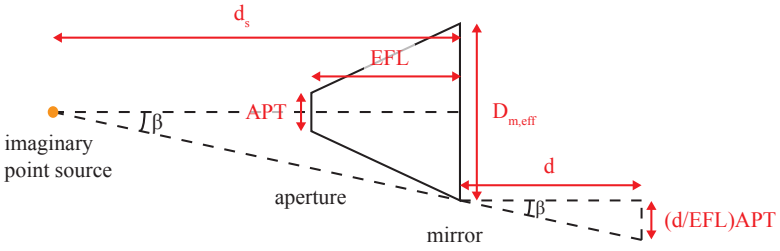

Figure 6.4: The approximation of the optical layout from the light source until the second off-axis parabolic mirror.

The cone angle of the imaginary point source can be described by Eq. 6.2 using the two triangles indicated with dashed lines. Moreover, the distance between the mirror and the imaginary point source (d_s) can be extracted from the similarity between the small and the large triangle.

$$tan\beta = \frac{APT}{EFL} = \frac{D_{m,eff}/2}{d_s} \tag{6.2}$$

The aperture size of the instrument varies from 0.25 mm to 8 mm. As the aperture gets smaller, the signal-to-noise ratio (SNR) decreases and the cone angle of the light beam impinging on the sample increases. For the FP filter measurements shown in Fig. 6.2, the diameter of the aperture was selected as 0.5 mm. Thanks to the high sensitivity of the cooled MCT detector, even the highly suppressed peaks with less than 2% peak transmittance were captured.

For $APT = 0.5$ mm and $EFL = 100$ mm the cone angle of the imaginary point source is calculated as 0.28°. Using $D_{m,eff} = 40$ mm as provided by the manufacturer, results in a separation of $d_s = 4000$ mm between the imaginary point source and the mirror. These values as well as description of the whole layout are then used to design a simplified optical layout for the FTIR spectrometer in Zemax as shown in Fig 6.5.

The size of the spot at the window is measured as 16.84 mm, while the focused light

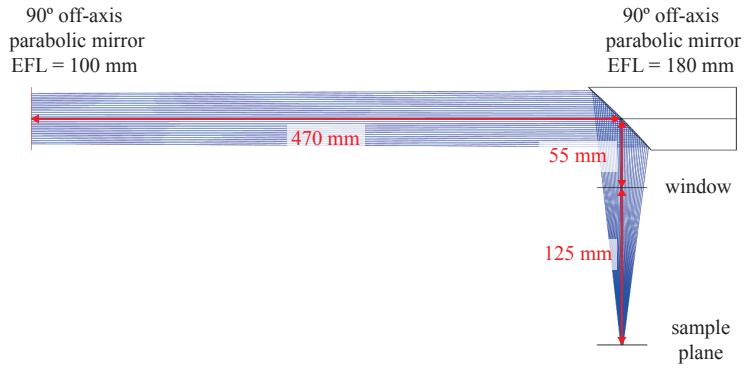

Figure 6.5: The simplified optical layout of the FITR spectrometer.

beam has a diameter of 1.02 mm at the sample plane as shown in Fig. 6.6. The change in the spot size, combined with the 125 mm distance between the sample plane and the window, translates into a light beam with 7.2° half cone angle impinging on the filter.

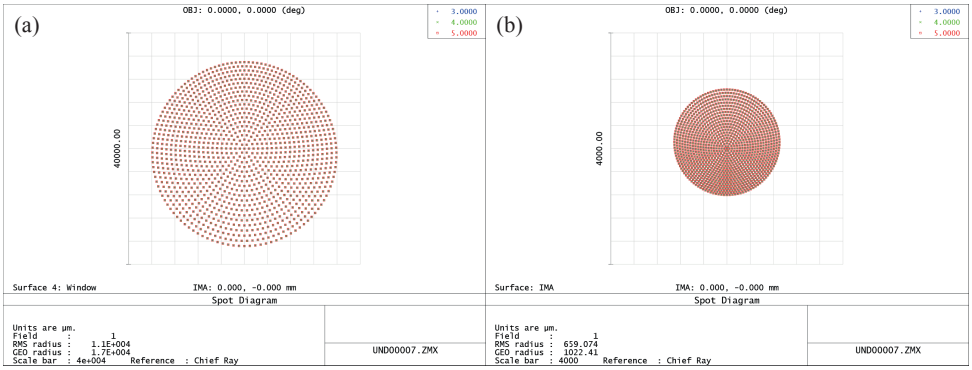

Figure 6.6: Spot diagram of the light beam at (a) the window and (b) the sample plane.

The transmission of the FP filter with 24.9 µm cavity length is simulated using the FP model and the measured reflectivity of the flat mirror that had been given in Fig. 6.2. As shown in Fig. 6.7, the filter is very sensitive to the collimation of the light source when the reflectivity of the mirrors is high. As the mirror reflectivity decreases, the transmission peaks start to appear, confirming the cone angle discussion given in chapter 3. At short wavelengths around 2500 nm, where the operating order is higher than 15, the reflectivity is still high, suppressing the transmittance at these demanding operating conditions. At longer wavelengths, on the other hand, the operating order is lower as well as the reflectivity of the mirrors. Therefore, the filter is less vulnerable to the cone angle of the light, allowing a peak transmittance of almost 20% at 4500 nm wavelength.

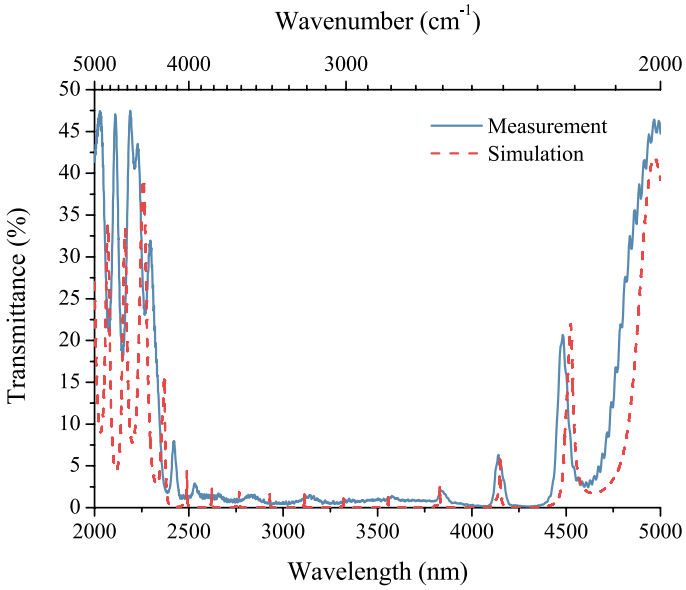

Figure 6.7: The comparison of measured transmission of an FP filter with a cavity length of 24.9 µm to the calculated transmission using the measured mirror reflectivity.

The same FTIR spectrometer with a Deuterated Tri Glycine Sulfate (DTGS) detector is employed for the wideband characterization of the LVOF. Since the sensitivity of the DTGS detector is worse than the cooled MCT detector, the aperture size is selected as $APT = 8$ mm to increase the SNR. Given the properties of the rest of the optical components, this translates into an imaginary point source that is $d_s = 250$ mm away from the first off-axis parabolic mirror with a 4.57° half cone angle in the simplified Zemax layout of the instrument. In this case, the diameter of the light spot at the window is simulated as 19.73 mm, while the spot size decreases to 7.45 mm at the sample plane. Therefore, the half cone angle of the light beam impinging on the filter can be calculated as 5.6°.

The spectral channels are separated spatially along the length of the filter using a 200 µm wide and 3 mm tall slit. By placing the slit in front of the filter at the sample plane and scanning the filter along its length at 2 mm steps using a translational stage, the spectral response of the LVOF is measured as shown in Fig. 6.8. At each step, 32 scans were averaged to improve the SNR. Moreover, the resolution of the instrument was set to 4 cm^{-1}, which is less than 5 nm in wavelength. Similar to the FP filter, the transmission curves in the desired wavelength range (i.e. 15^{th} order) are suppressed due to the cone angle of the light beam. As discussed in chapter 3, the effect of cone angle is less significant in the LVOF compared to an equivalent FP filter, due to the nonparallel configuration of the mirrors. The peak transmittance at 3325 nm wavelength is measured

as less than 1% in the FP filter, while it is approximately 3% in the LVOF thanks to the combined effect of the nonparallelism of the mirrors and the smaller cone angle in the LVOF measurements.

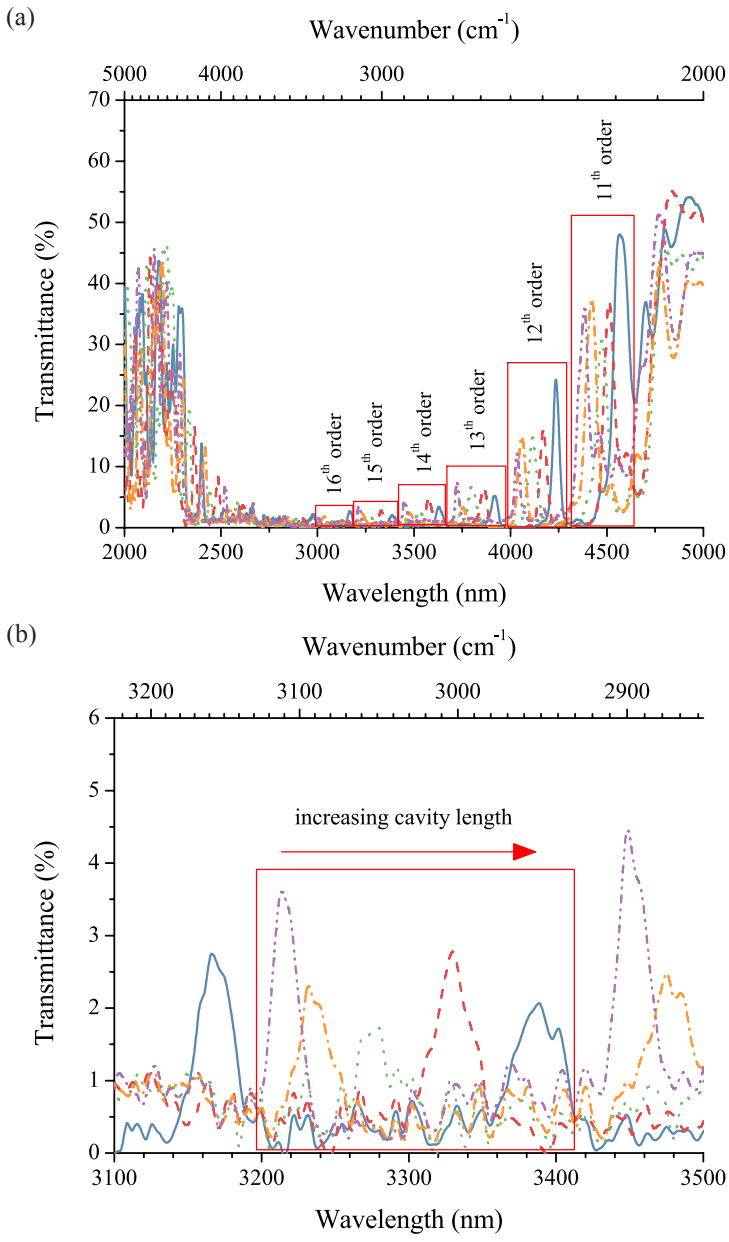

Figure 6.8: The transmission curves of the LVOF measured with the FTIR spectrometer in the (a) 2 µm to 5 µm and (b) 3.1 µm to 3.5 µm wavelength ranges.

Analyzing the FTIR measurement results is not trivial for a number of reasons, including, but not limited to, the cone angle limitation. After passing through the filter, the light propagates toward an elliptic mirror, where it is focused on the detector. Hence, the light propagates for almost 25 cm with a focusing element in the path after filtering. Therefore, the filter-detector separation, which is an important parameter in the characterization of an LVOF, cannot be controlled in the FTIR measurements. Furthermore, the SNR limit of the instrument forces us to use a slit that is wider than the required size to capture the expected transmission curve in detail. As the slit gets wider, a wider range of cavity length is covered, which means a wider wavelength range will be transmitted per measurement; thus, making the transmission curve wider.

Although the curves are widened and exhibit a very low transmittance (< 5%), there is a spectral shift toward longer wavelengths at increasing cavity length; thus, qualitatively demonstrating the functionality of the filter in a wideband arrangement as shown in Fig. 6.8(b) in the desired wavelength range.

6.1.2. SINGLE-WAVELENGTH MEASUREMENTS

The gas-filled LVOF is to be integrated with a wideband light source and a detector array in the final device. However, to investigate the spectral resolution limit, the device must be characterized using a light source with a spectral purity that is better than the resolution of the LVOF. Moreover, the light source must be highly collimated to overcome the cone angle limitation. Furthermore, the setup must be sufficiently flexible so that the filter-detector separation and the incidence angle of the light beam are both adjustable.

The mid-IR is a very information-rich band for material identification due to the fact that the vibrational modes of many organic molecules fall within 3 µm to 5 µm wavelength range. However, there are only a handful of commercially available light sources that meet the requirements of the characterization method, i.e. high resolution and high degree of collimation. The HeNe laser at 3392 nm (Research Electro-Optics, Inc., Colorado, USA) is the only single-wavelength laser in the market in the mid-IR. For the wideband operation, optical parametric oscillator (OPO) based tunable lasers stand out. Firefly-IR (M Squared Lasers, Ltd., Glasgow, Scotland) and Cobolt Odin (Cobolt AB, Solna, Sweden) are OPO-based commercially available tunable lasers in the band of interest. Despite their high resolution and high degree of collimation, the latter two are costly instruments used mainly for research purposes. Much effort has been put in the development of quantum cascade lasers (QCLs) in the last decade. Commercially available QCLs are currently in the 4 µm to 12 µm wavelength range [2]; however, there is ongoing research about the development of QCLs in the 3 µm to 5 µm band [3].

An optical setup with the HeNe laser at 3392 nm wavelength is built to measure the spectral response of the LVOF and to validate the theoretical discussion as shown in Fig.

6.9. The laser has a 2 mW minimum output power and a 2.13 mrad full angle of divergence. The $1/e^2$ beam diameter, where the intensity drops down to 0.135 of its peak value is 2.02 mm. The degree of linear polarization is usually quantified as the extinction ratio, which is the transmitted intensity of p-polarized light relative to the s-polarized light. A high extinction ratio indicates a very pure transmitted p-polarized beam. The extinction ratio of the HeNe laser is specified as 500:1, meaning that the output of the laser is highly p-polarized. The linewidth of the laser is indicated as 200 MHz in frequency, which translates into 7.67 pm in wavelength. Therefore, the HeNe laser meets the high resolution and high degree of collimation requirements of the characterization method.

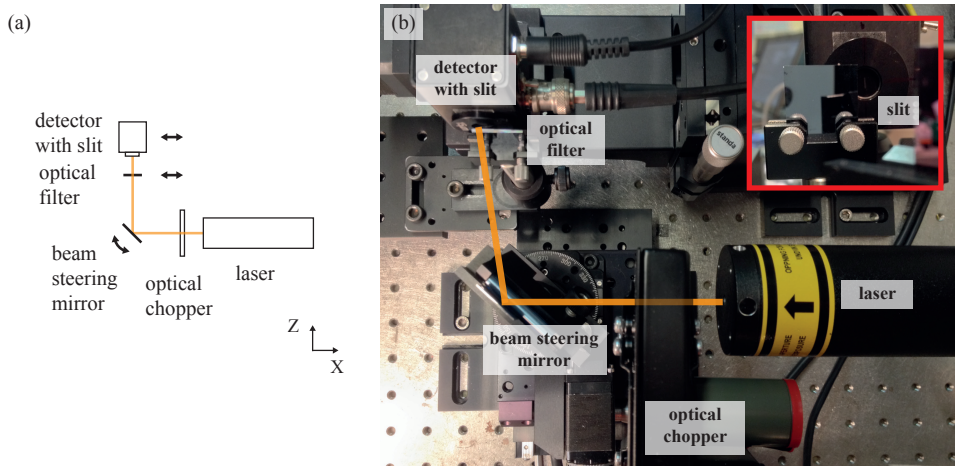

Figure 6.9: (a) A schematic illustration of the optical characterization setup with the HeNe laser. (b) The actual optical characterization setup. The optical filter and slit are shown in detail in the inset.

An optical chopper that operates at 1 kHz is placed in front of the laser output to improve the SNR. After the optical chopper, a beam steering mirror that is mounted on a motorized rotational stage is used for steering the beam for the intended angle of incidence. The optical filter to be characterized is mounted on a motorized translational stage and moved along its length. Lastly, a large-area Lead Selenide (PbSe) detector (ET-6000, Electro-Optics Technology, Inc., USA) with a 15 µm wide and 3 mm tall slit is mounted on another motorized translational stage for proper position monitoring during consecutive measurements. The detector signal is band-pass filtered to allow the signal at only 1 kHz to pass by cascading a high- and a low-pass filter (SR650, Stanford Research Systems, USA). The filtered signal is then recorded with a high performance digital multimeter (Keithley 2002, Keithley Instruments, Inc., USA).

The measurement is done by first aligning the detector with the laser such that the

maximum signal is obtained. Then, the filter is inserted again in the light path and the position range on the filter that corresponds to the transmission curve at 3392 nm wavelength is searched. This range is scanned by moving the filter along its length so that the curve is fully captured. The step size of the movement is selected as 15 µm, same as the slit width, to avoid any convolution effect or missing data.

The motorized stages and the high performance digital multimeter are controlled via computer using Labview. The entire scan is performed in a loop, where the start and stop positions, as well as the step size of the filter movement are used as loop parameters in the software. During the scan, two intensity measurements are performed for each position to account for the fluctuations in the laser power. The first measurement without the filter is used as a reference, while the second measurement is done with the filter in the light path. The ratio of the latter to the former gives the transmittance at that particular position along the length of the filter. By repeating the same measurement scheme from the start to the stop position, the transmission curve that belongs to the 3392 nm wavelength is constructed.

The measurement results at the filter-detector separation $z = 6$ mm are shown in Fig. 6.10 for various incidence angles. It must be noted that in these measurements, the tapered reflector LVR4-ver2 is used. Due to the repetitive movement of the filter in and out of the light path, each measurement takes about 1 hour. To avoid the effect of possible overheating on the filter performance, two scans were taken after turning on the laser that were later averaged to calculate the transmission response. Then, the laser was turned off for half an hour to cool down until the next measurement. The x-position in this setup indicates the position on the filter, where the curve that corresponds to 3392 nm wavelength is located, rather than the distance from the imaginary wedge apex as was used in the optical simulations. The shift in the x-position of the filter, which results from the angular positioning of the beam steering mirror, is corrected for different values of the angle of incidence in the measurement results. Therefore, the relative values rather than the absolute values of the x-position must be taken into account in the measurements.

The transmission curve at normal incidence exhibits a low peak transmittance with side peaks emerging at positions away from the wedge apex, which is in agreement with the theoretical analysis. As the incidence angle gets smaller, the transmission curve starts moving toward the wedge apex with an increasing peak transmittance. At the optimum incidence angle, the peak transmittance reaches almost 40%, while the top part of the curve becomes significantly narrow. The full width at half maximum (FWHM) of this curve is measured as 105 µm in the x-position, which corresponds to 4.1 nm spectral resolution. When the incidence angle is further decreased, the peak transmittance starts to get lower and the curve leans away from the wedge apex as expected.

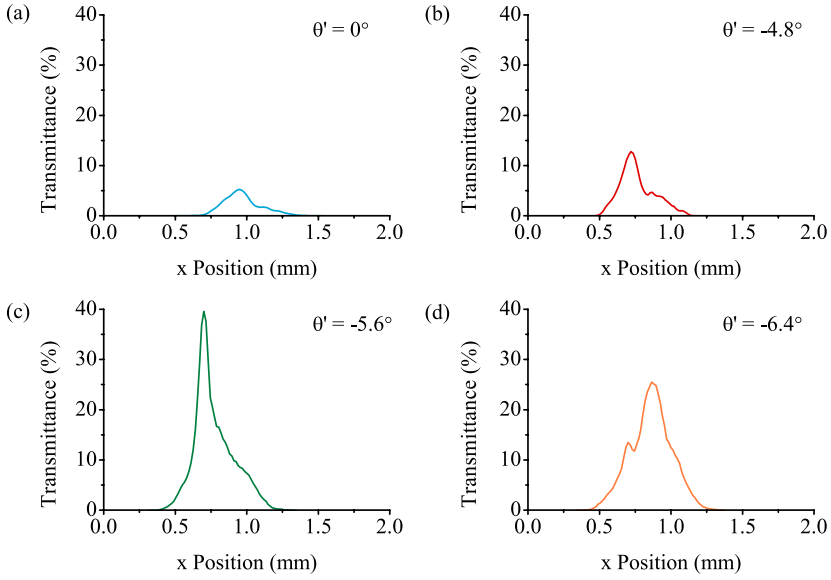

Figure 6.10: Measured transmission curves at (a) normal incidence, (b) $\theta' > \theta'_{opt}$, (c) $\theta' = \theta'_{opt}$ and (d) $\theta' < \theta'_{opt}$.

The device was simulated using the actual cavity length that was calculated using the measured mirror profile given in Fig. 5.11. The spectral response at a filter-detector separation of $z = 6$ mm is shown in Fig. 6.11 for various incidence angles. The step size in the x-position was selected as 1 µm in calculations. The simulated spectral response has been averaged to a single value over every 15 data points to be consistent with the measurement that has been performed with a 15 µm wide slit. The simulated optimum incidence angle is higher than the measured value. Nevertheless, the curves confirm the shapes and shifts in position.

The main reason of the widening of the transmission curves is that the responses of several different cavity lengths are captured at every measurement step. This can be caused by both the filter and the measurement setup. The thickness of an ideally tapered layer at a certain position along its length is the same at every position along its width. Therefore, if the slit width is small enough to capture the transmission curve, as is illustrated in Fig. 6.12(a), no widening will be observed. In this application, the tapered cavity is defined by the tapered mirror, which is fabricated by thermal-chemical reflow of photoresist blocks with linearly variable width. The reflow process rounds the corners of these blocks, which results in an arc-shaped taper rather than a linear one. Therefore, the part of the slope that is selected by the slit during measurements spans a wider range of cavity length; hence, a wider spectral range as shown in Fig. 6.12(b) that

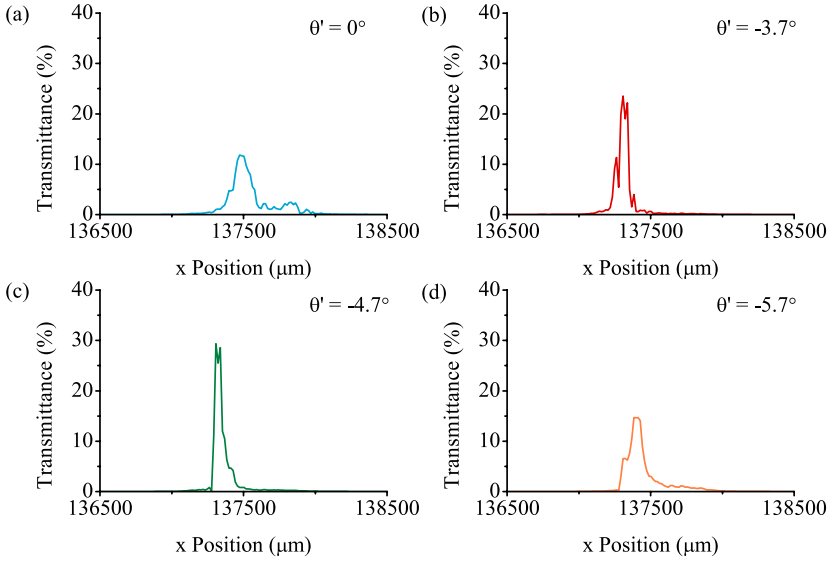

Figure 6.11: Simulated transmission curves at (a) normal incidence, (b) $\theta' > \theta'_{opt}$, (c) $\theta' = \theta'_{opt}$ and (d) $\theta' < \theta'_{opt}$.

results in wider transmission curves. Moreover, the alignment between the slit and the filter affects the results in a similar way as shown in Fig. 6.12(c). Since the slit is mounted on the detector housing without any alignment marks, it might be tilted with respect to the filter. For instance, if the slit is 3° tilted, the x-position that is covered by the slit will increase by 157 μm assuming an ideally tapered mirror. Compared to the width of the slit, this will have a substantial effect in the measurement results.

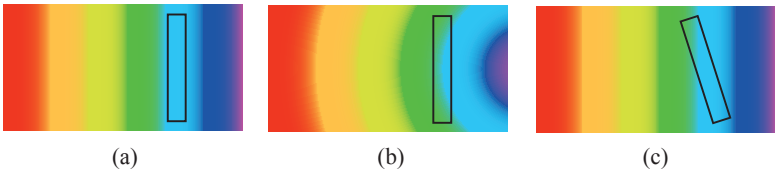

Figure 6.12: The relationship between (a) a straight slit and an ideal taper, (b) a straight slit and an arc-shaped taper, and (c) a tilted slit and an ideal taper.

The slight difference between the measured and simulated peak transmittance is related to the fabrication. The fabrication tolerance of the Bragg mirror layer deposition is neglected in simulations, where reflectivity has an important effect. It is impossible to avoid layer thickness alteration during fabrication; hence, a lower reflectivity compared to the simulations must be anticipated in the actual device. These filters are expected to exhibit a higher peak transmittance at lower mirror reflectivity due to the demanding op-

erating conditions. Therefore, the discrepancy between the measured and the simulated peak transmittance can be explained by thin-film deposition tolerances.

6.2. GAS MEASUREMENTS

The gas-filled LVOF translates a µm-level physical cavity into a mm-level effective optical path. Despite the improvement, the effective OPL of a gas-filled LVOF is shorter than commercially available sample chambers. The gas cell with the shortest absorption path available in the market is 5 cm long, which results in full absorption in our measurement method. Moreover, placing the filter inside a gas cell limits the flexibility of the optical setup in terms of the adjustment of incidence angle and filter-detector separation. Therefore, the sample gas must remain only in the cavity during the measurement, so that the effect of optical path elongation could be observed.

6.2.1. DEVICE PACKAGING

The proof-of-concept device includes three filters in a row with openings on the left and the right side of the filters. During the experiments, these openings are used as gas inlet and outlet. A pressure difference between the two results in a gas flow through the cavity. The challenge is to connect a big tube to the 550 µm wide openings without damaging the device during the repetitive measurements. Moreover, the reference measurement requires taking the device out of the optical path at every step. Given the die size of 20 mm, this necessitates very frequent long distance movement of the device. Therefore, the package must be compact enough to minimize the time spent for taking the filter out of the optical path so that the laser remains stable during the measurement.

The intended package is composed of two parts and the device is clamped between them. The bottom part has an 18 mm by 18 mm opening, where the filters are located. A shallow bed that covers the frame of the die is designed to hold the device in such a way that, when the die is placed in the bottom part, the top surfaces of the package and the die would be at the same level. The bottom part of the package also houses a built-in channel for the gas to flow, that is connected to the gas tube at the bottom and aligned with the openings on the sides of the die at the center. The second part of the package is rather simple, a thin and flat frame with an 18 mm by 18 mm opening at the center.

3D printing is an innovative technology that offers rapid prototyping with low cost. The resolution of the 3D printers and the variety of materials that can be printed are constantly improving. We selected the strong and flexible material offered by Shapeways (Shapeways BV, Eindhoven, The Netherlands) to print the package for the gas-filled LVOF. The bottom part of the package with the die in it is shown in Fig. 6.13(a). The device is clamped between the two parts of the package and tightened at the corners using screws

as shown in Fig. 6.13(b). Finally, the device is sealed around the frame using a thin layer of silicone.

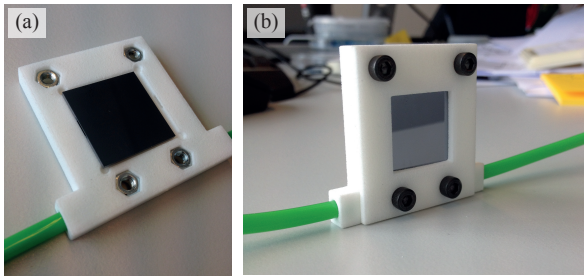

Figure 6.13: The 3D printed package, (a) the bottom part of the package with the gas-filled LVOF die in it and (b) the whole package with the gas inlet and outlet.

Initial tests with the package showed that most of the gas coming out of the inlet tube leaked from the package before reaching the openings on the device. This was caused by the powder-like material used in 3D printing. Covering the package with resin was suggested for proper sealing; however, another aspect of the package, i.e. the thickness, was limiting the flexibility of the measurements. The increasing filter-detector separation due to the thickness of the package counteracted the optimization of the angle of incidence. As the incidence angle became more negative, the transmitted light was blocked by the package before it could reach the detector. This limited the position range that could be scanned along the length of the filter. Therefore, we decided to switch to simpler packaging options, where we rely on the sealing of the wafer bonding.

Instead of putting a frame around the die, the openings on the sides of the filters are connected directly to the inlet and the outlet tubes. As shown in Fig. 6.14(a), the connection can be done using dispensing tips with silicone as the gluing agent. Pieces of silicon wafer are used for extra support. However, putting long dispensing tips at the sides of the device limits the reference measurements of the filter in the middle. Another approach is to partially split the tube along its length and seal the device on the frame using silicone as shown in Fig. 6.14(b). Both of the packages shown in Fig. 6.14 are used in the gas measurements discussed in the following sections.

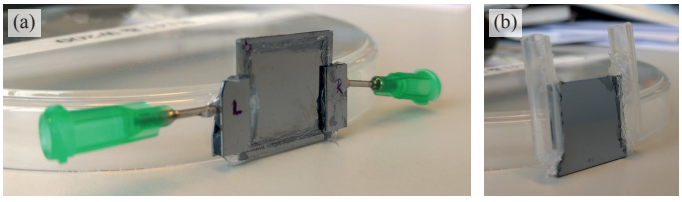

Figure 6.14: Gas inlet and outlet connected to the device (a) via dispensing tips and (b) directly.

6.2.2. HeNe LASER MEASUREMENTS

The effect of optical path elongation can correctly be characterized if the sample gas is present only in the cavity of the LVOF. To selectively flow gas in the cavity of the device with the reflector LVR4-ver2 that was described in chapter 5, dispensing tips are glued to the openings on both sides of the device using silicone. The inlet is connected to the gas bottle via flexible tubing, while the outlet tube is left open and pointing away from the measurement area. The gas flow through the cavity is ensured by applying a pressure of a few mbar above atmospheric pressure to the gas inlet. The optical characterization setup with the HeNe laser that is adjusted for the gas measurements is shown in Fig. 6.15.

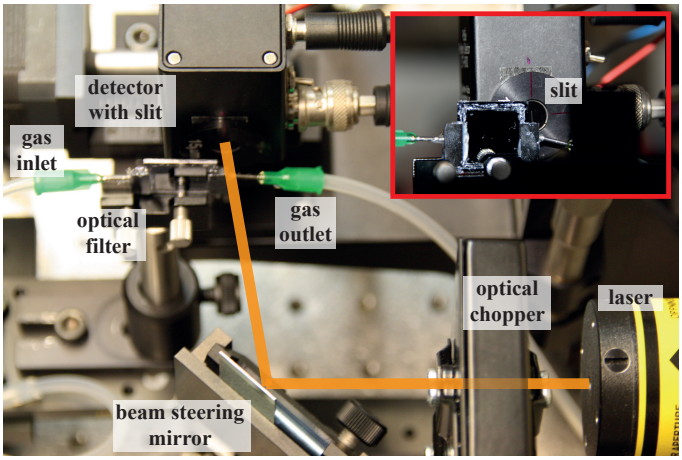

Figure 6.15: Optical characterization setup for methane measurements.

The same laser measurement procedure has been employed for the gas experiments. Thanks to the flexible tubing, the repetitive mechanical movement of the filter holder did not disturb the measurements. To avoid the effect of a possible gas leakage on the optical performance, a fan was placed above the filter.

The position of a transmission curve depends strongly on the cavity length and a small perturbation could shift the curve to another position. During the measurements, we observed that due to the pressure of the gas flowing toward the cavity, the mirrors on each side were pushed outwards. The resulting increase in the cavity length shifted the x-position of the transmission curve. Therefore, a comparison between the transmission of the filter at ambient pressure to the filter with methane above the ambient pressure is not valid, since the optical performance of the latter could be affected by the physical influence of the gas pressure. To overcome this, the filter measurement at ambient pressure was replaced with a measurement using a nonabsorptive gas, nitrogen in this case, at the same experimental conditions as the methane measurement. Thus, the

physical effect of the gas pressure would be the same for both measurements.

The transmission curves of the filter at 3392 nm wavelength with methane and nitrogen in the cavity are shown in Fig. 6.16. Because of the dispensing tips, the detector had to be placed further than 6 mm, resulting in a smaller optimum incidence angle of −8.8°. The peak transmittance of the reference measurement with nitrogen (39.9%) is in agreement with the theory in the sense that the same optimum transmission curve can be found at a different incidence angle for every filter-detector separation.

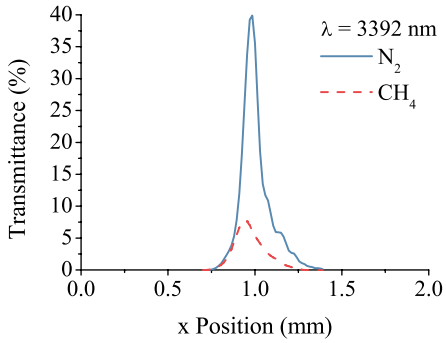

6

Figure 6.16: The measured transmission response of the gas-filled LVOF at 3392 nm wavelength with methane and nitrogen in the cavity.

Compared to the high peak transmittance of nitrogen, methane absorbs almost 80% of the light with a 7.8% peak transmittance. The slight positional shift in the peak transmittance of the two measurements arises from the pressure setting. The output pressure of the gas bottle is adjusted manually using a valve while reading the value on an analog gauge. The pressure displayed on the gauge was 7 mbar and 5 mbar above the ambient pressure for methane and nitrogen respectively, thereby explaining the minor shift in the position of the peak.

The absorption of gas in a spectroscopic measurement system is highly dependent on the resolution of the wavelength-selective element. In the gas-filled LVOF, where the light source is a wideband infrared emitter, the resolution is determined by the filter. In the laser-based experiments, on the other hand, the resolution of the system is determined by the light source rather than the filter, since the spectral purity of the HeNe laser outperforms the LVOF in terms of spectral resolution. The absorption coefficient of methane corresponding to the 7.67 pm resolution of the HeNe laser at 3392 nm wavelength is extracted from the HITRAN database, using the information-calculating system Spectroscopy of Atmospheric Gases (ICS SPECTRA) for unit pressure and absorption length as 1.0314 mm^{-1} [4, 5]. Then, the modified absorption coefficient is used as an attenuation factor in the simulations performed with the actual cavity length values. Averaging is applied to the transmittance at every 15 µm to be consistent with the mea-

surements. The transmission curves of only the filter and the filter with methane are shown in Fig. 6.17. The peak transmittance of only the filter is 29.3%, while the absorption of methane decreases this value to 1.52%, which translates into 2.86 mm effective OPL, given the modified absorption coefficient. Compared to the physical cavity length of 25.44 µm, 112.6-fold elongation is achieved.

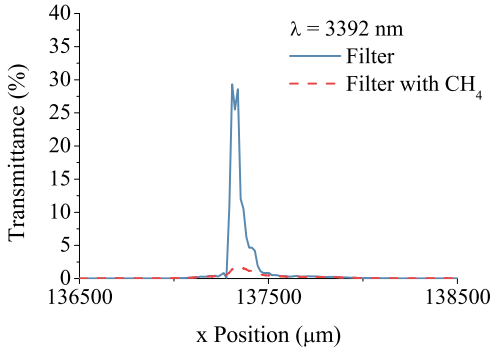

Figure 6.17: The simulated transmission response of the gas-filled LVOF at 3392 nm wavelength. The effect of methane is introduced using the modified absorption coefficient.

The effective OPL is calculated as 1.58 mm for the measured absorption of methane as was shown in Fig. 6.16, using the modified absorption coefficient value. Therefore, the physical cavity length of 25.44 µm is elongated by 62.2-fold, experimentally. The difference between the simulated and the measured elongation factor arises from the fabrication tolerance of the Bragg mirror layer deposition. The unavoidable fluctuations in the thin-film layer thickness results in a reduced reflectivity, which is observed as an increased measured peak transmittance of almost 40% compared to the 29.3% simulated peak transmittance. Lower mirror reflectivity is equivalent to a reduced number of reflections, thereby limiting the elongation to 62.2-fold compared to the simulated value of 112.6-fold.

Both simulated and measured effective OPLs are shorter than the values derived in chapter 4. Even though the designed and fabricated devices have minor differences in taper angle and mirror layer thicknesses, the reduction in the effective OPL cannot be solely explained by these effects.

The explanation becomes clear when considering the fact that the operating principle of the gas-filled LVOF is similar to cavity enhanced absorption spectroscopy (CEAS), since both methods exploit multiple reflections from high-finesse optical cavities. In the CEAS method, as the absorption of the sample becomes comparable to the cavity loss, the sensitivity improvement saturates [6]. In other words, the absorption of the sample begins to dominate the effective number of cavity passes. Therefore, the effective OPL

becomes a function of the absorption coefficient, or equivalently the concentration, of the sample. The narrow linewidth of the HeNe laser allows it to resolve narrower absorption peaks with higher coefficients. The increased absorption saturates the sensitivity and limits the effective number of reflections. Thus, the difference between the effective OPL of the optical design and both the experimental and the simulated OPL that is based on profile measurements is primarily a result of the high resolution of the laser.

6.2.3. OPO LASER MEASUREMENTS

For the characterization of the gas-filled LVOFs in a wide wavelength range, a highly collimated broadband light source is required. Moreover, the resolution of the laser must be better compared to the filter, so that the spectral limits of the device could be experimentally specified. Therefore, we collaborated with the Trace Gas Research Group from Radboud University to characterize our devices with their benchtop mid-IR OPO laser.

Optical parametric oscillator lasers are powerful tools in laser spectroscopy, especially at the wavelength bands that are difficult to access through stimulated emission from a gain medium such as mid-IR [7–10]. In OPO lasers, a pump beam is converted into signal and idler beams by a nonlinear crystal as shown in Fig. 6.18. The optical gain is achieved by parametric amplification in the nonlinear crystal that is placed in a resonator cavity. The output wavelength of an OPO laser is tuned in a wide range by altering the phase-matching condition [11]. This condition is usually adjusted by changing the temperature or the orientation of the nonlinear crystal.

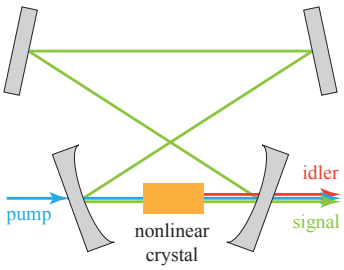

Figure 6.18: A schematic illustration of the OPO laser.

The setup for the OPO laser is described in detail in [12]. The OPO laser is pumped by a 1064 nm distributed Bragg reflector (DBR) diode laser (EM4, Bedford, Massachusetts, USA). The nonlinear crystal is placed inside a bow-tie ring resonator that is composed of two plano-concave and two plane mirrors. The output wavelength is adjusted by altering the position and the temperature of the crystal.

The output of the laser is highly collimated; however, due to the slight misalignment between the mirrors, it is no longer a Gaussian beam. To convert the TEM_{10}-like spot

into TEM_{00} mode, i.e. a Gaussian beam, the output of the laser is coupled into a fiber. Due to the small core diameter and small refractive index difference between core and cladding, single-mode fibers support only the TEM_{00} mode [13]. Then, the light beam coming out of the fiber is collimated and used as the light source for the characterization of the gas-filled LVOF. The optomechanical setup used in the HeNe laser measurements is integrated to the OPO laser as shown in Fig. 6.19.

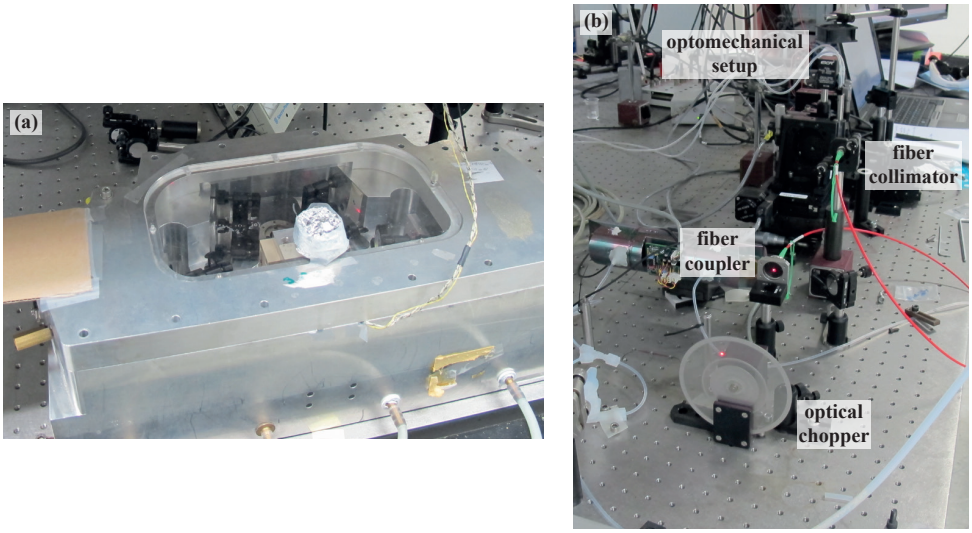

Figure 6.19: (a) The OPO laser. The pump laser enters the setup on the left side, while the output beam leaves the setup on the right side. (b) The output of the OPO laser passes through the optical chopper, propagates through the fiber and finally reaches the optomechanical setup.

The entire setup is schematically illustrated in Fig. 6.20(a). The output of the OPO laser is focused on the fiber coupler (FiberPort PAF-X-4-E, Thorlabs, Germany) while passing through an optical chopper operating at 1.6 kHz. After propagating through a single mode ZrF_4 fiber (P3-23Z-FC-1, Thorlabs, Germany), the TEM_{00} mode is collimated by an aspheric lens package with 5.95 mm focal length (F028APC-3450, Thorlabs, Germany), resulting in a 1 mm diameter light beam with a measured divergence of 0.126° at 3.3 µm wavelength. The collimated light beam is then directed at the optomechanical setup described before, as shown in Fig. 6.20(b).

The chip that is shown in the inset of Fig. 6.20(b) has three filters with openings at both sides for gas flow. Among these filters, LVR3-ver2 is selected for the OPO laser measurements. Since this device is at the center of the die between the openings, using long dispensing tips as gas inlet and outlet is not practical. Instead, the device is partially placed in the split tubing and sealed with silicone. The bottle with the pure sample gas and nitrogen as the IR-inactive diluting component are combined into a single flow

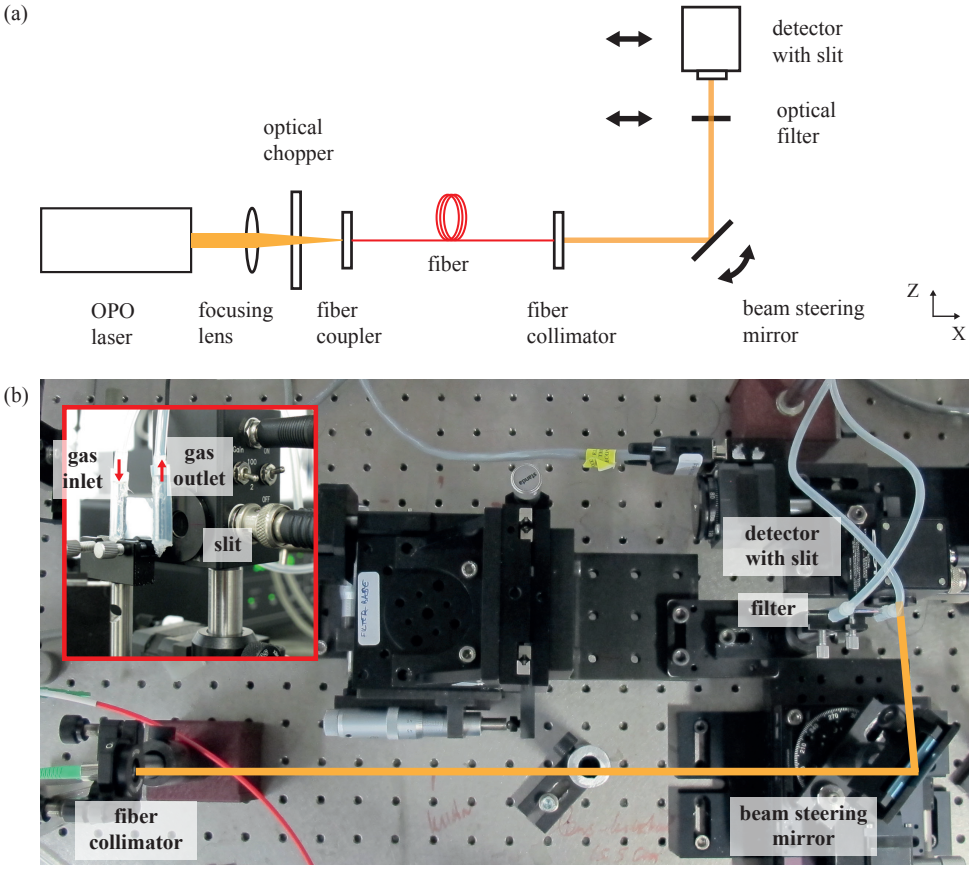

Figure 6.20: (a) A schematic illustration of the entire setup with the OPO laser as the light source. (b) The actual optomechanical setup with the fiber collimator.

with a T-shaped tubing adapter. The flow of both gases is controlled by a mass-flow controller (5850S, Brooks Instrument, USA) at a rate of 3 $\mathrm{L\,h^{-1}}$ in total. To assure the gas flow through the resonator cavity of the filter, the gas outlet is connected to a vacuum pump and the pressure is set to 750 mbar.

In the final device, two identical filters; one with openings to allow the ambient gas inside and one fully sealed, are used for measurement and referencing respectively. Moreover, the filters are fabricated directly on top of a detector array. Therefore, the final device does not require the use of mass-flow controllers or extra tube sealing; the reference device is sealed during wafer bonding. In contrast, keeping the gas only inside the cavity during characterization is crucial to be able to measure the effect of using the resonator also as a gas cell. Hence, extra precaution should be taken during the measurements to remove any leaking gas from the optical path. A fan was placed on top of the device to avoid any leaking gas absorb the incoming light. Since the sealing with silicone was not perfect, the gas pressure inside the cavity is assumed to be equal to the atmospheric pressure.

The experimental procedure starts with tuning the wavelength of the laser by choosing the right slab on the nonlinear crystal and subsequent computer-controlled temperature setting. Then, the position of the transmission curve at this wavelength is approximately located along the length of the device. Subsequently, the incidence angle is adjusted for the optimum transmission while 100% nitrogen is flowing through the resonator cavity. To calculate the transmittance, first the filter is taken out of the optical path and a reference measurement is done, then the filter is brought back in the optical path and scanned along its length at a step size of 15 µm. The ratio of the filter to the reference measurement gives the transmittance. To see the effect of the gas, first pure sample gas is flown into the cavity and then diluted with nitrogen to observe the effect of concentration in filter transmission. For methane, four measurements at 3221.69 nm, 3270.75 nm, 3317.89 nm and 3416.60 nm wavelengths are performed. The nonlinear crystal in the OPO laser was not optimized for the 3.2 µm to 3.4 µm wavelength range; thus, only a handful of wavelengths could be selected given the required time for the temperature stabilization.

A coarse adjustment of the beam steering mirror resulted in the experimental optimum incidence angle of −6° at a filter detector distance of approximately 7 mm, while the OPO laser was tuned to 3416.60 nm wavelength. As shown in Fig. 6.21, the response of the filter to the injection of gases was very repeatable and stable. The transmission curve with 18.88% peak transmission has an experimental FWHM resolution of 309.68 µm in position at a cavity taper angle of 12.9 millidegree, which translates into 10 nm FWHM resolution in wavelength. In the final device, the resolving power of the sensor is determined by the resolution of the filter; however, in the experimental setup

the resolution of the laser theoretically outperforms the filter. Hence, the absorption coefficient of methane that is used for the effective OPL calculation is modified using the 10 MHz linewidth of the laser. Using the peak transmittance ratio of pure methane and nitrogen, an effective OPL of 1.534 mm is calculated. This is equivalent to an elongation of 64-fold compared to the 23.916 µm long physical cavity.

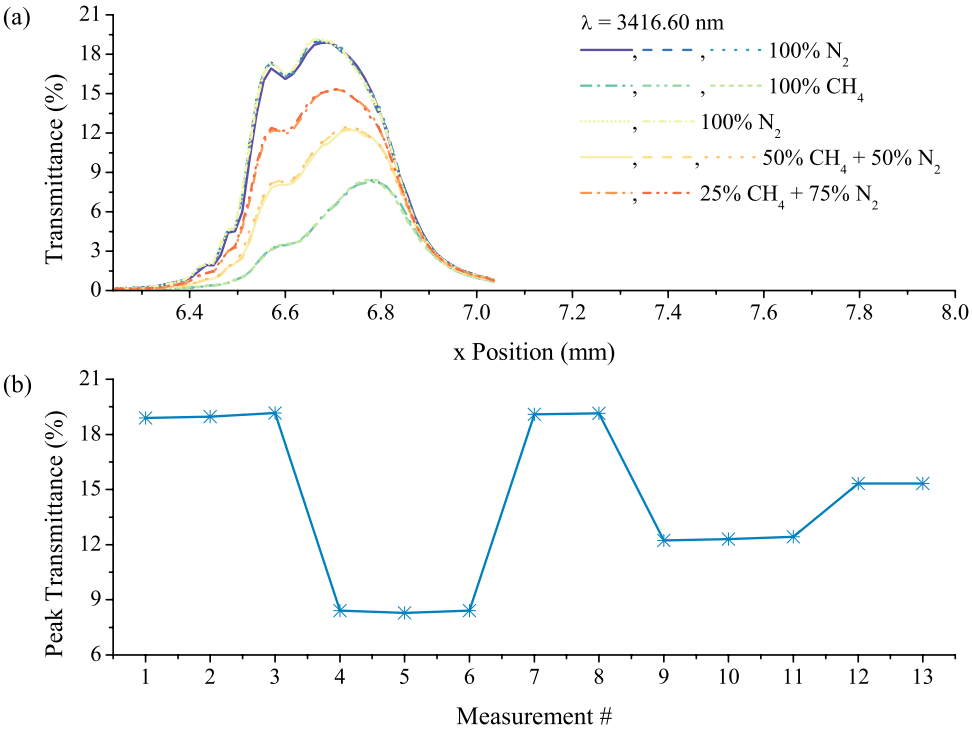

Figure 6.21: The spectral response of the gas filled LVOF measured at 3416.60 nm wavelength with pure nitrogen and methane in addition to 50% and 25% of methane in a mixture diluted with nitrogen. (a) The transmission curves measured along the length of the filter with various samples. For each sample 2 or 3 scans were done. (b) The peak transmittance values extracted from the transmission curves.

The wideband operation of the filter is crucial for sample selectivity. Transmission curves with and without sample gas were measured at four different wavelengths along the length of the device as shown in Fig. 6.22. The shape of the curves, as well as the peak transmittance and FWHM resolution, are different at each wavelength. This is mainly due to the position-dependent optimum incidence angle that is a direct result of the position dependency of the tapered mirror reflectivity. In the final device, the average of the optimum incidence angle will be selected, or the position dependency of the reflectivity will be removed, by tapering the Si wafer instead of the SiO_2 layer of the Bragg mirror. However, during the measurements, the optimum angle was adjusted for 3416.60 nm

wavelength and the alignment was kept the same for the remaining wavelengths. The change in peak transmittance with the sample on the other hand is highly dependent on the absorption of the sample at that wavelength.

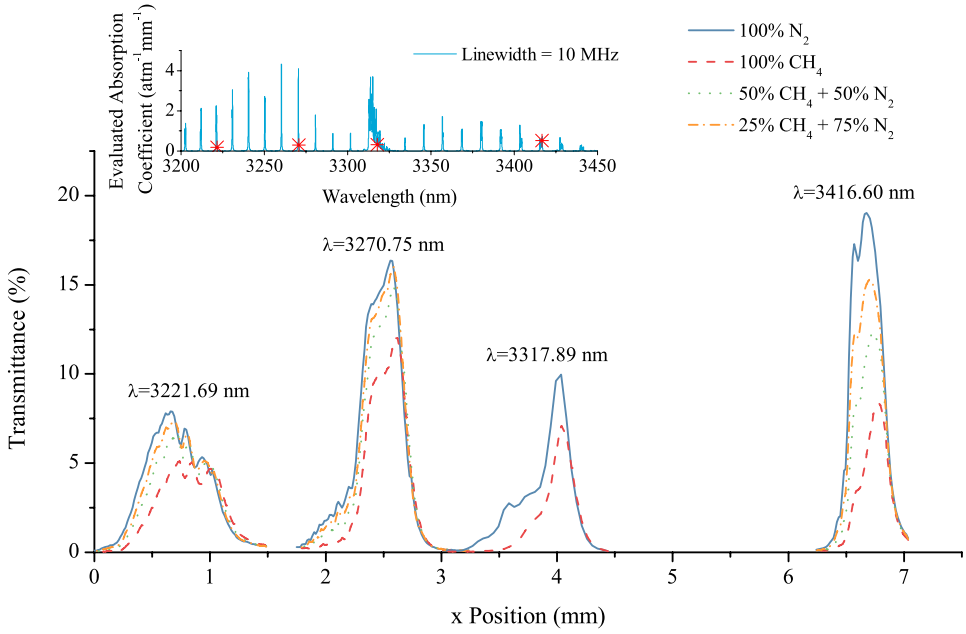

Figure 6.22: The measured spectral response of the gas filled LVOF at 3221.69 nm, 3270.75 nm, 3317.89 nm and 3416.60 nm wavelengths. The inset shows the modified absorption coefficient of methane for a laser linewidth of 10 MHz, which is the resolution of the experimental OPO laser used in measurements. The values that correspond to measurement wavelengths are labeled with a star.

The higher hydrocarbons, ethane and propane, have distinctive spectral features in the 3.25 µm to 3.5 µm and 3.3 µm to 3.5 µm wavelength ranges, respectively. Since there is no high-resolution data on these gases available, the comparison is made qualitatively. According to the PNNL database, as presented in Fig. 4.3, both gases are almost nonabsorptive at 3222 nm, while propane has a higher absorption coefficient at 3449 nm than ethane does at 3448 nm. As shown in Fig. 6.23(b) and 6.23(d), pure propane absorbs 54.6% of the light compared to ethane absorbing only 15.8%. At 3222 nm wavelength, the peak transmittance of the measurement with the pure gases remains almost the same as shown in Fig. 6.23(a) and 6.23(c). However, we observed a slight shift of the curve along the length of the filter. Similar shifts, either as the whole curve or the peak transmittance, were observed in all measurements. Although it has not been systematically confirmed, we believe that the dispersion of light in the sample (i.e. the refractive index of the gases are slightly different from that of nitrogen), which was disregarded in the simulations, combined with the position dependent reflectivity of the tapered mirror and imperfec-

tions in the taper itself, results in various shifts in the spectral response.

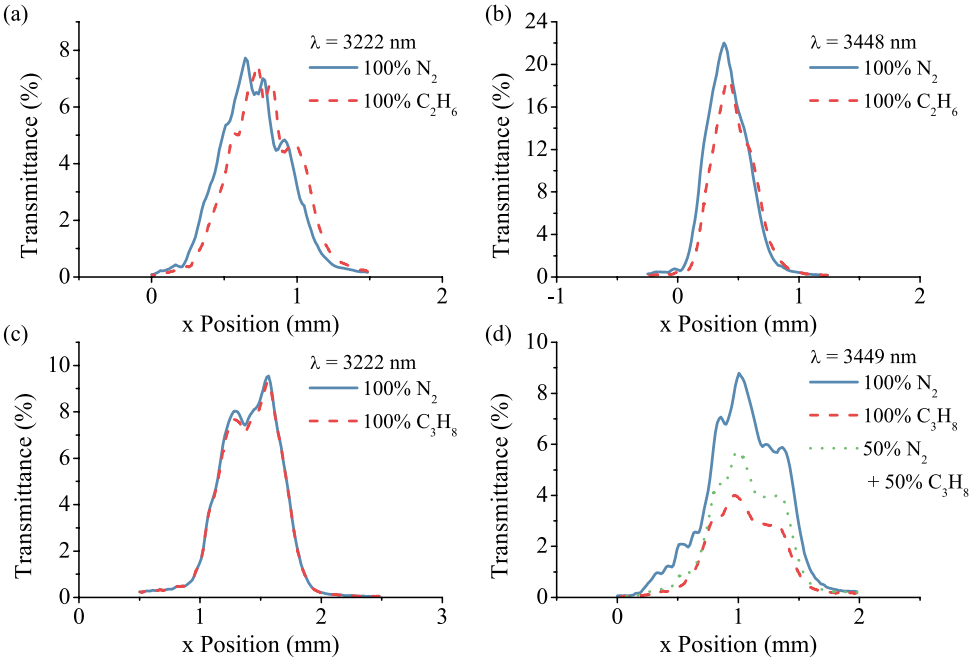

Figure 6.23: The spectral response of the filter with ethane and propane measured at two wavelengths. The spectrum of ethane compared to nitrogen at (a) 3222 nm and (b) 3448 nm wavelength. The spectrum of propane compared to nitrogen at (c) 3222 nm and (d) 3449 nm wavelength.

6.3. RESULTS AND DISCUSSION

In this chapter, the feasibility of a gas-filled LVOF for the composition measurement of natural gas is demonstrated with actual measurements with methane, ethane and propane. Moreover, the theoretical approach presented in chapter 3 that is based on the Fizeau model is confirmed with experimental results. Although gas-filled LVOF is a new concept and benchmarking requires a complete device with a light source and a detector, various aspects of the sensor can still be evaluated.

The most important property of a sensor is the selectivity. A highly selective sensor is capable of distinguishing the entire composition of a sample. Selectivity of the gas-filled LVOF is achieved by the distinctive spectral features of the target molecules in mid-IR and the wideband operation of the sensor tailored for this wavelength range. Although the spectra of hydrocarbons are very similar, they have characteristic features in the 3.2 µm to 3.4 µm spectral window. The highly oscillating spectrum of methane starts from 3.15 µm and extends up to 3.5 µm. The absorption of ethane begins at 3.25 µm,

thereby allowing methane and ethane to be distinguished in the 100 nm wide spectral window between 3.15 µm and 3.25 µm. Propane and butane have almost identical absorption features that start from 3.3 µm wavelength. Since the latter two gases constitute only a small part of the natural gas, much interest is paid to their combined concentration. Therefore, the gas-filled LVOF that operates in the 3.2 µm to 3.4 µm wavelength range with an experimental resolution of 4.1 nm, as demonstrated in this chapter, is suitable for distinguishing methane, ethane as well as the combination of propane and butane, when the wavelength selectivity is considered.

Sensitivity is another crucial aspect of sensors. The concentration sensitivity of the gas-filled LVOF is highly dependent on the measurement limit of the detector, given the power of the light source. A change in the sample concentration always alters the transmitted intensity. However, this change should exceed the detection limit of the sensor for a measurable response. Since the measurements of the gas-filled LVOF are performed with a commercially available detector integrated with a slit to replicate a detector pixel, the concentration sensitivity and the limit of detection are set by the performance of the detector rather than the filter.

Due to the stability of the light source and availability of the data, the measurements with methane at 3416.60 nm wavelength are employed in the calculation of the concentration sensitivity. The peak transmittance of the filter with pure nitrogen is compared to dilutions with 25% and 50% methane concentration as well as to pure methane as shown in Fig. 6.24. The related absorption coefficient values are also indicated on the top x-axis, assuming 1 atm pressure for 100% methane. Despite the limited number of data, the slope of the linear fit shows that 1% change in the concentration of methane requires the detection of 0.104% change in the transmittance of the gas-filled LVOF.

The peak transmittance of a 14 mm long LVOF is simulated at 3390 nm wavelength with respect to the absorption coefficient of the sample as shown in Fig. 6.25. The filter is operated at the 15^{th} order and has a taper angle of 6.13 millidegree. In agreement with the discussion on the reduced sensitivity at high absorption coefficient values in CEAS, the peak transmittance curve exhibits an exponential decay, where the slope - or equivalently the concentration sensitivity - gradually decreases with increasing absorption coefficient. The linear response regime for this particular device can be defined as $0\,mm^{-1}$ to $0.08\,mm^{-1}$ using the linear approximation. Although the comparison of Fig. 6.24 to Fig. 6.25 reveal qualitative overlapping in the spectral response, further analysis is required to draw an analogy.

The wavelength sensitivity, or usually referred to as spectral sensitivity, is a property of both the detector and the filter. Due to the varying thickness of the first SiO_2 layer and thereby the varying reflectivity of the tapered mirror, the peak transmittance changes over the length of the LVOF. As presented in the measurement section, various experi-

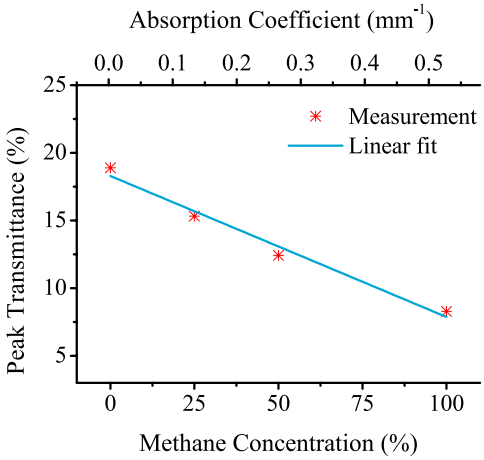

Figure 6.24: The peak transmittance of the gas-filled LVOF measured at 3416.60 nm wavelength using various methane concentrations.

mental peak transmittance values were observed at different wavelengths. Therefore, if the specifications of the detector are known, the wavelength sensitivity can be calculated for the entire operating range using the filter properties.

Accuracy and precision are important parameters that must be specified in the commercialization step of the sensor. Within the framework of the proof of concept, the accuracy can only be specified in a rather crude fashion and from two different perspectives: the accuracy of the LVOF and the concentration accuracy of the gas measurements, with the latter being the critical specification for the user. The measured and simulated transmission responses of only the filter, as shown in Fig. 6.10 and Fig. 6.11 respectively, are in good agreement. The slight difference between the two arises from the fabrication and characterization tolerances.

The main requirement for the assessment of the concentration accuracy is measuring the effective OPL with previously known concentrations of a sample in controlled experimental conditions. This requires unlimited access to the characterization setup and the sample handling equipment, as well as having two identical devices - one sealed reference filter and one measurement filter with gas inlet and outlet - integrated to identical detector arrays. Given the limited access, the effective OPL values presented in this thesis were extracted from only a small number of measurements.

Similarly, the precision of the device is strongly influenced by the experimental conditions, particularly by the stability of the light source. When the wavelength of the laser is stable, the same transmission curve can be measured with high precision. As shown in Fig. 6.21, the OPO laser was very stable at 3416.60 nm and a high level of repeatability

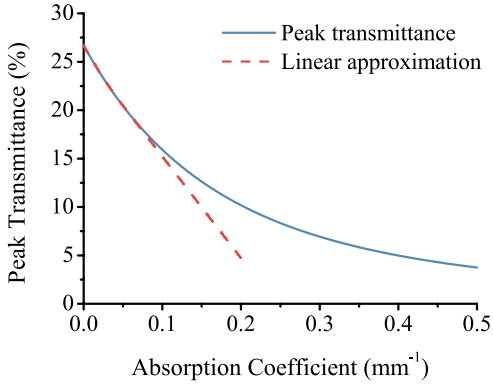

Figure 6.25: The peak transmittance of the gas-filled LVOF calculated at 3390 nm wavelength using various values of absorption coefficient.

was observed. Apart from the rest of the optical components, the LVOF is a passive device without any moving parts and the environmental conditions, such as temperature, have negligible effect on the thin-film properties. Therefore, the LVOF is well-suited for high precision optical measurements.

The calculated effective OPL is highly dependent on the spectral resolution of the laser, which outperforms the LVOF. In the final device, a wideband light source is combined with the LVOF and the resolution of the LVOF determines which spectral lines of the sample are resolved. Due to the high spectral purity of the light source, the absorption coefficient of the sample is higher in the current configuration. This leads to a shorter effective OPL, due to the absorption coefficient dependency of the OPL as in CEAS. In the final device, the resolution and therefore, the absorption coefficient of the sample is determined by the LVOF, which is very similar to the NIST database that was presented in Fig. 4.2. In that case, the effective optical path will be longer than the values measured using the laser as the light source.

The response time is an important parameter in chemical sensing. Optical chemical sensing is inherently a real-time measurement method. Considering the gas flow rate and the length of the pipeline in a household, the response time of an optical sensor is short enough to control the burner dynamically for the application. The measurements presented in this chapter are also, in a sense, in real-time. Nevertheless, since the measurements are based on scanning the filter along its length, it takes some time to construct the transmission curve. In the final device the filter is integrated with a detector array and, instead of the transmission curve, the area under the curves that corresponds to the pixel width is measured. Therefore, apart from the delay that originates from the electronics and the analysis, a real-time measurement is possible with a detector array.

The robustness of the gas-filled LVOF can be interpreted in two ways: the robust-

ness originating from the physical properties of the device and the long-term stability of the measurements. The robustness of the sensor arises from the fact that there are no moving parts in the device. The robustness of the measurements, on the other hand, is strongly dependent on the characterization setup. The repeatability, for instance, is directly affected by the wavelength stability of the laser. As is evident from the multiple measurements of the same sample, the filter response is very stable provided that the wavelength of the light source does not fluctuate. Since the filter characterization is performed by measuring individual transmission curves, the wavelength stability of the light source is crucial. However, it should be noted that a wideband light source rather than a laser is to be used in any future product based on the gas-filled LVOF. Therefore, the wavelength stability is no longer a problem in the final device. Moreover, the instability of the light source in terms of power is also not an issue, due to the self-referencing property of the method.

REFERENCES

[1] Bruker Optics, *Vertex 70 FTIR Spectrometer,* Accessed: 27.05.2016.

[2] L. Bush, *Quantum cascade lasers for infrared spectroscopy: Theory, state of the art, and applications,* Spectroscopy **28** (2013).

[3] M. Razeghi, N. Bandyopadhyay, Y. Bai, Q. Lu, and S. Slivken, *Recent advances in mid infrared (3-5 μm) quantum cascade lasers,* Optical Materials Express **3**, 1872 (2013).

[4] L. S. Rothman, I. E. Gordon, A. Barbe, D. C. Benner, P. F. Bernath, M. Birk, V. Boudon, L. R. Brown, A. Campargue, J. P. Champion, K. Chance, L. H. Coudert, V. Dana, V. M. Devi, S. Fally, J. M. Flaud, R. R. Gamache, A. Goldman, D. Jacquemart, I. Kleiner, N. Lacome, W. J. Lafferty, J. Y. Mandin, S. T. Massie, S. N. Mikhailenko, C. E. Miller, N. Moazzen-Ahmadi, O. V. Naumenko, A. V. Nikitin, J. Orphal, V. I. Perevalov, A. Perrin, A. Predoi-Cross, C. P. Rinsland, M. Rotger, M. Šimečková, M. A. H. Smith, K. Sung, S. A. Tashkun, J. Tennyson, R. A. Toth, A. C. Vandaele, and J. Vander Auwera, *The HITRAN 2008 molecular spectroscopic database,* Journal of Quantitative Spectroscopy and Radiative Transfer **110**, 533 (2009).

[5] E. V. Semiletova, Y. F. Arshinov, C. N. Mikhailenko, Y. L. Babikov, and V. F. Golovko, *Information-calculating system spectroscopy of atmospheric gases. The structure and main functions,* Atmospheric and Oceanic Optics **18**, 685 (2005).

[6] G. W. Drake, *Springer Handbook of Atomic, Molecular, and Optical Physics* (Springer Science & Business Media, 2006).

[7] G. M. Gibson, M. H. Dunn, and M. J. Padgett, *Application of a continuously tunable, cw optical parametric oscillator for high-resolution spectroscopy,* Optics Letters **23**, 40 (1998).

[8] E. V. Kovalchuk, D. Dekorsy, A. I. Lvovsky, C. Braxmaier, J. Mlynek, A. Peters, and S. Schiller, *High-resolution Doppler-free molecular spectroscopy with a continuous-wave optical parametric oscillator,* Optics Letters **26**, 1430 (2001).

[9] M. W. Todd, R. A. Provencal, T. G. Owano, B. A. Paldus, A. Kachanov, K. L. Vodopyanov, M. Hunter, S. L. Coy, J. I. Steinfeld, and J. T. Arnold, *Application of mid-infrared cavity-ringdown spectroscopy to trace explosives vapor detection using a broadly tunable (6-8 μm) optical parametric oscillator,* Applied Physics B **75**, 367 (2002).

[10] G. W. Baxter, H. D. Barth, and B. J. Orr, *Laser spectroscopy with a pulsed, narrow-band infrared optical parametric oscillator system: a practical, modular approach,* Applied Physics B **66**, 653 (2014).

[11] R. F. Curl and F. K. Tittel, *7 Tunable infrared laser spectroscopy,* Annual Reports Section "C" (Physical Chemistry) **98**, 219 (2002).

[12] D. D. Arslanov, M. P. P. Castro, N. A. Creemers, A. H. Neerincx, M. Spunei, J. Mandon, S. M. Cristescu, P. Merkus, and F. J. M. Harren, *Optical parametric oscillator-based photoacoustic detection of hydrogen cyanide for biomedical applications,* Journal of Biomedical Optics **18**, 107002 (2013).

[13] P. K. Rastogi and E. Hack, *Optical Methods for Solid Mechanics: A Full-Field Approach* (John Wiley & Sons, 2012).

7

CONCLUSIONS AND REMARKS

Natural gas is a major source of energy for many countries, especially for the Netherlands, due to the local resources in Groningen and the North Sea. However, the local production is expected to decrease by almost 80% in the coming 20 years due to the depletion of the resources. This is mainly compensated by importing natural gas from other countries. Moreover, there is an increasing trend toward the use of sustainable resources such as biogas. With all these changes, the composition of the natural gas in the Dutch gas grid diverges from the stable Groningen-gas to the more flexible 'new' gas. For safe and clean combustion and proper billing, the composition of natural gas must be monitored at both distribution points and households. This societal drive calls for a robust and low-cost gas sensor that does not require sample preparation or a lab technician to analyze the results.

Optical absorption spectroscopy in the mid-IR is a highly suitable method for composition measurement of combustible gases. It is a promising compromise for gas sensing between high-resolution and high-cost methods such as gas chromatography and non-selective and low-cost methods like calorimetric sensing. In optical absorption spectroscopy, light is passed through a sample and the ratio of absorbed to incident radiation is recorded. The sample is identified by comparing the acquired spectrum with a database. Because of these advantages and its non-destructive and self-referencing properties, mid-IR absorption spectroscopy is the method of choice in this thesis work.

Among several ways of implementing an optical absorption spectrometer, the linear variable optical filter (LVOF)-based option offers high sensitivity while maintaining low cost. An LVOF-based microspectrometer is composed of a wideband light source, an LVOF, a sample cell and a detector array. The manufacturing costs of such a microspectrometer can be kept to a minimum, as the batch fabrication of these elements is as-

sured. Therefore, the miniaturization of these components at the wafer-level is crucial. Several MEMS implementations of the light source, the filter and the detector array have been reported in the literature. However, the sample cell takes up most of the space in an LVOF-based microspectrometer and needs to be miniaturized at the wafer-level.

This ultimate miniaturization ambition is pursued in this thesis work by realizing a hollow LVOF resonator that serves also as a sample chamber. Therefore, the gas-filled LVOF functionally integrates the LVOF and the gas cell. The basic idea is that if the filter is operated at a high order, i.e. initially long cavity, and the mirrors are highly reflective, the physical cavity length at the μm-level can be elongated to the effective optical path length at the mm-level.

An important conclusion of this work is that, contrary to the general approach taken in the literature, LVOFs cannot be treated as Fabry-Perot (FP) filters, where the mirrors are perfectly parallel. At the demanding operating conditions of high mirror reflectivity and high order of operation, the angle between the mirrors of an LVOF that allows it to act as a wavelength-selective device in a wide wavelength range, cannot be neglected. Therefore, the design approach using the Fizeau interferometer model, where the angle between the flat and the tilted mirror is taken into account, was introduced in this thesis. The nonparallelism of the mirrors results in more design and optimization parameters such as the incidence angle, the filter-detector separation and the cone angle of the light source. It was shown both theoretically and experimentally that the optimum spectral response is obtained at a different negative incidence, directed at the imaginary apex of the cavity wedge, for every filter-detector separation. Moreover, the light source must be highly collimated to achieve interference.

The fabrication of the gas-filled LVOF relies on the integration of a flat and a tapered mirror by wafer bonding. The Bragg type mirrors are composed of alternate layers of sputtered Si and SiO_2 layers. The tapered mirror is fabricated using the CMOS-compatible method of patterning blocks of photoresist with linearly variable width, followed by transforming these blocks into a tapered photoresist layer by thermal-chemical reflow and subsequent transfer etching onto the underlying SiO_2 layer. The rest of the layers are sputtered on top and a tapered Bragg reflector is achieved.

The demanding operating conditions necessitate a custom-built opto-mechanical characterization setup combined with a HeNe laser at 3392 nm to confirm the theoretical approach of the Fizeau model. With slight differences due to fabrication tolerances, the design approach was validated. To see the optical path elongation effect of the device, the same setup is used, while methane is injected in the cavity of the filter. The measurement result shows that a 62.2-fold elongation in the optical absorption path is achieved using highly reflective mirrors. The measured elongation is lower than the theoretically predicted values mainly due to the high resolution of the laser compared to

the LVOF, which determines the resolution of the optical system with a wideband light source as was assumed in the calculations.

Wideband characterization of the filter with hydrocarbons was performed using an experimental optical parametric oscillator (OPO) laser in the mid-IR as the light source of the custom-built optomechanical setup. The spectral response of the LVOF with methane was compared to the IR-inactive gas, nitrogen, at 3221.69 nm, 3270.75 nm, 3317.89 nm and 3416.60 nm wavelengths using several dilution ratios. Based on the absorption coefficient of methane at these wavelengths, different changes in the filter transmission were observed. An effective optical path length of 1.534 mm is achieved at 3416.60 nm wavelength, which translates into a 64-fold path length elongation. Similar to the measurements with the HeNe laser, the elongation is lower than the theoretical values due to the high resolution of the OPO laser. Moreover, the response of the device to ethane at 3222 nm and 3448 nm wavelengths was demonstrated. Due to the lack of spectral data for ethane, the comparison was done qualitatively. As expected, the transmittance remained almost the same at 3222 nm wavelength, where ethane is nonabsorptive, while the transmittance decreased slightly at 3448 nm wavelength, where the absorption coefficient of ethane is nonzero. The spectral response of the filter with propane remained exactly the same at 3222 nm wavelength, where propane has no absorption, whereas the change in transmission was clearly demonstrated for several dilution ratios at 3449 nm wavelength, where propane is absorbing. Therefore, the feasibility of a gas-filled LVOF has been demonstrated for the composition analysis of natural gas with actual gas measurements.

The gas-filled LVOF is highly suitable for wafer-level microspectroscopy with low-cost and high-volume fabrication. Compared to its high-resolution benchtop counterparts with wide wavelength range and laser-based systems with ppb-level high sensitivity, gas-filled LVOF offers moderate wavelength range and sensitivity. However, both of these parameters can be tailored by adjusting the mirror materials and the optical design. Thanks to its design flexibility, gas-filled LVOF can be used to detect various materials at different wavelengths. Despite the demonstration of the feasibility of the gas-filled LVOF, several aspects of the device needs to be improved. First of all, the fabrication of the tapered mirror relies on tapering the first SiO_2 layer of the Bragg mirror. This results in a position dependent mirror reflectivity; hence, spectral response of the filter. To overcome this limitation, the taper must be transferred onto the Si wafer, which serves merely as a substrate. In this way, the optical design can be simplified. Furthermore, despite its simplicity, the thermal-chemical reflow method is still in the experimental phase. This technique should be standardized for high-volume batch fabrication. Secondly, instead of assuming discrete wavelengths, the effect of a wideband light source must be simulated using the design approach developed in this thesis. Based on this simulation, the

device parameters can be optimized more realistically and the sensor properties such as selectivity and sensitivity can be calculated. In this way, in addition to the device parameters, the optimum pixel size of the detector array can be calculated for the required selectivity and sensitivity. The demanding operating conditions of the gas-filled LVOF require an extremely well collimated light source. Therefore, a miniaturized light source with collimating optics must be realized with less than 2° half cone angle. Finally, the gas-filled LVOF must be integrated with a highly collimated light source and a detector array to be tested in the field.

SUMMARY

This thesis presents a robust and low-cost sensor for measuring the composition of natural gas. The functional integration of a linear variable optical filter (LVOF) and a gas cell using microelectromechanical systems (MEMS) technology allows for composition measurement in a wide wavelength range with a compact microspectrometer.

Chapter 1 describes the motivation of the project and investigates several gas sensing methods. The focus of the research is on methane, ethane and the combination of propane and butane. The ambition is to enable the selective measurement of these two molecules plus the combination. Moreover, optical absorption spectroscopy is chosen as the measurement method. The aim is to realize a robust and low-cost microspectrometer that operates in the mid-IR.

In Chapter 2, the options for implementing a miniaturized spectrometer for optical absorption spectroscopy are investigated. The most suitable method is optical filter based, especially the LVOF, which was indeed selected. The largest component in an LVOF-based microspectrometer is the sample cell and this thesis focuses on the functional integration of the gas cell and the LVOF. Firstly, the possibility of an on-chip optical absorption path as defined by 45° inclined mirrors is examined. Such structures are fabricated on the {110} planes using wet etching, by aligning the etch mask in the <100> crystal direction in a (100) wafer. However, optical simulations show that the efficiency of a system with 45° inclined mirrors is less than 1.1%. Instead, an on-chip optical absorption path with off-axis parabolic mirrors, where the collimation and the steering of the light are performed simultaneously, is analyzed. However, the strong effect of the fabrication tolerances on optical efficiency forced us to skip this intermediate step and to the take the miniaturization one step further. As a result, the full emphasis of this thesis is on using the resonator cavity of an LVOF also as a gas cell.

Due to the demanding conditions required for the operation of the gas-filled LVOF, the design approach is revisited in chapter 3. It was shown that an LVOF cannot be treated as a Fabry-Perot (FP) filter if it is operating at a high order and has highly reflective mirrors. Instead, the Fizeau interferometer model is adopted, where the angle between the two mirrors is taken into account. Both approaches are explained theoretically and compared in terms of the operating order, mirror reflectivity, incidence angle, filter-detector separation and the cone angle of the light source.

Chapter 4 explains the optical design of the gas-filled LVOF. Following the road map defined for the filter design, firstly the available IR spectral databases on hydrocarbons are compared. Based on the spectra of hydrocarbons and the requirements of the application, the operating order of the resonator and the reflectivity of the mirrors are selected. Since the tapered mirror is fabricated by tapering one of the mirror layers, extra attention was paid to the reflectivity calculations of such a structure. The chapter is finalized with the wideband optical simulations using the Fizeau approach developed in the previous chapter.

The fabrication details of the gas-filled LVOF are discussed in chapter 5. The devices are fabricated by integrating a flat and a tapered mirror by wafer bonding. Firstly, the fabrication flow of the flat and the tapered Bragg mirrors are described in detail. Then, the mask design for the 4-mask process is explained. The chapter ends with the description of the wafer bonding and the analysis of the mirror profile measurements.

In chapter 6, the characterization of the gas-filled LVOF is discussed in detail. Firstly, the results of the characterization of the filter itself are shown and explained. Due to the limitations of the measurement instrument in terms of the light source, the wideband characterization using a Fourier transform infrared (FTIR) spectrometer remained only qualitative. The simulations with the Fizeau model were confirmed using a custom-built setup with a HeNe laser. After a short discussion about the requirements imposed on device packaging for gas measurements, the spectral response of the filter with methane at 3392 nm is presented. The wideband measurements with methane, ethane and propane were performed using an optical parametric oscillator (OPO) laser as the light source. More than 60-fold elongation in optical path length is experimentally achieved and the response of the device to different gas mixtures is demonstrated.

Chapter 7 concludes the thesis and gives suggestions for the future work.

SAMENVATTING

Dit proefschrift presenteert een robuuste en goedkope sensor voor de meting van de samenstelling van aardgas. De functionele integratie van een lineaire variabele optische filter (LVOF) en een gascel, door toepassing van microelektromechanische systeem (MEMS) technologie, maakt compositiemeting mogelijk over een breed golflengtegebied met een compacte microspectrometer.

Hoofdstuk 1 beschrijft de motivatie van het project en onderzoekt de verschillende methoden voor de detectie (sensing) van gas. De focus van het onderzoek is op methaan, ethaan en de combinatie van propaan en butaan. Het is de ambitie om deze twee moleculen plus die combinatie selectief te kunnen meten. Bovendien is optische absorptiespectroscopie gekozen als meetmethode. Het is de bedoeling om een robuuste en goedkope microspectrometer te realiseren, met het mid-IR als het werkgebied.

In hoofdstuk 2 worden de mogelijkheden voor de uitvoering van een geminiaturiseerde spectrometer voor optische absorptiespectroscopie onderzocht. De meest geschikte methode is gebaseerd op optische filters, in het bijzonder met een LVOF, welke dan ook is gekozen. De grootste component in een LVOF-gebaseerde microspectrometer is de gas cel waarin het monster van het gas gedurende de meting is opgeslagen, en dit proefschrift richt zich op de functionele integratie van deze gas cel en de LVOF. In eerste instantie wordt de mogelijkheid van een chip met daarop een optisch absorptietraject als gedefinieerd door spiegels onder een helling van 45° onderzocht. Dergelijke structuren worden vervaardigd op de {110} vlakken met behulp van nat etsen, door het uitrichten van de etsmasker in de <100> kristalrichting in een (100) wafer. Echter, uit optische simulaties blijkt dat de efficiëntie van een systeem met 45° schuine spiegels minder dan 1,1%. In plaats daarvan is een on-chip optische absorptie pad met parabolische spiegels geanalyseerd, welke zijn verschoven ten opzichte van het optische pad en daarmee zorg draagt voor zowel collimatie als ook sturing van het lichtbundel. Echter, de sterke invloed van de fabricagetoleranties op de optische efficientie dwong ons deze tussenstap over te slaan en de volgende stap in de miniaturisatie te nemen. Hierdoor kwam de volledige nadruk van dit onderzoek te liggen op het gebruik van de resonatieruimte van een LVOF ook als gascel.

Vanwege de hoge eisen waaraan de gasgevulde LVOF moet voldoen, wordt de ontwerpmethodiek in hoofdstuk 3 herzien. Daarbij werd aangetoond dat een LVOF niet kan worden beschouwd als een Fabry-Perot (FP) filter indien deze werkt bij een hoge orde

en is voorzien van sterk reflecterende spiegels. In plaats daarvan wordt het Fizeau interferometermodel overgenomen, waarbij de hoek tussen de twee spiegels wordt meegenomen in de benadering. Beide benaderingen zijn theoretisch toegelicht en vergeleken wat betreft het effect van de ingestelde orde van de resonantie, reflectie van de spiegels, invalshoek, afstand tussen filter en detector en de openingshoek van de lichtbron.

Hoofdstuk 4 verklaart het optisch ontwerp van de gasgevulde LVOF. Het stappenplan zoals gedefinieerd voor het filter ontwerp wordt gevolgd, waarbij eerst de beschikbare IR spectrale databases voor koolwaterstoffen worden vergeleken. Gebaseerd op de spectra van koolwaterstoffen en de vereisten van de toepassing, worden de orde van de resonantie en de reflectie van de spiegels gekozen. Aangezien de tapse spiegel wordt vervaardigd door een tapsgewijze vormgeving van een van de lagen in de spiegel, werd extra aandacht besteed aan de berekening van de reflectie van een dergelijke structuur. Het hoofdstuk wordt afgesloten met de optische simulaties over een brede spectrale band op basis van de Fizeau aanpak, zoals ontwikkeld in het voorgaande hoofdstuk.

De details van de fabricage van de gasgevulde LVOF worden besproken in hoofdstuk 5. Deze zijn vervaardigd door het integreren van een plat en een taps toelopende spiegel met behulp van wafer bonding. In eerste instantie wordt het stroomdiagram van de fabricage van de vlakke en de tapse Bragg spiegels in detail beschreven. Vervolgens wordt het maskerontwerp voor het 4-masker proces toegelicht. Het hoofdstuk eindigt met de beschrijving van de hechting van de wafers (wafer bonding) en de analyse van de profielmetingen aan de spiegel.

In hoofdstuk 6 wordt de karakterisering van de gasgevulde LVOF in detail besproken. Allereerst worden de resultaten van de karakterisering van het filter zelf getoond en toegelicht. Door de beperkingen van het meetinstrument wat betreft de lichtbron, kan de breedbandige karakterisering met een Fourier spectrometer (Fourier transform infrared -FTIR- spectrometer) slechts kwalitatief zijn. De simulatieresultaten op basis van het Fizeau model werden bevestigd door gebruik te maken van een op maat gemaakte opstelling met een HeNe laser. Na een korte discussie over de eisen te stellen aan de behuizing van sensoren voor gasmetingen, wordt de spectrale respons van het filter voor methaan bij 3392 nm gepresenteerd. De breedbandige metingen aan methaan, ethaan en propaan werden uitgevoerd met een optische parametrische oscillator (OPO) laser als lichtbron. Een meer dan 60-voudige verlenging in optische weglengte wordt experimenteel verkregen en de respons voor verschillende gasmengsels wordt getoond.

Hoofdstuk 7 sluit het proefschrift af en geeft voorstellen voor toekomstige werkzaamheden.

ACKNOWLEDGEMENTS

It always seems impossible until it's done.

Nelson Mandela

At each step in my career, I thought I was facing the biggest challenge of my life. Over the years, I realized that the challenge not only became bigger but also reduced to an individual level. The PhD, being the hardest and the most personal task I have faced so far, could not be completed without the help of my family, friends and colleagues.

I am grateful to my supervisor Dr. ir. Reinoud F. Wolffenbuttel and my promoter Prof. dr. ir. Albert J.P. Theuwissen for giving me the chance to work in this multi-disciplinary project funded by STW that combined a real life application with daring scientific questions, a rare and valuable combination in academia. While many colleagues suffered from being micromanaged or completely neglected, Dr. Wolffenbuttel provided me with just the right amount of supervision that allowed me to become an independent researcher.

Advances in research are strongly influenced, even steered, by the prior discoveries in the field. The accumulated knowledge on optical microsystems in our research group enabled the realization of this particular hydrocarbon sensor. Among many findings, Dr. Arvin Emadi's work on the fabrication of optical filters funded by Energy Delta Gas Research (EDGaR) Consortium laid the groundwork for the device described in this dissertation. Needless to say, the implementation of previous findings into the current device would not be possible without the help of the group members. I am thankful to my colleague Amir Ghaderi for his help with the fabrication and Dr. Ger de Graaf for valuable discussions.

This multi-disciplinary research project required a fundamental understanding of optical sensing and spectroscopy. As a researcher with a microelectronics background, I had the opportunity to learn from the pioneers of the field, to one of whom I am deeply indebted for his help. Prof. Emer. H. Angus Macleod provided insight about the limitations of the sensor during our fruitful discussions and inspired me to change my design perspective completely. Besides his scientific knowledge, I admire that he encouraged

me to ask more questions in the e-mail conversation that started with a simple inquiry about his thin-film coating design software. It is uplifting to know that such dedicated and enthusiastic scientists still exist in today's scientific community.

The gas sensors described in this dissertation were fabricated in two clean room facilities, Nanofabrication Laboratory, Chalmers University of Technology in Gotheburg, Sweden and Else Kooi Laboratory (formerly DIMES), Delft University of Technology in Delft, the Netherlands. I am grateful to Prof. dr. Peter Enokkson for temporarily welcoming me in his group, Henrik Frederiksen for his help with sputtering and Ulf Södervall for his help in organizational matters. I am much obliged to the staff of Else Kooi Laboratory for their assistance while I was simultaneously fabricating devices and working toward my diploma. Fabrication would not be successful without the help of Dr. Gregory Pandraud, Silvana Milosavljevic, Johan van der Cingel, Tom Scholtes and Dr. Henk van Zeijl. Also, I would like to thank Dr. An Tran for helping me with wafer bonding.

The characterization of the sensors required a light source with specific properties, which strongly limited our options. Dr. Frans Harren, head of the Life Science Trace Gas Research Group in Radboud University, kindly opened his laboratory to us for measurements. Thanks to him, I was able to demonstrate the wideband operation of the devices in addition to proving that even a huge optical setup could be portable if carried in a big suitcase. I am also grateful to Dr. Julien Mandon for sharing his expertise and helping me with the measurements.

The last four years were not only about research. I had the chance to be a board member of MEST and organize several events with my colleagues. Thanks to the encouragement of Dr. ir. André Bossche, I was involved in the Master Kick-off event twice, where we helped new MSc students to integrate. It was a wonderful experience to attend the High Talent Summer School in Chengdu, China with my colleagues Wouter Brevet, Aleksandar Jović, Junfeng Jiang, Lorenzo Pedalà, Violeta Prodanović, Yelena Grachova, Robert Sokolovskij and Gustavo Campos Martins. I was lucky to work with Prof. dr. Kofi Makinwa in the organization of monthly colloquiums, where I learned how to help my colleagues prepare their presentations and how to trick people into attending an event using pizza as a bait.

According to the World Health Organization, most of the world's population spend one-third of their adult life at work. If it was not for my past and present office mates Dr. Zhichao Tan, Saleh Heidary Shalmany, Long Xu and Hui Jiang, my job would not be bearable. I am particularly thankful to Hui for always having back-up for my afternoon sugar craving. Thanks to Hui and his wife Unee, I had the chance to taste amazing, and usually very spicy, Chinese food at several occasions.

The Electronic Instrumentation Laboratory has been my second home in the last four years. This thesis would not be completed without the help of *EI people*. Our tech-

nicians Lukasz Pakula, Zu-yao Chang, Ron van Puffelen and Jeroen Bastemeijer were always there with practical solutions when needed. The secretaries Joyce Siemers and Karen van Busschbach served more like lifelines when we had to tackle the bureaucracy of TU Delft. It was always great to see friendly faces of my colleagues Zeyu Cai, Chao Chen, Xiaoliang Ge, Burak Gönen, Accel Abarca Prouza, Uğur Sönmez, Xin Yu, Stephen van 't Hof, Dr. Fabio Sebastiano, Dr. Ruimin Yang and Dr. Guijie Wang in the corridors of EI Laboratory and Dr. Aslıhan Arslan, Dr. ir. Sten Vollebregt, Dr. Jing Zhang, Pan Liu, Cinzia Silvestri, Miki Trifunovic, Dr. Amir Sammak and Dr. Sima Tarashioon at ECTM. My special thanks go to Aslıhan for helping me find this PhD position and adjust to Delft during my first year.

I fell in love with Delft, the moment I set foot in it. But what made it more beautiful was the kind people of Delft. Among many of them that I got to know, I am mostly grateful to René and Marijke Colsen for making this small town feel more like home.

They say it becomes harder to make good friends as you become older. Funnily enough, I made my best friends after mid-twenties. Dr. Sibel Eker, my true friend, has been there for me from the beginning to the end at good times and bad times. Together we traveled to places that I would never go, cooked dishes that I would never cook, saw movies that I would never see, did sports that I would never do... *Ok, ice-skating does not count, but at least we tried.* I am also grateful that she agreed to be my paranymph in the defense ceremony. Rumor has it that paranymphs are officially entitled to carry a sword, so will she? I had the chance to get to know Arjang Alidai only in the last two years but all the laughter that Sibel and he brought into my life made up for lost time. Laura Kingston came into my life quite unexpectedly as a room mate when I was an undergraduate. Despite moving to initially different universities and then different countries, we always stayed in touch. Although she is not able to stand by my side this time, I am deeply grateful for her moral support during both my MSc and PhD years. Cem Sağıroğlu was always a phone call away when I needed a friend to talk to. It is very comforting to know that we can still share a laughter despite the miles between us.

The involvement of parents in their child's education is indispensable. However, my parents took it a bit too seriously. My mother, a primary school teacher herself, was practically my in-house teacher, who turned out to be more demanding than her daytime counterpart. To this day, I can confidently say that I studied primary school twice. Despite his vast knowledge about geography, my father did not particularly enjoy helping me with my courses. Instead, he took care of all the practical matters. Thanks to this admirable team effort I made it through high school. Then, my brother, whom I followed career-wise for quite a while, came into play. Thanks to his endless support and experience, I managed to become an engineer. Even though my family's input gradually decreased over the years, they never stopped supporting me and occasionally remind-

ing me to work harder. Apparently the involvement of family in a child's education is also everlasting! In all seriousness, I am deeply grateful to my family for standing by my side at every step I take in life.

As the Swedish proverb goes: *shared joy is a double joy, shared sorrow is half a sorrow.* I was lucky to share all the ups and downs of the last four years with René. Here's to many more years full of adventures...

List of Publications

Journal Articles

1. **N. P. Ayerden**, M. Ghaderi, P. Enoksson, G. de Graaf, and R. F. Wolffenbuttel, "A miniaturized optical gas-composition sensor with integrated sample chamber", Sensors and Actuators B: Chemical (2016).

2. **N. P. Ayerden**, G. de Graaf, and R. F. Wolffenbuttel, "Compact gas cell integrated with a linear variable optical filter", Optics Express **24**, 2981-3002 (2016).

3. **N. P. Ayerden**, U. Aygun, S. T. S. Holmstrom, S. Olcer, B. Can, J.-L. Stehle, and H. Urey, "High-speed broadband FTIR system using MEMS", Applied Optics **53**, 7267-7272 (2014).

4. H. R. Seren, S. Holmstrom, **N. P. Ayerden**, J. Sharma, and H. Urey, "Lamellar-grating-based MEMS Fourier transform spectrometer", Journal of Microelectromechanical Systems **21**, 331-339 (2012).

5. M. Ghaderi, **N. P. Ayerden**, A. Emadi, P. Enoksson, J. H. Correia, G. de Graaf, and R. F. Wolffenbuttel, "Design, fabrication and characterization of infrared LVOFs for measuring gas composition", Journal of Micromechanics and Microengineering **24**, 084001 (2014).

6. M. Ghaderi, **N. P. Ayerden**, G. de Graaf, and R. F. Wolffenbuttel, "Minimizing stress in large-area surface micromachined perforated membranes with slits", Journal of Micromechanics and Microengineering **25**, 074010 (2015).

Conference Proceedings

1. **N. P. Ayerden**, G. de Graaf, P. Enoksson, and R. F. Wolffenbuttel, "A highly miniaturized NDIR methane sensor", in *SPIE Photonics Europe*, Brussels, Belgium, 2016, pp. 98880D-98880D-8. **Best student paper award*

2. **N. P. Ayerden**, M. Ghaderi, G. de Graaf, and R. F. Wolffenbuttel, "A miniaturized optical sensor with integrated gas cell", in *Procedia Engineering (Eurosensors)*, **120**, 392-395, 2015.

3. **N. P. Ayerden**, M. Ghaderi, G. de Graaf, and R. F. Wolffenbuttel, "Optical design and characterization of a gas filled MEMS Fabry-Perot filter", in *SPIE Microtechnologies*, Barcelona, Spain, 2015, pp. 95171N-95171N-8.

4. **N. P. Ayerden**, M. Ghaderi, G. de Graaf, and R. F. Wolffenbuttel, "A miniaturized optical sensor for natural gas analysis", in *The Sense of Contact*, Soesterberg, the Netherlands, 2015. **Best poster award*

5. **N. P. Ayerden**, M. Ghaderi, G. de Graaf, and R. F. Wolffenbuttel, "A lossy Fabry-Perot based optical filter for natural gas analysis", in *Procedia Engineering (Eurosensors)*, **87**, 1410-1413, 2014.

6. **N. P. Ayerden**, M. Ghaderi, M. F. Silva, A. Emadi, P. Enoksson, J. H. Correia, G. de Graaf, and R. F. Wolffenbuttel, "Design, fabrication and characterization of LVOF-based IR microspectrometers", in *SPIE Photonics Europe*, Brussels, Belgium, 2014, pp. 91300T-91300T-10.

7. **N. P. Ayerden**, M. Ghaderi, G. de Graaf, and R. F. Wolffenbuttel, "A linear variable optical filter (LVOF) for gas analysis", in *The Sense of Contact*, Soesterberg, the Netherlands, 2014.

8. **N. P. Ayerden**, M. Ghaderi, G. de Graaf, and R. F. Wolffenbuttel, "Design and fabrication of a lossy Fabry-Perot detector for infrared absorption spectroscopy on combustible gases", in *Micromechanics and Microsystems Europe*, Espoo, Finland, 2013.

9. **N. P. Ayerden**, J. L. Stehle, S. Holmstrom, and H. Urey, "MEMS FTIR spectrometer and optical results", in *2012 International Conference on Optical MEMS and Nanophotonics*, Banff, AB, Canada, 2012, pp. 130-131.

10. **N. P. Ayerden**, S. Holmstrom, H. R. Seren, S. Olcer, J. Sharma, S. Luettjohann, T. Sandner, and H. Urey, "MEMS Fourier transform IR spectrometer", in *2011 International Conference on Optical MEMS and Nanophotonics*, Istanbul, Turkey, 2011, pp. 11-12.

11. H. R. Seren, **N. P. Ayerden**, S. Holmstrom, and H. Urey, "MEMS Fourier transform spectrometer", in *General Assembly and Scientific Symposium, 2011 XXXth URSI*, Istanbul, Turkey, 2011, pp. 1-4.

12. H. R. Seren, **N. P. Ayerden**, J. Sharma, T. S. S. Holmstrom, T. Sandner, T. Grasshoff, H. Schenk, and H. Urey, "Lamellar grating based MEMS Fourier transform spectrometer", in *2010 International Conference on Optical MEMS and Nanophotonics*, Sapporo, Japan, 2010, pp. 105-106.

13. M. Ghaderi, **N. P. Ayerden**, G. de Graaf, and R. F. Wolffenbuttel, "Vapour HF release of airgap-based UV-visible optical filters", in *Procedia Engineering (Eurosensors)*, **120**, 816-819, 2015.

14. M. Ghaderi, **N. P. Ayerden**, G. de Graaf, and R. F. Wolffenbuttel, "Optical characterization of MEMS-based multiple air-dielectric blue-spectrum distributed Bragg reflectors", in *SPIE Microtechnologies*, Barcelona, Spain, 2015, pp. 95171M-95171M-6.

15. M. Ghaderi, **N. P. Ayerden**, G. de Graaf, and R. F. Wolffenbuttel, "Surface-micromachined Bragg reflectors based on multiple airgap/SiO_2 layers for CMOS-compatible Fabry-Perot filters in the UV-visible spectral range", in *Procedia Engineering (Eurosensors)*, **87**, 1533-1536, 2014.

16. M. Ghaderi, **N. P. Ayerden**, A. Emadi, P. Enoksson, J.H. Correia, G. de Graaf, and R. F. Wolffenbuttel, "LVOF-based IR microspectrometer for gas composition measurement", in *Micromechanics and Microsystems Europe*, Espoo, Finland, 2013.

17. E. Karimi Shahmarvandi, M. Ghaderi, **N. P. Ayerden**, G. de Graaf, and R. F. Wolffenbuttel, "CMOS-compatible metamaterial-based wideband mid-infrared absorber for microspectrometer applications", in *SPIE Photonics Europe*, Brussels, Belgium, 2016, pp. 988309-988309-9.

About the Author

N. Pelin Ayerden was born in Karabük, Turkey in 1986. She attended both primary and high school in the historical town of Safranbolu. She attained her BSc degree from Boğaziçi University, Istanbul, Turkey in 2009, specializing in microelectronics. She graduated from Koç University, Istanbul, Turkey in 2012 with her master's thesis "Lamellar Grating Interferometer Based MEMS Fourier Transform Infrared Spectrometer". Her master's work was supervised by Prof. Hakan Ürey in the FP7 project *MEMFIS: Ultrasmall MEMS FTIR Spectrometer*. During her MSc, she successfully developed a MEMS interferometer based benchtop FTIR spectrometer. She was awarded with the MSc scholarship by Koç University, where she worked as both research and teaching assistant. She was a visiting researcher at Fraunhofer Institute for Photonic Microsystems (IPMS), Dresden, Germany in the summer of 2010, where she characterized MEMS mirrors that were designed and fabricated for the MEMFIS project.

She has been working toward her PhD degree in the Electronic Instrumentation Laboratory of Delft University of Technology since 2012. She conducted research on the development of a microspectrometer for natural gas analysis within the framework of the STW funded project *Microsystem for Multi-gas Analysis*, under the supervision of Dr. ir. Reinoud F. Wolffenbuttel. During her doctoral studies, she focused on the miniaturization of spectrometers at the wafer-level. Her work was mainly on the functional integration of the linear variable optical filter (LVOF) and the gas cell for the composition measurement of natural gas. She designed, fabricated and characterized the *gas-filled LVOF*, paving the way toward the ultimate miniaturization of microspectrometers. She presented her work in reputable scientific journals and conferences, which brought her the best poster award at The Sense of Contact in 2015 and the best student paper award at SPIE Photonics Europe in 2016.

She organizes the monthly colloquiums of Electronic Instrumentation Laboratory and served as a board member in Micro-Electronic Systems & Technology Association (MEST). She also worked as the secretary in the IEEE Instrumentation and Measurement Chapter of the BeNeLux Section, (Chapter IM09).